NASA/TM—1998-208503

Experimental Study of Boundary Layer Behavior in a Simulated Low Pressure Turbine

Rickey J. Shyne
Lewis Research Center, Cleveland, Ohio

National Aeronautics and
Space Administration

Lewis Research Center

October 1998

Acknowledgments

The author wishes to gratefully acknowledge the support of the many individuals who were helpful in this endeavor. Special thanks is extended to Dr. Eric McFarland and Mr. Nicholas Georgidias for their help in the computational analyses used in this dissertation. Special gratitude and thanks is extended to Dr. Ki-Hyeon Sohn for his assistance in the experimental research portion of this dissertation. The author also wishes to thank Dr. Robert Simoneau, Mr. Frederick Simon and Dr. John Adamcyzk for their advice and consultation in formulating this research. A very special note of appreciation is extended to my advisers, Drs. Kenneth J. DeWitt and Theo G. Keith, Jr., for their encouragement, guidance, and patience during the completion of this work.

An Abstract of

EXPERIMENTAL STUDY OF BOUNDARY LAYER BEHAVIOR IN A SIMULATED LOW PRESSURE TURBINE

Rickey J. Shyne

Submitted in partial fulfillment
of the requirements of the
Doctor of Philosophy Degree

The University of Toledo

An experimental investigation of boundary layer behavior on the suction surface of a simulated low pressure turbine (LPT) blade was conducted. The Boundary Layer Transition Tunnel at the NASA Lewis Research Center was used in the study. A large scale experiment was developed for this facility to simulate the pressure gradients typically found in low pressure turbines. A two-dimensional flow was established, and passed through the test section. The upper wall of the test section was designed so that the LPT pressure gradients would be imposed on a flat plate opposite it. The large size and simple geometry of the experiment facilitated the detailed measurement of the boundary layer flow. A basic understanding of the detailed flow physics is required to consistently design high performance low pressure turbines, which have to operate over a wide range of conditions. An inviscid, integral equation solver was used to design the test section, and a Navier-Stokes computational fluid dynamics code was used to analyze the design.

Detailed data including flow visualization data were acquired to help understand the boundary layer transition process in the LPT. Measurements were made in the test section module at Reynolds numbers experienced in a LPT at typical take-off and cruise conditions. Reynolds numbers of 100,000 and 250,000 based upon the test section length and exit velocity were used for this study. This was due the scaling of the test section to tunnel blower constraints. The flow behavior at these test conditions are representative of

those encountered at cruise and take-off flight conditions with separated and attached flow occurring at the lower and higher Reynolds numbers, respectively. The effects of freestream turbulence intensity (TI) and Reynolds number on the transition process were investigated during this study. Flow visualization was performed using a nichrome wire smoke generator system as well as tufts, and these methods were used to identify areas of separation. Hot-wire probes (single and x-wire) were utilized to obtain detailed boundary layer measurements at multiple axial locations and flush mounted hot-film gages were used to identify the onset and location of transition and turbulent spot development. Static pressure measurements were also made to quantify the surface pressure distribution.

Detailed measurements revealed that a separation bubble occurs on the lower wall at a typical take-off Reynolds number for all freestream turbulence levels tested. Separation was confirmed for 0.8% TI (grid 0) through the use of smoke flow visualization and for all turbulence levels through hot-wire measurements. The separation bubble starts just downstream of the throat (minimum flow area) and reattaches as a turbulent boundary layer downstream. Hot-wire signals were also analyzed to compute intermittency values all levels of TI and Reynolds numbers tested.

The transition process over the separated flow region was observed to behave like a laminar free shear layer flow through the formation of a large coherent eddy structure. It can be concluded from this study that the transition process is still bypass, but it follows a different process. The study also revealed that classical disturbances were not discerned in the flow field generated in the upstream portion of the test section from the boundary spectra data and it could not be concluded that the upstream disturbances affect the downstream boundary layer behavior. Additionally, it can be concluded that for the ranges of freestream turbulence intensity evaluated in this experiment and a Reynolds number of 100,000, a separation bubble will occur for a pressure gradient parameter, K, below -4.0×10^{-6}.

TABLE OF CONTENTS

Abstract i

Nomenclature v

List of Figures ix

List of Tables xvi

I. INTRODUCTION 1

II. BACKGROUND 6
A. Low Pressure Turbine Flow Physics 6
B. Boundary Layer Behavior 7
C. Computational Efforts 9

III. RESEARCH FACILITY 20
A. Boundary Layer Transition Tunnel 20
B. Test Section 21
C. Flow Visualization 23
D. Instrumentation 24
1. Steady-State Instrumentation 24
2. Dynamic Instrumentation 25

IV. DATA ACQUISITION 35
A. Steady-State Data 35
B. Unsteady Data 36
C. Calibration 36
1. Hot-wire Calibration 37
2. Hot-film Calibration 37

V. RESULTS AND DISCUSSION 39
A. Characterization of Flow 39
B. Flow Visualization Data 45
C. Establishment of Test Conditions 47
D. Pressure Distribution Data 48
E. Hot-wire Data 52
1. Mean Velocity Contour Plots 52
2. Law of the Wall Plots 58
3. Fluctuating (rms) Velocity Profiles 65
4. Boundary Layer Parameters 75

5. Intermittency Profiles 90
6. Power Spectra Density Data 95
7. Integral Length Scales 105
8. Classification of Separation Bubble 105
F. Hot-film Data 108
G. X-wire Data 114
1. X-wire u′ Velocity Profiles 114
2. X-wire v′ Velocity Profiles 119
3. Reynolds Shear Stress Profiles 125

VI. UNCERTAINTY ANALYSIS 131

VII. CONCLUSIONS AND RECOMMENDATIONS 136

VIII. REFERENCES 139

NOMENCLATURE

AR Aspect ratio $\left[=\frac{\text{span}}{\text{chord}}\right]$

A Constant in thermal response equations of hot-wire

B Constant in thermal response equations of hot-wire

c_f Skin friction coefficient $\left[=\frac{\tau}{q_\infty}\right]$

c_f Pressure coefficient $\left[=\frac{p_l - p_\infty}{q_\infty}\right]$

E_L Linearized voltage, volts

f Frequency, hertz

H_{12} Shape factor $\left[=\frac{\delta^*}{\theta}\right]$

H_{32} Shape factor $\left[=\frac{\varepsilon}{\theta}\right]$

i Wire current, amperes

K Pressure Gradient Parameter $\left[=\frac{\nu}{U_m^2}\frac{dU_m}{dx}\right]$

$\frac{l_w}{d_w}$ Length-to-diameter ratio of wire

l_w^+ Wire length normalized in wall units $\left[=\frac{u_\tau l_w}{\nu}\right]$

PSD Power spectral density $\left[\frac{V^2}{Hz}\right]$

p Local static pressure, $\frac{lb_f}{in^2}$ or kPa

p_∞ Free-stream static pressure, $\frac{lb_f}{in^2}$ or kPa

q_∞ Dynamic pressure, $\left[=\frac{1}{2}\rho_\infty v_\infty^2\right]$, $\frac{lb_f}{in^2}$ or kPa

Re_x Length Reynolds number $\left[=\frac{U_e x}{\nu}\right]$

Re_θ Momentum thickness Reynolds number $\left[=\frac{U_e \theta}{\nu}\right]$

Re_{δ^*} Displacement thickness Reynolds number $\left[=\frac{U_e \delta^*}{\nu}\right]$

r_0 Radius of wire, inches or mm

T Instantaneous or Mean temperature, °F or °C

TI Free-stream turbulence intensity $\left[=\frac{\sqrt{\frac{1}{3}\left(\overline{u'^2}+\overline{v'^2}+\overline{w'^2}\right)}}{U_\infty}\right]$

u' Fluctuating streamwise velocity, $\frac{ft}{sec}$ or $\frac{m}{sec}$

U Instantaneous or mean streamwise velocity, $\frac{ft}{sec}$ or $\frac{m}{sec}$

U_0 Magnitude of actual velocity, $\frac{ft}{sec}$ or $\frac{m}{sec}$

u_τ Friction velocity $\left[=\sqrt{\frac{\tau_w}{\rho}}\right]$, $\frac{ft}{sec}$ or $\frac{m}{sec}$

u^+ Streamwise mean velocity in wall units $\left[=\frac{U}{u_\tau}\right]$

v Spanwise vertical velocity, $\frac{ft}{sec}$ or $\frac{m}{sec}$

v' Instantaneous or rms vertical fluctuating velocity, $\frac{ft}{sec}$ or $\frac{m}{sec}$

V Bridge voltage of the hot-wire anemometer or instantaneous, volts

$-\overline{u'v'}$ Reynolds shear stress, $\frac{lb_f}{ft^2}$ or $\frac{N}{m^2}$

X or x Streamwise distance from leading edge of test section, inches or cm

y Vertical distance from the wall, inches or cm

Y_o Typical distance between wall and first measurement station, inches or cm

y^+ Vertical distance in wall units $\left[=\frac{u_\tau y}{\nu}\right]$

y_b Contour height, inches or cm

y_c Flow path height, inches or cm

y_o Tunnel inlet height, inches or cm

y_2 Exit height, inches or cm

Greek

α	Temperature coefficient of resistance
Γ	Intermittency factor
$\delta_{0.995}$	Boundary layer thickness at U = 0.995 U_e, inches or mm
δ^*	Integral displacement thickness $\left[= \int_0^\infty \left(1 - \frac{u}{U} \right) dy \right]$, inches or mm
ε	Integral energy thickness $\left[= \int_0^\infty \left(1 - \left(\frac{u}{U} \right)^2 \right) \left(\frac{u}{U} \right) dy \right]$, inches or mm
Λ	Longitudinal integral length scale, inches or mm
θ	Integral momentum thickness $\left[= \int_0^\infty \left(1 - \frac{u}{U} \right) \left(\frac{u}{U} \right) dy \right]$, inches or mm
ν	Kinematic viscosity, $\frac{ft^2}{sec}$ or $\frac{m^2}{sec}$
ρ	Density, $\frac{lb_m}{ft^3}$ or $\frac{kg}{m^3}$
τ	Wall shear stress, $\frac{lb_f}{in^2}$ or $\frac{N}{m^2}$

Subscripts

a	Ambient conditions
e	Boundary layer edge or free-stream
fs	free-stream
lam	laminar
max	maximum
w	Wall or wire
n	Non-turbulent part of the quantities
o	Total quantities
t	Turbulent part of the quantities
tur	Turbulent
∞	Free-stream conditions

LIST OF FIGURES

Figure 1 Typical turbine blade-row velocity diagram and surface static pressure distribution 5

Figure 2 Boundary layer development on a turbine 12

Figure 3 Viscous effects in flow around an airfoil 12

Figure 4 Transition events on a turbine airfoil (Laminar separation and reattachment) 13

Figure 5 Separated flow velocity profile, velocity gradient and velocity curvature and pressure distributions 14

Figure 6 Generic low pressure turbine (LPT) blade 15

Figure 7 Generic low pressure turbine blade (LPT) Panel code pressure distribution 16

Figure 8 Panel code simulated low pressure turbine test section geometry 17

Figure 9 Comparison of LPT blade and simulated LPT lower wall Panel code pressure distributions, Re = 250,000 18

Figure 10 NPARC velocity contour plot of simulated LPT test section 19

Figure 11 Schematic diagram of unmodified boundary layer transition tunnel 30

Figure 12 Schematic diagram of simulated low pressure turbine test section 31

Figure 13 Photograph of boundary layer transition tunnel with simulated low pressure turbine test section 32

Figure 14 Photograph of simulated low pressure turbine test section from inside and upstream of boundary layer transition tunnel 33

Figure 15 Schematic diagram of simulated low pressure turbine test section lower wall 34

Figure 16 Sample Streamline hot-wire probe calibration curve 38

Figure 17 K, pressure gradient parameter, grids 0, 2 and 3, Re = 100,000 43

Figure 18 K, pressure gradient parameter, grids 0, 2 and 3, Re = 250,000 43

Figure 19 Edge velocity variation, grids 0, 2 and 3, Re = 100,000.....44

Figure 20 Edge velocity variation, grids 0, 2 and 3, Re = 250,000.....44

Figure 21 Photograph of flow visualization without suction, grid 0, Re ≈ 50,000..46

Figure 22 Photographs of flow visualization with suction, grid 0, Re ≈ 50,000 47

Figure 23 Experimental simulated test section lower wall pressure distributions, grids 0, 2 and 3, Re = 100,000 51

Figure 24 Experimental simulated test section lower wall pressure distributions, grids 0, 2 and 3, Re = 250,000 51

Figure 25 Comparison of computational and experimental lower wall pressure distributions, Re = 250,000.....52

Figure 26 Mean velocity and streamline contour, grid 0, Re = 100,000.....55

Figure 27 Mean velocity and streamline contour, grid 2, Re = 100,000 55

Figure 28 Mean velocity and streamline contour, grid 3, Re =100,000.....56

Figure 29 Mean velocity and streamline contour, grid 0, Re =250,000 56

Figure 30 Mean velocity and streamline contour, grid 2, Re =250,000.....57

Figure 31 Mean velocity and streamline contour, grid 3, Re =250,000.....57

Figure 32 Upstream streamwise mean velocity profiles in wall units, grid 0, Re = 100,000.....60

Figure 33 Upstream streamwise mean velocity profiles in wall units, grid 2, Re = 100,000.....61

Figure 34 Upstream streamwise mean velocity profiles in wall units, grid 3, Re = 100,000.....61

Figure 35 Upstream streamwise mean velocity profiles in wall units, grid 0, Re = 250,000.....62

Figure 36 Upstream streamwise mean velocity profiles in wall units, grid 2, Re = 250,000.....62

Figure 37 Upstream streamwise mean velocity profiles in wall units, grid 3, Re = 250,000 63

Figure 38 Downstream streamwise mean velocity profiles in wall units, grid 0, Re = 250,000 63

Figure 39 Downstream streamwise mean velocity profiles in wall units, grid 2, Re = 250,000 64

Figure 40 Downstream streamwise mean velocity profiles in wall units, grid 3, Re = 250,000 64

Figure 41 Downstream rms velocity and streamline profiles, grid 0, Re = 100,000 66

Figure 42 Downstream rms velocity and streamline profiles, grid 2, Re = 100,000 67

Figure 43 Downstream rms velocity and streamline profiles, grid 3, Re = 100,000 67

Figure 44 Downstream rms velocity and streamline profiles, grid 0, Re = 250,000 68

Figure 45 Downstream rms velocity and streamline profiles, grid 2, Re = 250,000 68

Figure 46 Downstream rms velocity and streamline profiles, grid 3, Re = 250,000 69

Figure 47 Upstream rms velocity profiles, grid 0, Re = 100,000 69

Figure 48 Upstream rms velocity profiles, grid 2, Re = 100,000 70

Figure 49 Upstream rms velocity profiles, grid 3, Re = 100,000 70

Figure 50 Upstream rms velocity profiles, grid 0, Re = 250,000 71

Figure 51 Upstream rms velocity profiles, grid 2, Re = 250,000 71

Figure 52 Upstream rms velocity profiles, grid 3, Re = 250,000 72

Figure 53 Downstream rms velocity profiles, grid 0, Re = 100,000 72

Figure 54 Downstream rms velocity profiles, grid 2, Re = 100,000 73

Figure 55 Downstream rms velocity profiles, grid 3, Re = 100,000.....73

Figure 56 Downstream rms velocity profiles, grid 0, Re = 250,000.....74

Figure 57 Downstream rms velocity profiles, grid 2, Re = 250,000.....74

Figure 58 Downstream rms velocity profiles, grid 3, Re = 250,000.....75

Figure 59 Displacement thickness profiles, grids 0, 2 and 3, Re = 100,000.....78

Figure 60 Momentum thickness profiles, grids 0, 2 and 3, Re = 100,000.....79

Figure 61 Energy thickness profiles, grids 0, 2 and 3, Re = 100,000 79

Figure 62 Shape factor profiles, grids 0, 2 and 3, Re = 100,000.....80

Figure 63 Energy shape factor profiles, grids 0, 2 and 3, Re = 100,000.....80

Figure 64 Displacement thickness profiles, grids 0, 2 and 3, Re = 250,000.....81

Figure 65 Momentum thickness profiles, grids 0, 2 and 3, Re = 250,000.....81

Figure 66 Energy thickness profiles, grids 0, 2 and 3, Re = 250,000 82

Figure 67 Shape factor profiles, grids 0, 2 and 3, Re = 250,000.....82

Figure 68 Energy shape factor profiles, grids 0, 2 and 3, Re = 250,000.....83

Figure 69 Skin friction profiles, grids 0, 2 and 3, Re = 250,000 83

Figure 70 Indicator function determination technique for single wire.....92

Figure 71 Downstream intermittency profiles, grid 0, Re = 100,000 92

Figure 72 Downstream intermittency profiles, grid 2, Re = 100,000 93

Figure 73 Downstream intermittency profiles, grid 3, Re = 100,000 93

Figure 74 Downstream intermittency profiles, grid 0, Re = 250,000 94

Figure 75 Downstream intermittency profiles, grid 2, Re = 250,000 94

Figure 76 Downstream intermittency profiles, grid 3, Re = 250,000 95

Figure 77 Upstream boundary layer spectra , $y = y(u'_{max})$, grid 0, Re = 100,000 ...97

Figure 78 Downstream boundary layer spectra, $y = y(u'_{max})$, grid 0, Re = 100,000 97

Figure 79 Upstream boundary layer spectra, $y = y(u'_{max})$, grid 2, Re = 100,000 98

Figure 80 Downstream boundary layer spectra, $y = y(u'_{max})$, grid 2, Re = 100,000 98

Figure 81 Upstream boundary layer spectra, $y = y(u'_{max})$, grid 3, Re = 100,000 99

Figure 82 Downstream boundary layer spectra, $y = y(u'_{max})$, grid 3, Re = 100,000 99

Figure 83 Upstream boundary layer spectra, $y = y(u'_{max})$, grid 0, Re = 250,000 100

Figure 84 Downstream boundary layer spectra, $y = y(u'_{max})$, grid 0, Re = 250,000 100

Figure 85 Upstream boundary layer spectra, $y = y(u'_{max})$, grid 2, Re = 250,000 101

Figure 86 Downstream boundary layer spectra, $y = y(u'_{max})$, grid 2, Re = 250,000 101

Figure 87 Upstream boundary layer spectra, $y = y(u'_{max})$, grid 3, Re = 250,000 102

Figure 88 Downstream boundary layer spectra, $y = y(u'_{max})$, grid 3, Re = 250,000 102

Figure 89 Boundary layer spectra, $y = y(u'_{fs})$, grids 0, 2 and 3, Re = 100,000, x = 2.25 inches, (5.72 cm) 103

Figure 90 Boundary layer spectra, $y = y(u'_{fs})$, grids 0, 2 and 3, Re = 100,000, x = 7.25 inches, (18.42 cm) 103

Figure 91 Boundary layer spectra, $y = y(u'_{fs})$, grids 0, 2 and 3, Re = 250,000, x = 2.25 inches, (5.72 cm) 104

Figure 92 Boundary layer spectra, $y = y(u'_{fs})$, grids 0, 2 and 3, Re = 250,000, x = 7.25 inches, (18.42 cm) 104

Figure 93 Gaster's two parameter bubble bursting criterion, grids 0, 2 and 3, Re = 100,000 107

Figure 94 Modified Roberts' correlation, grids 0, 2 and 3, Re = 100,000 107

Figure 95 Hot-film gage voltage traces, grid 0, Re = 100,000 111

Figure 96 Hot-film gage voltage traces, grid 2, Re = 100,000 112

Figure 97 Hot-film gage voltage traces, grid 3, Re = 100,000 112

Figure 98 Hot-film gage voltage traces, grid 0, Re = 250,000 113

Figure 99 Hot-film gage voltage traces, grid 2, Re = 250,000 113

Figure 100 Hot-film gage voltage traces, grid 3, Re = 250,000 114

Figure 101 X-wire u′ velocity profile, grid 0, Re = 100,000 116

Figure 102 X-wire u′ velocity profile, grid 2, Re = 100,000 117

Figure 103 X-wire u′ velocity profile, grid 3, Re = 100,000 117

Figure 104 X-wire u′ velocity profile, grid 0, Re = 250,000 118

Figure 105 X-wire u′ velocity profile, grid 2, Re = 250,000 118

Figure 106 X-wire u′ velocity profile, grid 3, Re = 250,000 119

Figure 107 X-wire v′ velocity profile, grid 0, Re = 100,000 122

Figure 108 X-wire v′ velocity profile, grid 2, Re = 100,000 122

Figure 109 X-wire v′ velocity profile, grid 3, Re = 100,000 123

Figure 110 X-wire v′ velocity profile, grid 0, Re = 250,000 123

Figure 111 X-wire v′ velocity profile, grid 2, Re = 250,000 124

Figure 112 X-wire v′ velocity profile, grid 3, Re = 250,000 124

Figure 113 Reynolds shear stress profiles, grid 0 Re = 100,000 128

Figure 114 Reynolds shear stress profiles, grid 2 Re = 100,000 128

Figure 115 Reynolds shear stress profiles, grid 3, Re = 100,000.....129

Figure 116 Reynolds shear stress profiles, grid 0, Re = 250,000.....129

Figure 117 Reynolds shear stress profiles, grid 2, Re = 250,000.....130

Figure 118 Reynolds shear stress profiles, grid 3, Re = 250,000.....130

LIST OF TABLES

Table 1 Simulated Low Pressure Turbine Test Matrix 28

Table 2 Scaling Chart for Simulated Low Pressure Turbine Experiment 28

Table 3 Location of Off-Centerline Static Pressure Taps 29

Table 4 Location of Hot-film Gages 30

Table 5 K, Pressure Gradient Parameter, grids 0, 2 and 3, Re = 100,000..... 41

Table 6 K, Pressure Gradient Parameter, grids 0, 2 and 3, Re = 250,000..... 42

Table 7 Streamwise Hot-wire Measurement Locations 54

Table 8 Boundary Layer Properties at Separation, Re = 100,000 84

Table 9 Boundary Layer Properties, Grid 0, Re =100,000..... 84

Table 10 Boundary Layer Properties, Grid 2, Re =100,000..... 85

Table 11 Boundary Layer Properties, Grid 3, Re =100,000..... 86

Table 12 Boundary Layer Properties, Grid 0, Re =250,000..... 87

Table 13 Boundary Layer Properties, Grid 2, Re =250,000..... 88

Table 14 Boundary Layer Properties, Grid 3, Re =250,000..... 89

Table 15 Λ, Longitudinal Integral Length Scale 105

Table 16 Separation Bubble Characteristics, Re = 100,000..... 108

Table 17 Hot-film Gage Test Matrix 111

1. INTRODUCTION

Designing modern gas turbine engines that operate over a wide envelope of flight conditions is a challenging task due to the many constraints that must be properly balanced to ensure high efficiency, low specific fuel consumption and low noise. Engines are designed for peak performance at take-off conditions with allowances made for climb and cruise operation. The performance of an engine at take-off has been well documented in full scale ground tests, but engine performance at cruise (altitude) conditions, especially the behavior of engine components such as the low pressure turbine, is less clear due to limitations of ground test facilities in simulating altitude flight conditions. More than forty different factors influence the performance of low pressure turbines (LPT), but factors such as end wall losses, blade loading, boundary layer behavior and wake passing effects are thought to play major roles. Transition and/or separation may occur along considerable regions of LPT blade surfaces in large gas turbine engines and this effect is amplified at the low Reynolds numbers encountered during altitude flight conditions. LPT efficiency (as much as two points) may be lost if the assumptions made on the state of the boundary layer in the LPT design process are inaccurate. The accurate prediction of the transition and/or separation process can lead directly to improved engine efficiency, lower specific fuel consumption and higher thrust-to-weight ratios. Detailed experimental data regarding boundary layer behavior on LPT blades under the influence of adverse pressure gradients, altitude Reynolds numbers and

varying free-stream turbulence levels is desired to modify existing LPT blade designs and to develop new correlations for use in LPT design systems. A typical turbine blade-row velocity diagram and surface static pressure distribution from Glassman et al., (1972) is shown in Figure 1.

Gardner (1981) and Cherry et al. (1982) performed experimental studies on the effect of loading on LPT blades as part of the NASA funded Energy Efficient Engine Technology Program. This experimental program, along with others, showed when designed properly, highly loaded blades exhibit higher performance than blades designed with a lower loading profile. As a consequence of this, modern LPT blades are now designed to be more highly loaded and have lower aspect ratios than their predecessors. This trend in blade design philosophy further complicates the transition problem by introducing severe adverse, as well as favorable, pressure gradients into the flow field experienced by the blades. Because of the complexity of the flow field, more systematic and well controlled experiments are required to help improve modeling and computational analyses of boundary layer transition as it occurs in a LPT. The purpose of this work is to develop a comprehensive set of experimental data to improve LPT blade design and modeling systems.

Methods for predicting boundary layer growth in laminar and turbulent flows have improved over the years, however, in the last five years more research has been directed towards understanding the laminar-turbulent transition process, especially within gas turbine engines. Binder et al. (1988) state that the prediction of the state of the boundary layer is important and dramatic advances in modeling an computational analyses are required to achieve this. Blair (1982) also discusses the importance of

predicting the state of the boundary layer and the interaction of the free-stream turbulence and pressure gradient in turbomachinery flows. Computational fluid dynamic methods are increasingly being used to model flows over blading, but the transition and/or turbulence models incorporated into these methods often do not contain adequate physics to accurately predict the state of the boundary layer. Mayle (1993) lectured on the importance of understanding the transition process in gas turbine engines, Walker (1993) amplified many of the same issues presented by Mayle (1991, 1993). Mayle made several suggestions as to how LPTs should be designed. These suggestions may be summarized as follows:

1) High turbulence levels should be used in experiments to correctly model transition and separation.

2) To properly calculate turbine airfoil transitional flows, models must be able to compute forward and reverse (relaminarization) transition in addition to wake induced transition.

3) Calculation of separated flow transition and massive separation in LPTs at low Reynolds numbers must include the modeling of laminar, transitional and turbulent shear layer flows near and away from the surface.

4) The variation of the pressure gradient parameter K to critical pressure gradient K_{crit} as a function of Reynolds should be considered in the design process.

5) The forcing of a short, separated, flow transition by a local change in blade shape (curvature) should be considered by designers as a method of controlling transition in LPTs.

Halstead et al. (1995) performed an extensive experimental and computational study of

boundary layer development on the suction surface of airfoils in an embedded stage of a LPT and compressor and this study revealed that laminar flow can persist over anywhere from 30 and 40 percent of the suction surface length. Since modern LPT airfoil designs are more aggressive (higher loadings, lower aspect ratios, etc.), an airfoil with significant laminar flow along its suction surface may suffer significant performance losses from boundary layer separation due to adverse pressure gradients and/or wake passing effects. Research performed by Ashworth et al. (1985); Baughn et al. (1995); Cumpsty (1995); Gostelow and Walker (1990); Gostelow et al. (1992); Hall and Gibbings (1972); Hodson et al. (1993); Johnsen et al. (1965); Mayle (1993); Rivir (1996) Schulte and Hodson (1994); Sharma (1987); Simon and Ashpis (1996); Wisler (1985) also investigated wake passing and pressure gradient effects on boundary layer behavior in compressors in addition to high and low pressure turbines. Additionally, Dixon (1978) discusses other important factors in designing turbomachinery components.

Minimizing losses in the LPT over its entire operating range is the designers ultimate challenge and having detailed knowledge of how the boundary layer behaves is of paramount importance in the design process. The purpose of this experimental study is to develop a comprehensive experimental database that can be used to improve LPT design systems. This study will provide data on transitional as well as separated flow fields if they occur. Additionally, this data will allow for the improvement of transition and turbulence models for CFD applications.

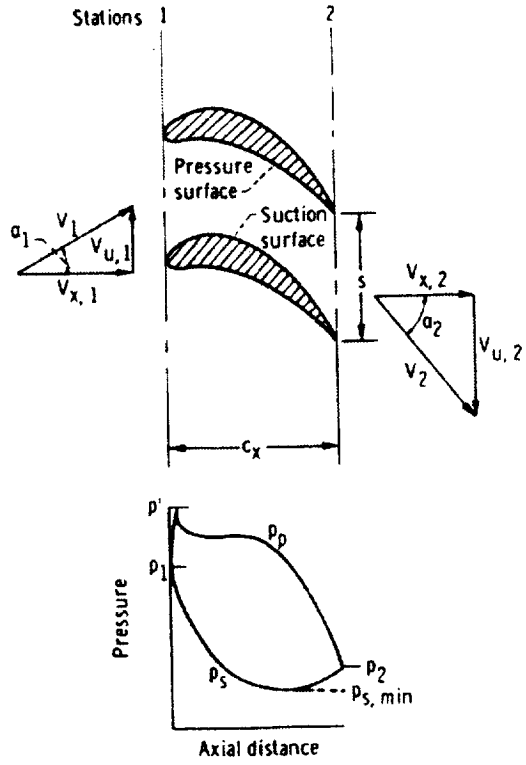

Figure 1 Typical turbine blade-row velocity diagram and surface static pressure distribution

II. BACKGROUND

A. Low Pressure Turbine Flow Physics

In November 1993, a workshop on bypass transition was held at the NASA Lewis Research Center. Attendees at this workshop included representatives from academia, the aircraft engine industry and government agencies. The aircraft engine industry expressed the need for shifting the research focus from studying bypass transition in turbomachinery to the investigation of boundary layer behavior in low pressure turbines. A performance degradation in efficiency in a low pressure turbine of approximately 2% occurs as the aircraft accelerates from take-off to cruise flight conditions and industry is interested in identifying the physics involved in this performance loss. This performance loss is primarily dictated by the operating Reynolds number which varies from 450,000 to 180,000 for take-off and cruise flight conditions, respectively. The Reynolds number is based upon the LPT exit velocity and blade suction surface length. Separation, wake passing effects and transition are three major physical mechanisms that may singularly or collectively affect the losses in a LPT. The understanding of separation on a LPT blade is important due to the potential presence of separation bubbles and the mechanics of the bubble (e.g., burst, growth, etc.). Wake passing effects can have a significant impact on the boundary layer causing separation and/or transition. Lastly, the modes of transition must be identified such as bypass, transition in separation bubbles and calmed regions, and turbulent spot dynamics. All of the aforementioned physical mechanisms are

affected by Reynolds number, free-stream turbulence intensity, pressure gradient and reduced frequency. This research is part of a collaborative NASA/Industry/Academia Low Pressure Turbine Flow Physics Program.

B. Boundary Layer Behavior

Figure 2 shows a boundary layer on a typical turbine blade. The boundary layer starts developing from the leading edge of the blade with a small finite thickness and grows along the pressure and suction surfaces. Initially the boundary layer is laminar, but soon becomes transitional due to viscous effects and free-stream disturbances (turbulence). Also, viscous effects contribute to the change to transition as illustrated in Figure 3. On the upper surface of the blade the flow is subjected to adverse or rising pressure which, in turn, leads to a region of separated flow or reversed flow. Chang (1970) describes this separation as stalling and this phenomena can be connected with closed separation bubbles. Separation bubbles may be short or long and both affect the flow in different ways. If the bubble is short, it usually is enclosed and points of separation and reattachment can be identified; however, a short bubble can also break down (burst) and this can lead to a stall condition with an attendant increase in drag and loss of lift. If the bubble is long, the pressure distribution along the airfoil changes slightly, but this flow breakdown does not lead to a complete separation; instead, the separated flow passes over the body surface and reattaches further downstream. If the flow undergoes transition, it encounters weak disturbances (Tollmien-Schlichting waves) which are amplified and this leads to random fluctuations in the flow that have turbulent characteristics. Figure 3 shows a separated flow region occurring in a laminar

boundary layer. Separation can also occur in a turbulent boundary layer, but a turbulent boundary layer is more resistant to separation because it contains more energy. The flow separates due to a decrease in free-stream velocity which translates into a static pressure rise along the rear section of the suction surface of the turbine blade. This results in a positive pressure gradient (or adverse pressure gradient, $\frac{dP}{dx} > 0$) which decelerates the flow in the boundary layer which enables a flow reversal. The flow in the boundary layer is retarded to such an extent that very close to the wall, the flow starts to move in a direction opposite to the mean flow. The point at which the flow starts to reverse itself is the separation point and this phenomena is referred to as separation. At the separation point, the velocity gradient $\left(\frac{\partial u}{\partial y}\right)_{y=0} = 0$. Figure 4 is a schematic of transition events on a turbine airfoil. This combination of flow phenomena includes a separation bubble that can reattach itself to the surface as a turbulent boundary layer as shown in Figure 4 or may burst if the Reynolds number is low enough. Malkiel and Mayle (1995) and Tani (1964) have also investigated the behavior of separation bubbles.

The boundary layer can be mathematically modeled by the continuity equation and a reduced set of the Navier-Stokes equations derived by Prandtl and found in Schlichting (1959), White (1974) and Anderson (1991). The boundary layer equations for two-dimensional steady flow of an incompressible fluid are:

$$\frac{\partial u}{\partial x} + \frac{\partial v}{\partial y} = 0,$$

$$u\frac{\partial u}{\partial x} + v\frac{\partial u}{\partial y} = -\frac{1}{\rho}\frac{dp}{dx} + \nu\frac{\partial^2 u}{\partial y^2},$$

$$u_e\frac{du_e}{dx} = -\frac{1}{\rho}\frac{dp}{dx},$$

with boundary conditions y = 0: u =0, v=0 ; y = ∞: u = U(x). From an examination of

Prandtl's boundary layer equations and considering the relationship of the pressure gradient $\frac{dP}{dx}$ to the velocity distribution u(x,y) or $u_e(x)$, it can be concluded that for steady flow, separation can only occur in the presence of an adverse pressure gradient. Restating this in a slightly different manner, an adverse pressure gradient is a necessary, but not sufficient condition for separation. Figure 5 shows the velocity profile, gradient and curvature profiles for a decelerating flow which corresponds to an adverse (positive) pressure gradient and a turbine blade pressure distribution plot which illustrates regions of favorable (negative), as well as adverse pressure gradient.

The largest losses in a turbine can be attributed to the boundary layer that builds up on the blade and end-wall surfaces, Glassman et al. (1972). These boundary layer losses are comprised of friction drag from the flow of viscous fluid over the surfaces, profile (pressure) drag that results from fluid flow past the trailing edge of the blade and mixing of low velocity boundary layer fluid with high velocity free-stream fluid downstream of the blade rows.

C. Computational Efforts

The LPT blade geometry used in this study is shown in Figure 6. The surface pressure distributions along the blade pressure and suction surfaces are shown in Figure 7. An inviscid panel code developed by McFarland (1982, 1984) was used to compute the blade pressure distribution which is fairly benign. The blade geometry was supplied by the Pratt & Whitney Aircraft Engine Company. The geometry is representative of the blade design and loadings used in modern LPT stages. This blade geometry was then used as the basis for designing a test section for the NASA Lewis experimental test facility, CW-7, for conducting the LPT flow physics research. The test section is two-

dimensional in nature and consists of contoured upper and flat lower walls. The contoured upper wall was used to generate a pressure distribution along the flat lower wall that corresponds to the pressure distribution along the suction surface of the generic blade. This wall contour was created by matching the mass flow from the generic LPT blade cascade through a flow channel with a contoured upper wall and flat plate lower wall. The inviscid panel code was used initially to compute the flow-field of the LPT cascade geometry shown in Figure 6. The velocity and pressure distributions computed by the panel code are a function of the area change through the channel. The suction surface velocity distribution was then expressed as a function of suction surface length of the generic blade. This function was used to correctly match the suction surface pressure distribution shown in Figure 7 by utilizing the continuity equation. The following form of the one-dimensional continuity equation was used to obtain a relation for the upper wall contour:

$$\rho VA = \text{constant},$$

(where $A = y_c w \cos \alpha$) .

The width of the test section is constant and the flow angle α, is assumed to be zero. Thus the one dimensional continuity equation can be written as

$$\rho V_X A_X = \rho V_2 A_2,$$

$$\rho V_X y_c w_X = \rho V_2 y_2 w_2.$$

For Mach numbers (M << 1) the flow is assumed to be incompressible, which yields

$$V_X y_c w_X = V_2 y_2 w_2,$$

or

$$V_X (y_o - y_b) = V_2 y_2,$$

(where $y_c = y_o - y_b$) .

Rearranging and solving for y_b yields

$$y_b = y_o - y_2\left(\frac{V_2}{V_x}\right).$$

The quantity $\frac{V_2}{V_x}$ was computed from the $\frac{V}{V_2}(s)$ distribution obtained from the generic LPT blade and continuity was applied to yield a new test section geometry with a contoured upper wall and a flat plate as shown in Figure 8. The pressure distributions from this new test section design and the generic LPT airfoil are shown in Figure 9.

Diffusion factors (the diffusion factor is the ratio of the exit velocity to the local velocity, Johnson and Bullock, 1965) were computed for the contoured upper wall and showed that the flow would separate. The new test section geometry was then analyzed using the NPARC full Navier-Stokes computational code described in the NPARC user's guide (1994). The analysis of the test section contour was performed to validate the effect of contoured upper wall (proper lower pressure distribution) as well as, to identify transition and/or separated flow regions. The NPARC analysis did reveal a small separation region just downstream of the minimum area (i.e., throat) on the contoured upper wall (Figure 10) and a suction system was added to the upper wall to alleviate this problem.

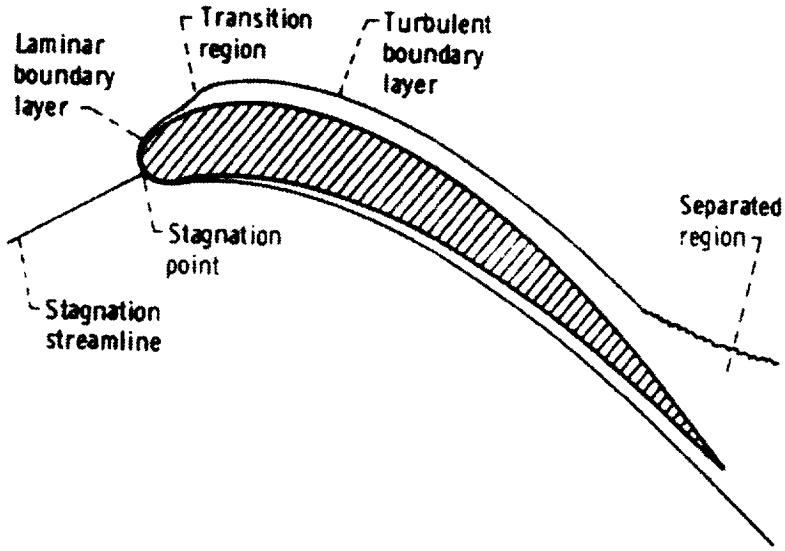

Figure 2 Boundary layer development on a turbine blade

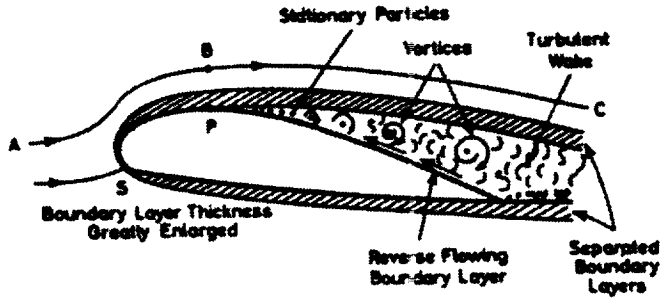

Figure 3 Viscous effects in flow around an airfoil

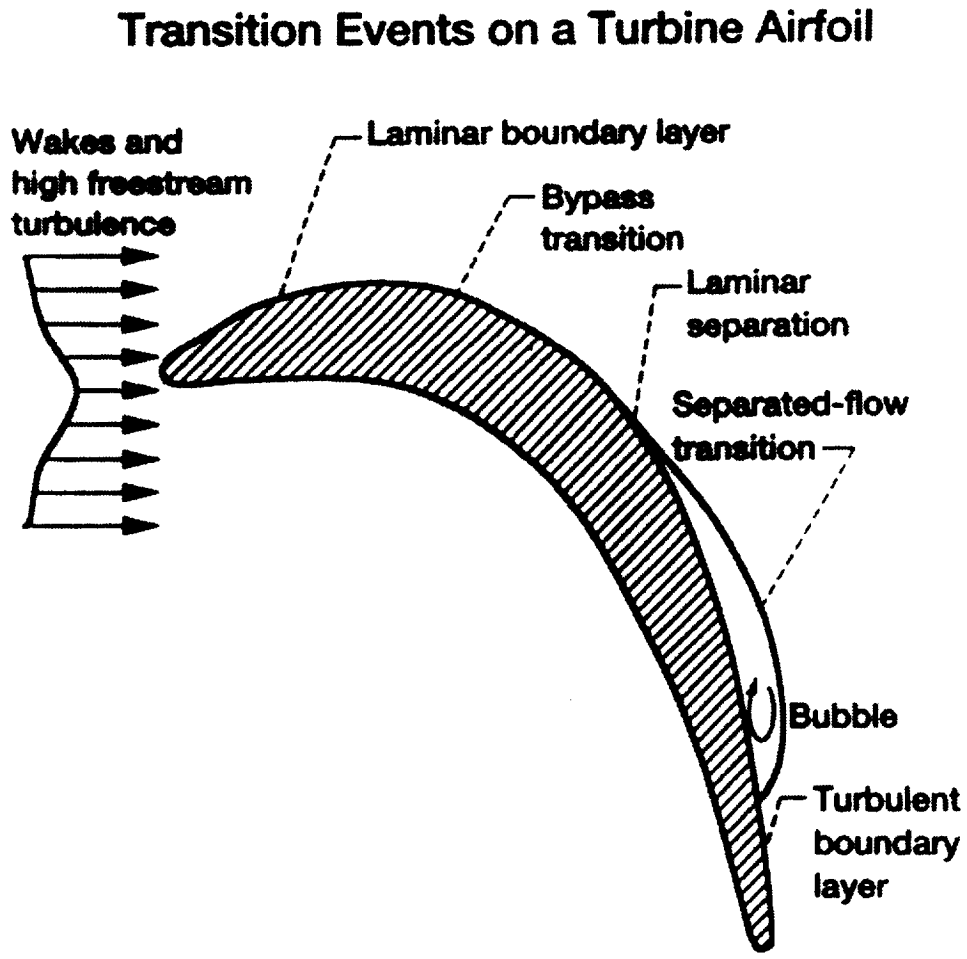

Figure 4 Transition events on a turbine airfoil (Laminar separation and reattachment)

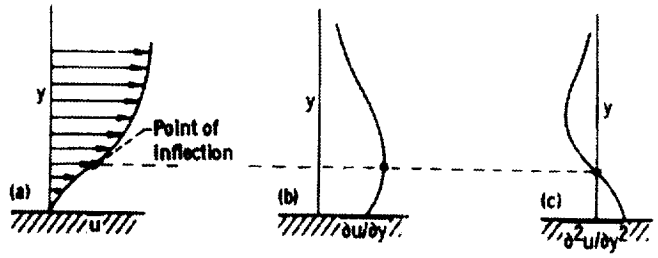

(a) Velocity profile. (b) Velocity gradient. (c) Velocity-profile curvature.

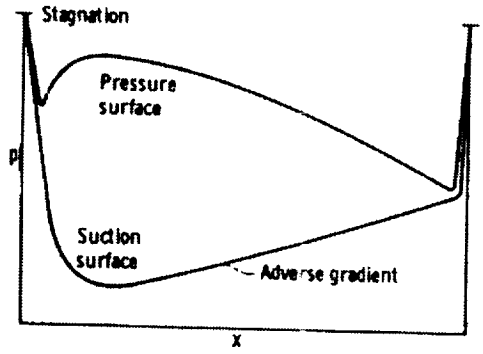

Figure 5 Separated flow velocity profile, velocity gradient and velocity curvature and pressure distributions

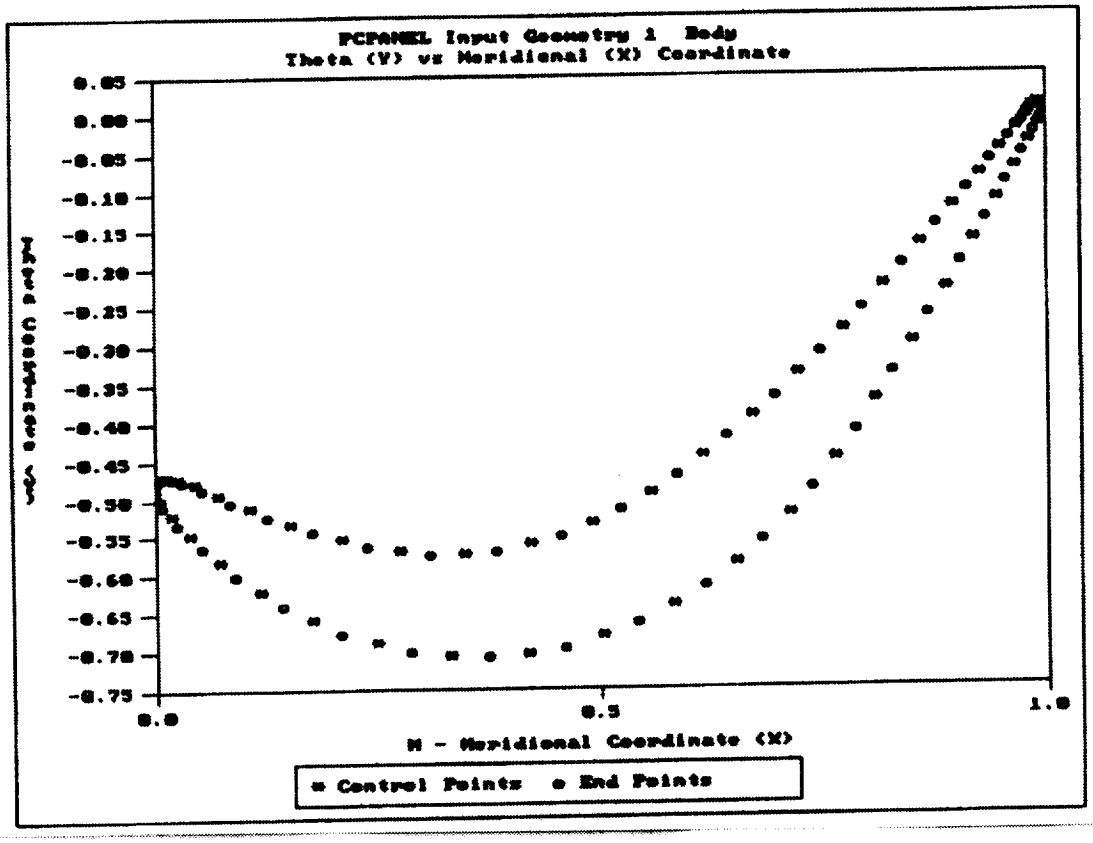

Figure 6 Generic low pressure turbine (LPT) blade*

*Note: Drawing is not to scale.

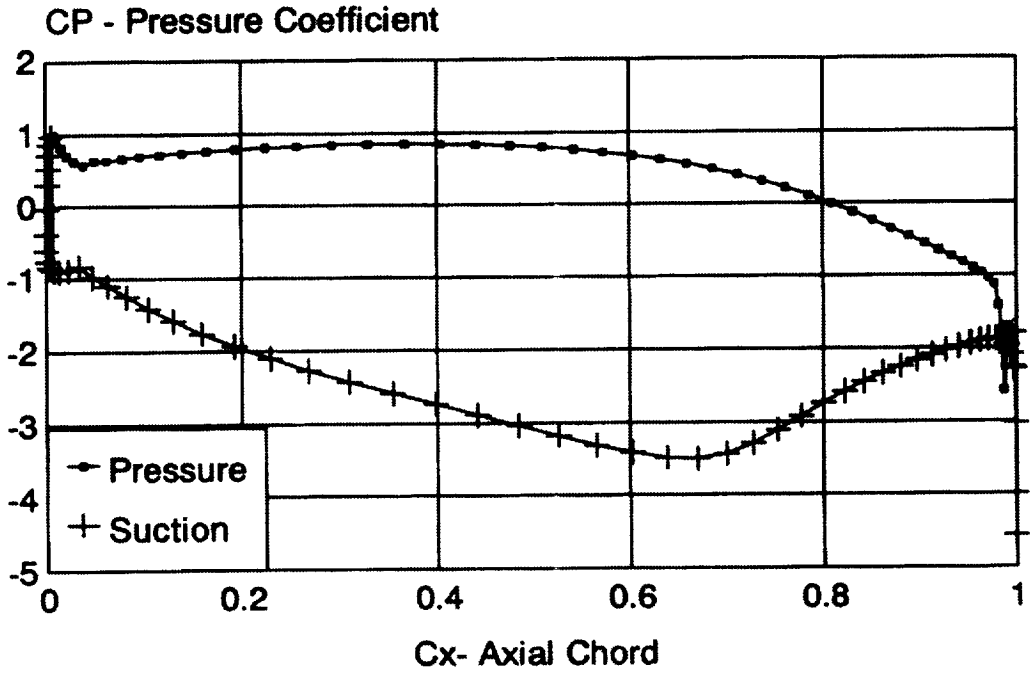

Figure 7 Generic low pressure turbine blade (LPT) Panel code pressure distribution

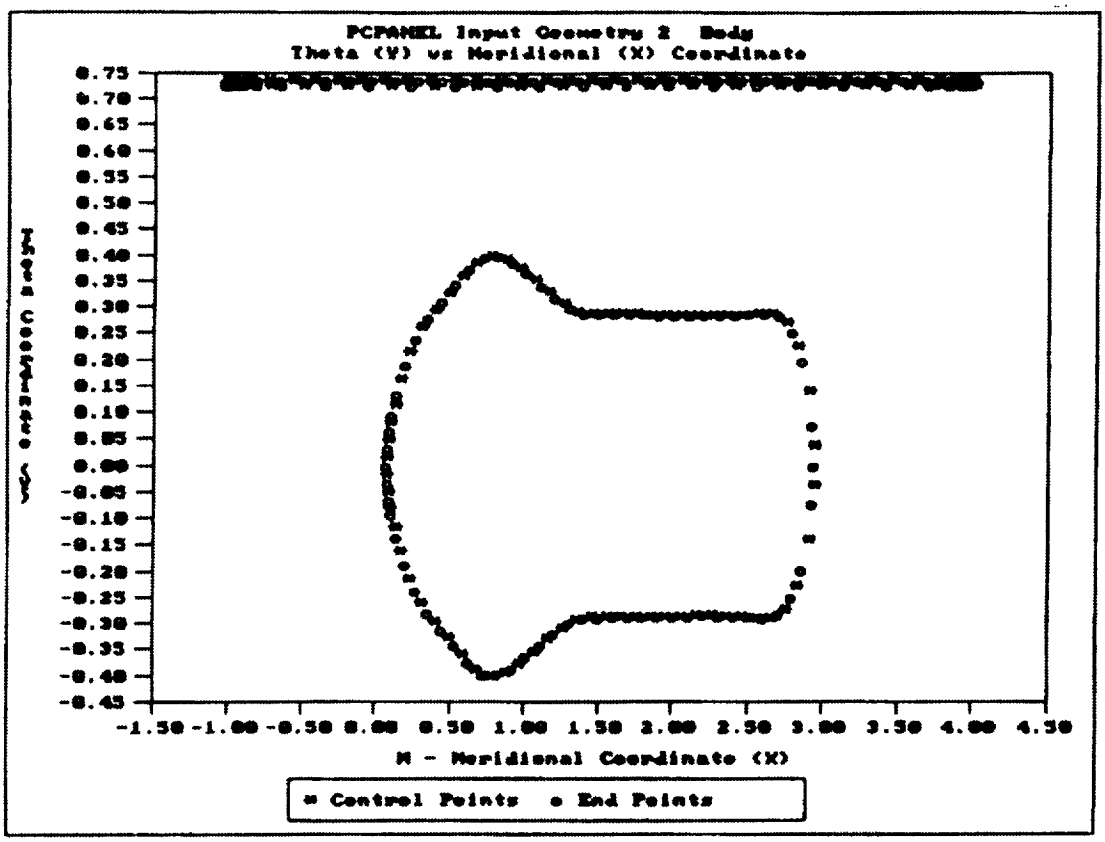

Figure 8 Panel code simulated low pressure turbine test section geometry*

*<u>Note</u>: Drawing is not to scale.

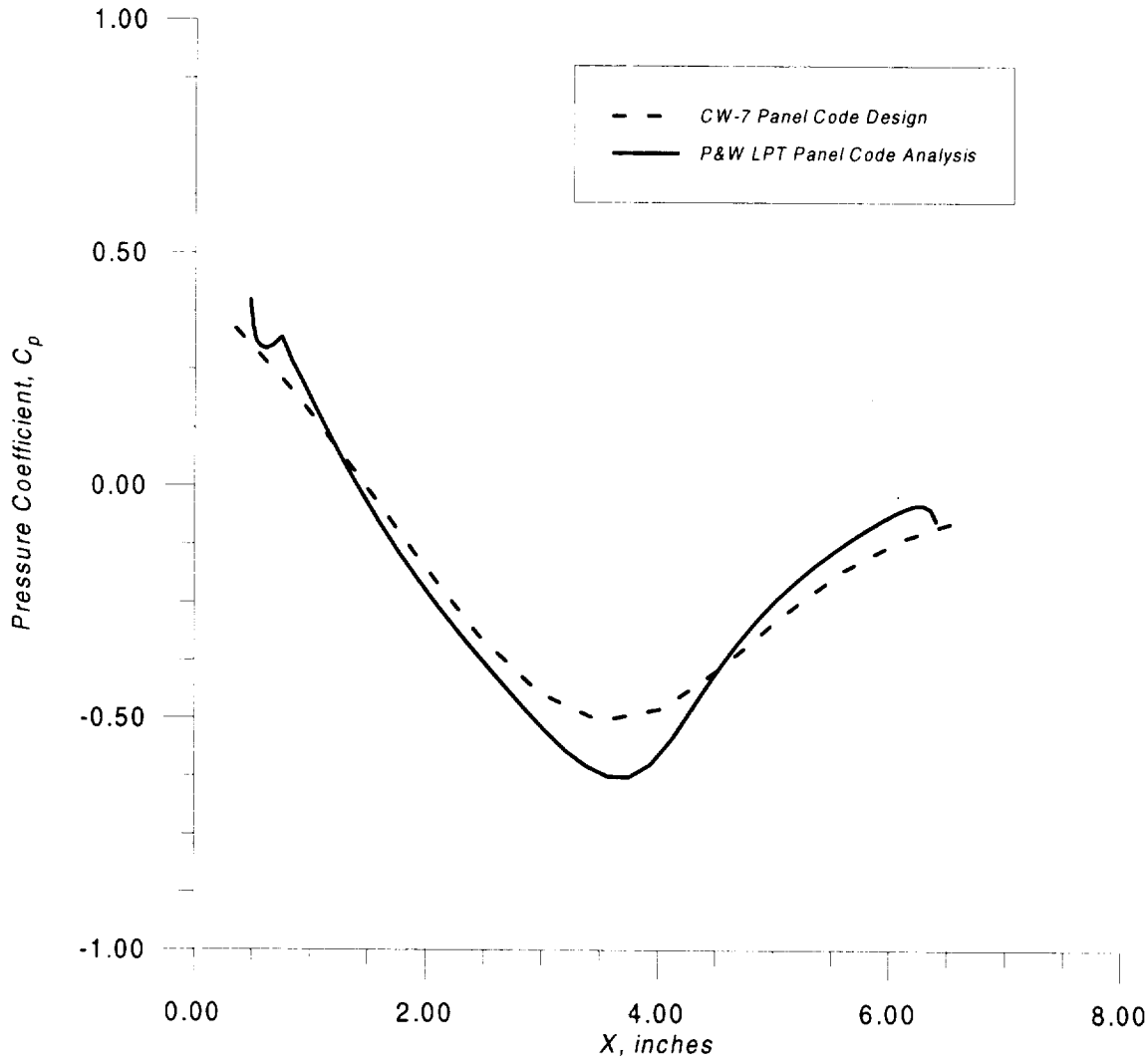

Figure 9 Comparison of LPT blade and simulated LPT lower wall Panel code pressure distributions, Re = 250,000

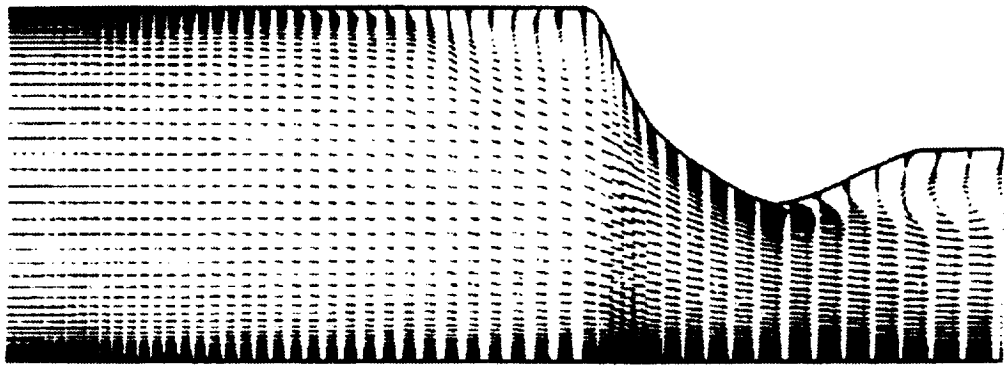

Figure 10 NPARC velocity contour plot of simulated LPT test section

III. RESEARCH FACILITY

A. Boundary Layer Transition Tunnel

A parametric investigation of low pressure turbine boundary layer transition was performed in the boundary layer transition tunnel, test facility CW-7, at the NASA Lewis Research Center. The research facility is a low-speed closed loop wind tunnel that was designed to investigate two-dimensional, incompressible, large-scale boundary layers. The effects of free-stream turbulence and pressure gradient on boundary layer behavior can be investigated in this facility. A schematic of the boundary layer research facility is shown in Figure 11. This wind tunnel consists of nine major components which are the blower, flow conditioner with turbulence grids, two dimensional convergent nozzle, bleed scoops, test section with variable upper wall, diffuser, air heater, air filter and air cooler. Facility operating conditions (velocity, temperature, pressure gradient, and free-stream turbulence) can be controlled through the adjustment of the previously mentioned wind tunnel components. This facility has been previously used for bypass transition studies on an unheated and heated flat plate by Suder et al. (1988) and Sohn et al. (1991), respectively.

A Chicago Blower Corporation, SISW Class III SQA centrifugal fan with capacity of 10,000 cubic feet per minute (283.2 cubic meters per minute) is used to provide the main flow to the tunnel. The blower flow rate is controlled by a vortex valve located at the blower inlet. After the air flow exits the blower, the air enters a flow

conditioning plenum chamber, which removes flow irregularities generated by the blower and reduces the free-stream turbulence levels. The plenum chamber consists of 1) perforated plate baffles, which distributes the distorted air flow from the blower across the entire plenum, 2) a series of honeycombs and soda straw arrays, which straighten the flow, and 3) a series of fine mesh screens which reduce the tunnel free-stream turbulence level.

The tunnel free-stream turbulence levels can be changed by the use of turbulence generating grids which can be inserted at the exit of the flow conditioning section, just upstream of the contraction nozzle. Locating the turbulence grids upstream of the contraction nozzle allows the generated turbulence to become more homogeneous and have a lower decay rate along the test section length (Blair et al., 1981). The turbulence grids consist of rectangular bar arrays with approximately 62% open area yielding a square mesh. Four grids were designed to generate test section turbulence levels from 0.25 to 6 percent. Grids 0, 2 and 3 (0.8%, 2% and 3% free-stream turbulence intensity, respectively) were used for this experiment. Table 1 contains the test matrix with the turbulence levels and Reynolds numbers used in this experiment. A more detailed description of the wind tunnel components including the turbulence grids can be found in Suder et al. (1988).

B. Test Section

The test section of the Boundary Layer Research Tunnel has a rectangular cross section that measures 27 inches (68.58 cm) wide, 12 inches (30.48 cm) long and 6 inches (15.24 cm) high. The test section consists of a flat lower wall, two vertical sidewalls and

a removable upper wall. The contoured upper wall which matches the pressure gradient generated by the suction surface of the generic LPT blade was designed and installed in the test section to replace the existing straight upper wall. The contoured wall was used to match the operating environment of a LPT blade and to study the effects of favorable and adverse pressure gradients and free-stream turbulence. A porous wall bleed system for suction was added to the contoured upper wall to prevent flow separation on the upper surface and to induce separation on the lower wall. Interchangeable wall bleed sections were used in the bleed system and these sections can be porous or solid. The total number of 1/8 inch (0.3175 cm) diameter holes for these configurations were 171, 271 and 362, respectively. Flow visualization was used to verify the test section flow, suction system effectiveness and suction flow rates.

In order to properly match the Reynolds numbers in a full scale LPT, a splitter plate (which also functioned as the flat lower wall) was inserted in the center of the test section (approximately 3 inches (7.62 cm) from the floor). The test section flow bifurcation was required due to operating limitations of the tunnel blower. Operating the tunnel blower at low flow settings was unstable and bifurcating the test section allowed the blower to be operated at a higher flow setting which yielded stable flow rates that match typical LPT cruise and take-off Reynolds numbers based on test section length and exit velocity (100,000 and 250,000, respectively). Table 2 was used to scale the size of the new test section. The leading edge of the splitter plate has a 4:1 elliptical cross section and a 1.5 inch (3.81 cm) long flap was attached to the end of the plate to help control the location of the stagnation point. The plate is 27 inches (68.58 cm) wide and 14 inches (35.56 cm) long. Additionally, the flap was positioned at an angle of attack

which fixed the stagnation point on the top surface of the splitter plate. Figure 12 is a schematic of the new contoured wall test section. The double bleed scoop assembly positioned at the bottom wall of the original test section entrance was not used in the tests reported herein. A suction system was added to the contoured upper wall to prevent separation and is shown in Figure 12. Figures 13 and 14 are photographs of the simulated LPT test section installed in the boundary layer transition tunnel and of the simulated LPT test section from inside the tunnel.

A probe traversing mechanism was used to position the hot-wire probes for making detailed boundary layer measurements in the vertical, streamwise, and spanwise directions relative to the flow direction. This specially designed traversing system referred to as PACS (Probe Actuation Control System) can be precisely positioned via a computer controlled actuation system and may be positioned in increments as small as 0.00033 inches (8.382×10^{-4} cm). Streamwise and spanwise positioning of the hot-wire probe is performed by moving the probe through streamwise and spanwise slots situated along centerline and off centerline locations in the contoured upper wall.

C. Flow Visualization

Flow visualization was used to qualitatively analyze the flow through the test section. Smoke traces were generated using a thin nichrome wire connected to a power supply and a smoke wire and camera control unit. Traces were performed at tunnel velocities between 5-10 ft/sec (1.524-3.048 m/sec) to minimize the diffusion of the smoke and to allow visualization of the flow-field. The nichrome wire was located in the inlet flow measurement station of the tunnel just upstream of the entrance to the test

section. The nichrome wire was pulled out of the tunnel and swabbed with a thin layer of oil (model train smoke fluid) and then placed back into the tunnel air flow. The smoke wire and camera control unit were then used to synchronize the timing of voltage supplied to the wire, the duration of the burn to generate smoke, as well as to control camera and flash units if desired. The duration of the burn time for the majority of the traces was two seconds and a voltage of 16-20 volts was used to burn the oil. The smoke traces were visually observed using a strobe flash unit and photographed with a 35 mm camera with two fast recovery flash units. Additionally, tufts were installed on the contoured upper wall during testing to verify that the flow on the upper wall remained attached. Photographs of the flow visualization will be presented later in the Results and Discussion section.

D. Instrumentation

Static pressure taps, hot-film gages and hot-wire probes (single and x-wire) were used to make flow field measurements. Velocity signals from a single wire probe were monitored on a digital oscilloscope and mean and fluctuating (rms) values were measured with a personal computer (PC) based constant temperature, anemometry system. Detailed descriptions of the test section instrumentation, hot-wire probes and constant temperature anemometry systems are given in the following sections.

1. Steady-State Instrumentation

Free-stream flow conditions at the test section inlet and exit planes are measured with a Pitot tube and thermocouple located at the center span of the test section.

These measurements were used to determine the free-stream velocity, temperature and mass flow. Additionally, static pressures taps are located spanwise off the center line as well as streamwise along the bifurcated test plate to measure the spanwise and streamwise pressure gradients impressed upon it by the contoured upper wall. A total of 36 static taps were used to instrument the test plate. Figure 15 shows the layout of the static taps on the flat test plate and Table 3 contains the locations of the taps situated 1 inch (2.54 cm) off the centerline.

2. Dynamic Instrumentation

Three different types of hot-wire probes were used for this experimental investigation, two single wire probes and an x-wire probe:

1) A commercially available TSI model 1218-t1.5 single sensor boundary layer probe was used to measure the streamwise component of the mean and fluctuating (rms) velocity. The safety leg of the single sensor probe was removed to allow surveys as close to the wall as possible.

2) A Dantec model 55P11 straight general purpose type probe was used with a special probe support to make boundary layer measurements upstream of the throat. This is a miniature wire probe made of tungsten wire with a diameter of 0.000197 inches (5 μm), length of 0.0492 inches (1.25 mm) and a prong length of 0.197 inches (5 mm).

3) A Dantec model 55P63 x-wire probe was used to simultaneously measure the instantaneous streamwise and vertical velocity components. These measurements provide data for the determination of the Reynolds shear stresses. This is also a miniature probe made of tungsten wire with a diameter of 0.000197 inches (5 μm), length of 0.0492

inches (1.25 mm), wire separation of 0.0394 inches (1 mm) and total prong length of 0.4882 inches (12.4 mm). This is an x-array probe, 90°, with its sensor plane parallel to the probe axis.

The x-wire probe was designed to have excellent spatial resolution and measurement capabilities. This probe was designed with a small separation distance between the wires to properly resolve small scale near wall turbulence (viscous length scale approximately of 0.004331 inches (11 μm) for the worst case of a fully turbulent boundary layer) without significant eddy averaging in the spanwise direction. To minimize heat conduction from the support prong and vertical averaging in the shear flow, a short sensing length must be used. These two constraints require the use of a miniature probe with small wires.

Hot-film gages were used to identify turbulent spot patterns, while the hot-wire and x-wire probes were used to measure the mean and rms velocities, as well as the Reynolds shear stress throughout the boundary layer, respectively.

The hot-film gages are TSI model 1237 standard flush mounted platinum sensors and these sensors are suitable for one-dimensional measurement of wall shear stress without disturbing the flow. The flat plate was instrumented with these hot-film gages along the centerline of the plate starting at 1.5 inches (3.81 cm) from the plate leading edge with spacing of 0.5 inch (1.27 cm) for the first 11 gages, followed by a gage spaced 1.0 inch (2.54 cm), further , followed by two gages spaced 2.0 inches (5.08 cm) apart as shown in Figure 15 and listed in Table 4. The hot-film gages were clustered in the region where the change in adverse pressure gradient has the greatest affect on the boundary

layer and the transition process.

A Dantec Streamline constant temperature anemometer system was used to operate the hot-film gages and hot-wire probes. The Streamline system used for this experiment consisted of a frame and six anemometer modules with signal conditioners incorporated. The frame can incorporate up to six anemometer modules and each module has galvanically separated power supplies for electrical noise protection and to prevent crosstalk between measured velocity components. Three bridge configurations are available from the software and each anemometer has a 20:1 general purpose bridge that includes compensation for 16.41 foot (5 m) and 65.62 foot (20 m) cables. Each bridge has two top resistance values, 20 and 10 Ohm. The 20 Ohm top resistance can be used with all standard probes and the 10 Ohm top resistance is used for high power applications (the 20 Ohm top resistance value was used for this experiment). A 1:1 symmetrical bridge ensures high system bandwidth and minimum noise and is intended for use in flows with fluctuating temperatures in conjunction with temperature compensated probes. This bridge is also needed for test setups that include long cables, high-impedance probes, or probes with negative temperature coefficients. The overheat resistor, cable compensation, probe resistance measurement circuit and amplifier parameters can be optimized by the user or set to a fully automatic mode. The signal conditioner contained in each anemometer module allows optimal signal adaptation to the analog/digital (A/D) converter in the 486 personal computer and had programmable input offset and gain. The variable input offset and gain allows for the investigation of very low turbulence levels in steady flows. High-bypass filters can be applied when analyzing turbulence levels in unsteady flows. Additionally, the hot-wire probes were calibrated

using a Dantec calibration module (that replaces an anemometer module in the frame) and Flow Unit. The calibration, calibration module and Flow Unit are discussed in detail in the calibration section of this thesis.

Table 1 Simulated Low Pressure Turbine Test Matrix

Grid	Tu	Re = 100,000	Re = 250,000
0	0.8%	X	X
2	2.0%	X	X
3	3.0%	X	X

Table 2 Scaling Chart for Simulated Low Pressure Turbine Experiment

Test section inlet height	Scale factor	Test section length	Re_{TSL}	Exit velocity	Inlet velocity
3.0 in. (7.62 cm)	4.11	11.97 in. (30.4 cm)	100,000 (cruise)	29.13 ft/sec (9.56 m/s)	19.82 ft/sec (6.50 m/s)
3.0 in. (7.62 cm)	4.11	11.97 in. (30.4 cm)	250,000 (take-off)	72.81 (23.89 m/s)	44.04 (14.45 m/s)

Table 3 Location of Off-Centerline Static Pressure Taps

Tap Number	Axial Location* , inches
1	1.0 (2.54 cm)
2	1.5 (3.81 cm)
3	2.0 (5.08 cm)
4	2.5 (6.35 cm)
5	3.0 (7.62 cm)
6	3.5 (8.89 cm)
7	4.0 (10.46 cm)
8	4.5 (11.43 cm)
9	5.0 (12.70 cm)
10	5.5 (13.97 cm)
11	6.0 (15.24 cm)
12	6.5 (16.51 cm)
13	7.0 (17.78 cm)
14	8.0 (20.30 cm)
15	9.0 (22.86 cm)
16	10.0 (25.40 cm)
17	11.0 (27.94 cm)
18	12.0 (30.48 cm)

***Note:** Distance from leading edge. Taps are offset 1 inch (2.54 cm) from centerline in spanwise direction.

Table 4 Location of Hot-film Gages

Gage Number	Axial Location, inches*
1	1.0 (2.54 cm)
2	1.5 (3.81 cm)
3	2.0 (5.08 cm)
4	2.5 (6.35 cm)
5	3.0 (7.62 cm)
6	3.5 (8.89 cm)
7	4.0 (10.46 cm)
8	4.5 (11.43 cm)
9	5.0 (12.70 cm)
10	5.5 (13.97 cm)
11	6.0 (15.24 cm)
12	7.0 (17.78 cm)
13	9.0 (22.86 cm)
14	11.0 (27.94 cm)

***Note:** Distance from leading edge. Gages located on centerline of flat plate.

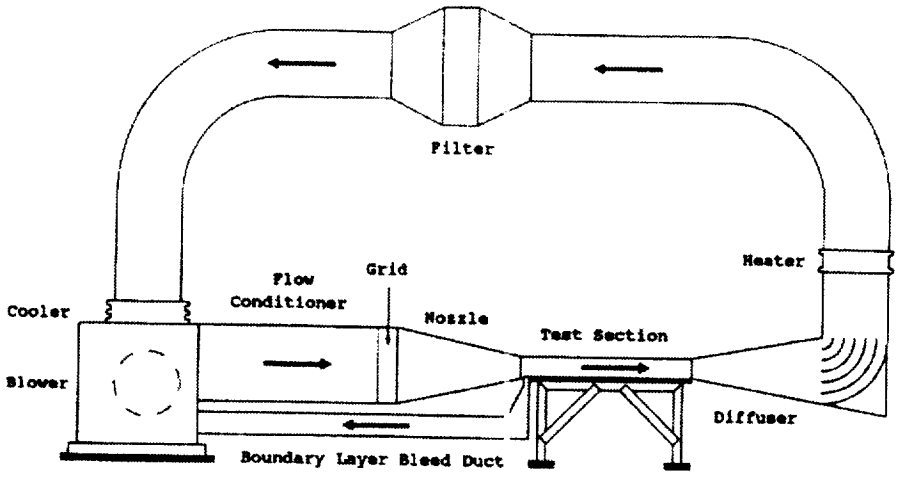

Figure 11 Schematic diagram of unmodified boundary layer transition tunnel

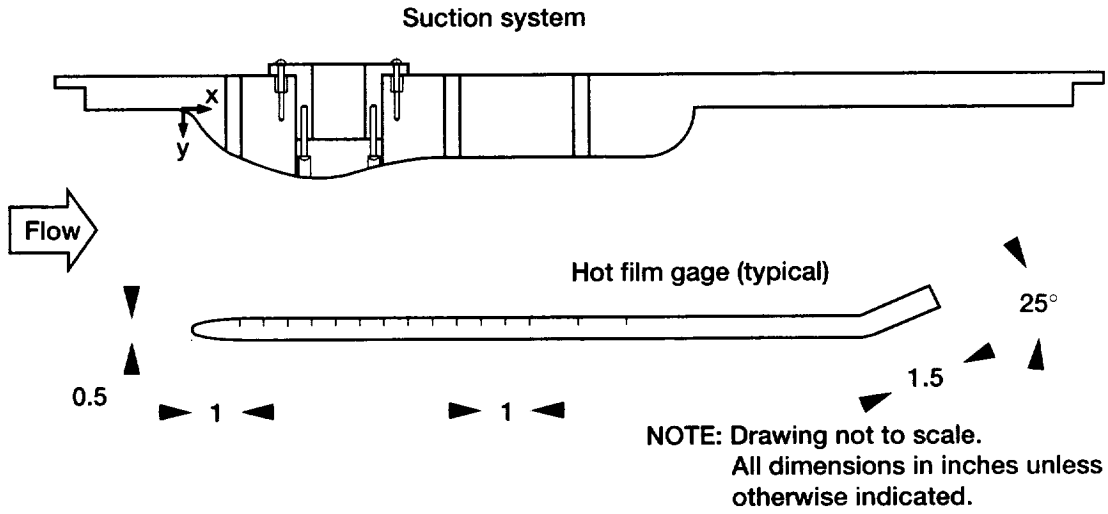

x	0.00000	0.25000	0.38007	0.41542	0.46054	0.52728	0.60429	0.68840	0.77711	0.86292	0.95349
y	0.00000	0.06667	0.14264	0.22245	0.29850	0.39879	0.49147	0.59047	0.68539	0.76987	0.84932

x	1.05089	1.15307	1.26895	1.38835	1.52370	1.66092	1.80703	1.95376	2.10131	2.24904	2.38700
y	0.92223	0.98827	1.05117	1.10709	1.16304	1.21432	1.26672	1.31734	1.36792	1.41792	1.46481

x	2.52542	2.65217	2.78008	2.90179	3.02482	3.14910	3.27399	3.40641	3.53850	3.67882	3.81840
y	1.51018	1.54955	1.58503	1.61328	1.63528	1.64905	1.65517	1.65257	1.64268	1.62593	1.60385

x	3.96434	4.10962	4.26152	4.41305	4.56412	4.71519	4.86378	5.01266	5.15955	5.30678	5.43854
y	1.57651	1.54566	1.51055	1.47370	1.43624	1.39897	1.36362	1.32954	1.29786	1.26775	1.24083

x	5.57100	5.70549	5.84060	5.99427	6.14799	6.30642	6.46490	6.62375	6.78259	6.94165	7.10066
y	1.21755	1.20138	1.19120	1.18860	1.19005	1.18992	1.18972	1.18901	1.18806	1.18711	1.18612

x	7.25979	7.41893	7.57798	7.73704	7.89596	8.05485	8.21366	8.37242	8.53102	8.68962	8.84809
y	1.18504	1.18397	1.18285	1.18178	1.18070	1.17971	1.17880	1.17797	1.17723	1.17665	1.17623

x	9.00657	9.16492	9.32323	9.48137	9.63951	9.79757	9.95559	10.11345	10.27130	10.42899	10.58668
y	1.17603	1.17594	1.17611	1.17652	1.17718	1.17814	1.17938	1.18091	1.18281	1.18521	1.18802

x	10.72472	10.86277	10.98257	11.10221	11.21172	11.32008	11.42251	11.52206	11.61734	11.70791	11.79372
y	1.19166	1.19356	1.19298	1.18719	1.17512	1.15518	1.12690	1.08968	1.04315	0.98798	0.92405

x	11.87337	11.94682	12.01295	12.07122	12.12142	12.16240	12.19499	12.22394	12.23449
y	0.85259	0.77372	0.68869	0.59858	0.50375	0.40690	0.30690	0.15537	0.00149

Figure 12 Schematic diagram of simulated low pressure turbine test section with upper wall coordinates*

*__Note:__ 1 inch = 2.54 cm

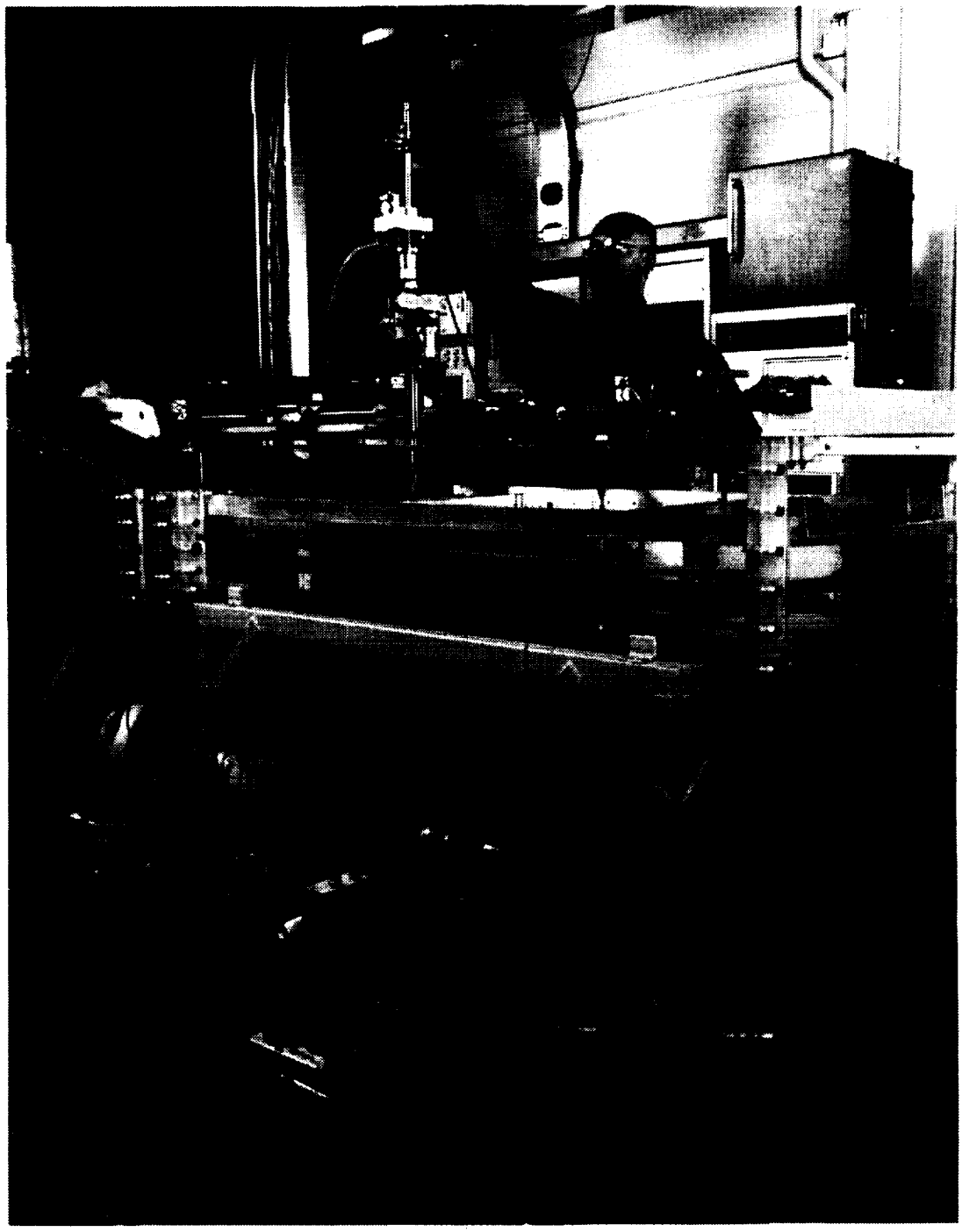

Figure 13 Photograph of boundary layer transition tunnel with simulated low pressure turbine test section

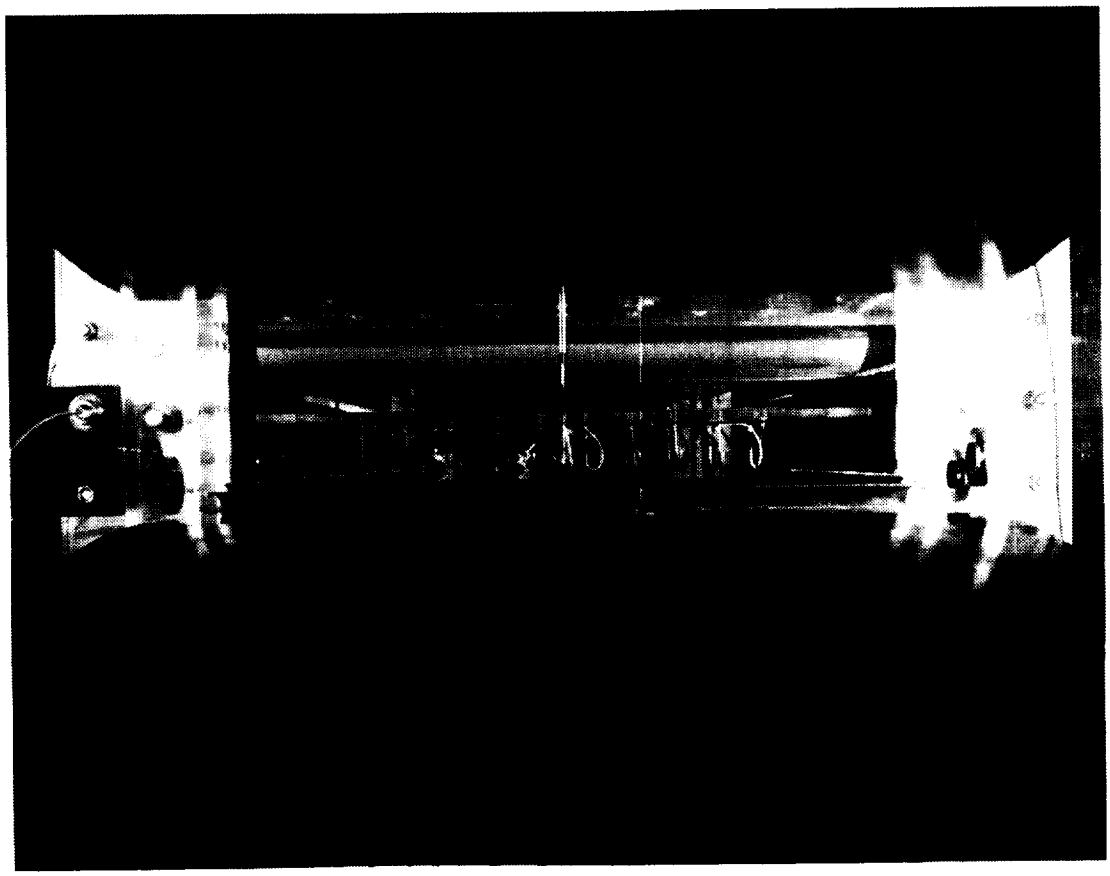

Figure 14 Photograph of simulated low pressure turbine test section from inside and upstream of boundary layer transition tunnel

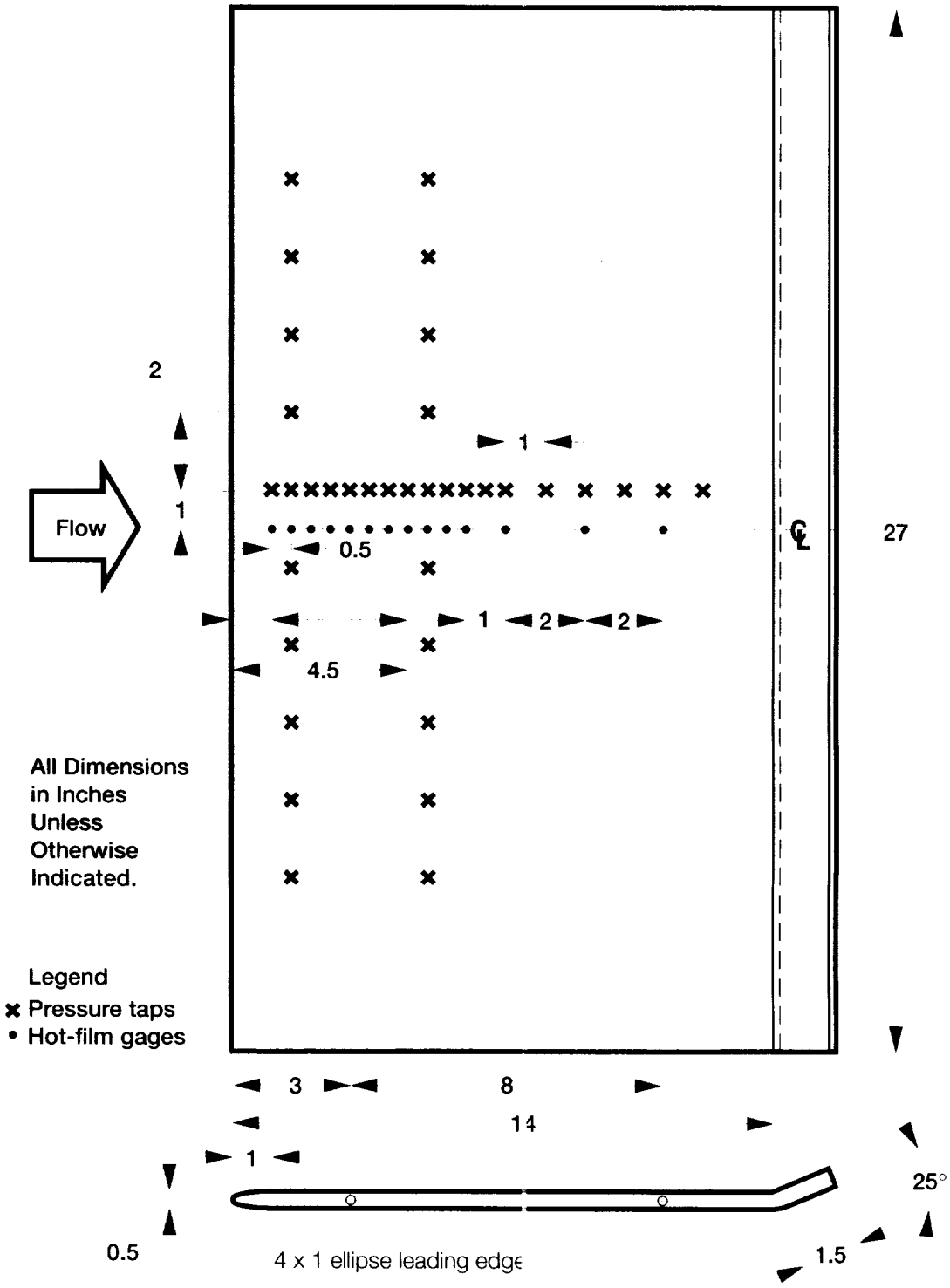

Figure 15 Schematic diagram of simulated low pressure turbine test section lower wall*

*Note: 1 inch = 2.54 cm

IV. DATA ACQUISITION

A. Steady-State Data

Steady state tunnel conditions, i.e., free-stream velocity, pressure, temperature and wall static pressures were monitored and recorded using a ESCORT D multichannel data acquisition system. The ESCORT D system provides real time data acquisition, display and control capability for the boundary layer transition tunnel. The ESCORT D system can be used to obtain data from a variety of modular instrumentation devices and the system is run on a facility dedicated DEC Micro-VAX computer. This system consists of a remote acquisition microprocessor, data input and output device, 256 multiplexing digitizer and a personal computer. The Escort D system is described in detail in Blaha (1993).

Steady state pressures were measured using an PSI Electronic Scanning Pressure (ESP) system which is capable of measuring pressure to ± 0.5 psi (3447.5 N/m^2). The ESP system is composed of a 32 channel module, separate transducer for each module, and is networked to the ESCORT system. Three 15 psi (103,425 N/m^2) modules were used for this experiment. Additionally, individual Setra pressure transducers were used for the inlet and exit pitot tube static and total pressure measurements. The Setra transducers are capable of measuring a differential pressure difference as low as 7.5 inches of water (1868.25 N/m^2) and 15 inches of water (3736.5 N/m^2) for the pitot static and total pressure measurements, respectively.

B. Unsteady Data

Time averaged mean and rms velocity data were acquired using a PC based Dantec Streamline constant temperature anemometer system. The data acquisition process and data reduction for the constant temperature anemometry were controlled using a Gateway 2000 series 486, 60 Mhz personal computer with a National Instruments AT-MIO-16E-1, 1.2 MHz, E series data acquisition (DAQ) board and SC-2040 simultaneous sample and hold accessory. This hardware setup was used to make all of the single wire, X wire and hot-film gage measurements.

A Nicolet Scientific Corporation model 660a dual channel FFT analyzer featuring a 1024 point, 12 bit analog-to-digital signal conversion with a maximum sampling rate of 100 kHz was used to acquire spectral data. Spectral data was obtained at a sampling rate of 12.8 kHz using an average of 100 scans.

Instantaneous velocity signals were also monitored using a Tektronix model 7603, digital oscilloscope that was used to sense the bridge output signal. A Hewlett-Packard Laserjet IV printer was used for data plotting as well as ESCORT screen prints.

C. Calibration

1. Hot-wire Calibration

Hot-wire calibrations are based on King's law (Perry 1982, Lomas 1986, and Holman 1978) as given in Equation (1):

$$E^2 = A + BU^n. \qquad (1)$$

E represents the bridge output voltage of the constant temperature anemometer, U is the velocity of the air flowing across the wire, A and B are constants calculated from the

calibration and n is the power of the selected exponential. The Dantec Streamline hot-wire anemometry system was used to calibrate both single and x-wire probes. The user can select a fourth order polynomial or a power law curve fit option of King's law in the Streamware software as described in Streamline User's Guide (1994). A fourth order polynomial fit was used for all of the calibrations performed during this experiment.

The Streamline system has a calibration module and Flow Unit which contains calibrated flow nozzles, a pressure transducer and temperature measurement sensor. The Flow Unit was connected to the Streamline frame via the calibration module and a shop air supply line was connected. The nozzles for the Flow Unit can calibrate flows with velocities ranging from 1.574 ft/s (0.5 m/s) up to Mach 1. Calibration of probes were performed automatically utilizing the Streamline system, Flow Unit and supporting software. A typical hot-wire calibration curve generated from Streamware is shown in Figure 16.

2. Hot-film Calibration

The calibration procedure for the hot-film gages was significantly more complicated than the procedure used for the hot-wire probes. The flush mounted hot-film gages were calibrated to indicate the wall shear stress and this was done by measuring the skin friction as described by Bellhouse and Schultz (1966). A relationship of the form

$$\tau_w^{1/3} = AE^2 + B$$

exists for a constant temperature anemometer, where τ_w is the wall shear stress, E is the bridge output voltage and A and B are constants determined from the calibration.

This calibration procedure may lead to large errors in determining the calibration constants as well as in skin friction in flows where large wall shear stress fluctuations occur as in the transitional boundary layer region. For this experiment the hot-film probes were not calibrated and were used for qualitative measurements only.

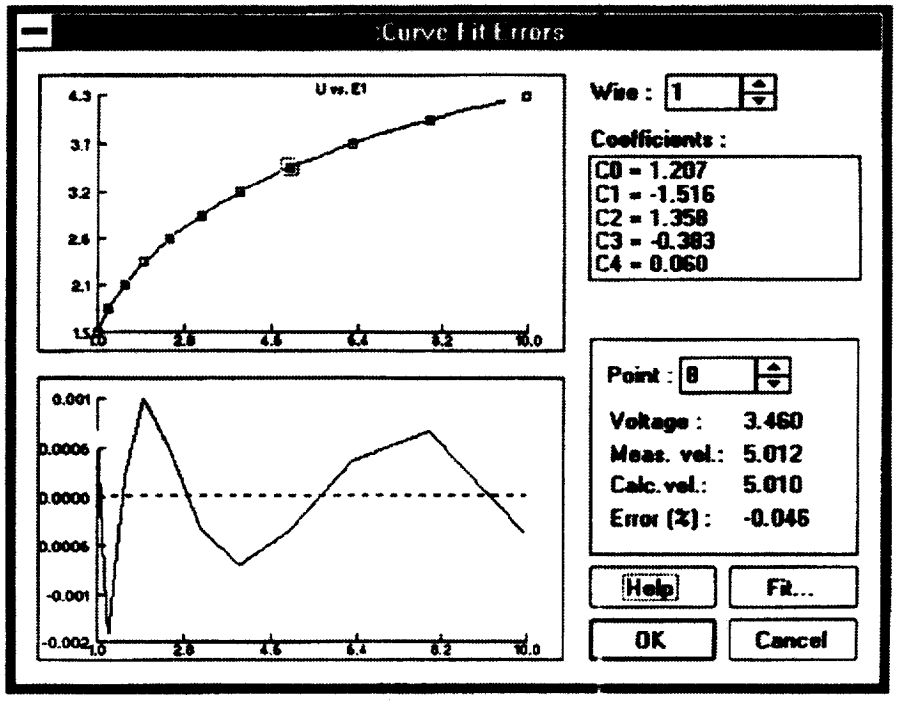

Figure 16 Sample Streamline hot-wire probe calibration curve

V. RESULTS AND DISCUSSION

A. Characterization of Flow

The flow within the simulated LPT test section can be characterized by the pressure gradient parameter K. The pressure gradient parameter is defined by the following equation

$$K = \frac{\nu}{U_\infty^2}\frac{dU_\infty}{dx} \quad ,$$

where ν is the kinematic viscosity of the working fluid, U_∞ is the free stream velocity and x is the axial or streamwise distance from the leading edge of the body. The K parameter is equal to a constant for many geometries, but for a converging-diverging geometry such as a typical airfoil it varies with streamwise distance. Tables 5 and 6 contain summaries of the K parameters computed for the simulated LPT test section for Reynolds numbers of 100,000 and 250,000, respectively. Plots of this parameter are contained in Figures 17 and 18. It was determined by Mayle (1991) that the flow on the suction surface of a typical LPT airfoil will separate for a critical K parameter less than -4×10^{-6} at a critical Reynolds number of less than 100,000 (based on axial chord). Figure 17 shows that a region of the flow is separated for a Reynolds number equal to 100,000 for the three turbulence intensity levels tested. Separation does not occur for a Reynolds number equal to 250,000 at any turbulence intensity level because the K parameter and Reynolds number values exceed the critical K and Reynolds number values as shown in Figure 18.

The flow within the test section can also be characterized by examining the variation of the edge velocity. Figure 19 is a plot of the edge velocity variation for a Reynolds number of 100,000. This plot shows that the flow in the test section accelerates up to a maximum velocity near the throat at an axial location of approximately 4.25 inches (10.80 cm). Once the flow proceeds past the throat, the flow velocity then decreases as the flow proceeds downstream and it continues to decrease until it reaches a constant value in the constant area portion of the test section. The flow behavior is consistent for the three turbulence levels tested. The edge velocity variation for a Reynolds number of 250,000 behaves in a similar manner to that of the 100,000 Reynolds number case except a constant value does not occur in the constant area portion of the test section. Figure 20 shows the edge velocity variation for a Reynolds number of 250,000.

Table 5 K, Pressure Gradient Parameter, grids 0, 2 and 3, Re = 100,000

x, inches	Grid 0 (0.8% TI)	Grid 2 (2% TI)	Grid 3 (3% TI)
1.75 (4.45 cm)	1.058E-05	1.520E-05	1.510E-05
2.25 (5.72 cm)	1.240E-05	1.290E-05	1.510E-05
2.75 (6.99 cm)	8.347E-06	9.590E-06	1.170E-05
3.25 (8.26 cm)	1.027E-06	4.730E-06	5.830E-06
3.75 (9.53 cm)	-8.785E-07	-4.570E-07	1.340E-06
4.25 (10.80 cm)	-2.460E-06	-2.240E-06	-3.770E-06
4.75 (12.07 cm)	-4.170E-06	-1.960E-06	-5.420E-06
5.25 (13.34 cm)	-2.775E-06	-1.870E-06	-3.020E-06
5.75 (14.61 cm)	-1.846E-06	-2.770E-06	-5.010E-06
6.25 (15.88 cm)	-4.383E-06	-6.120E-06	-5.570E-06
6.75 (17.15 cm)	-6.737E-06	-7.680E-06	-2.160E-06
7.25 (18.42 cm)	-2.985E-06	-4.130E-06	-8.750E-07
7.75 (19.69 cm)	0.000E+00	-2.310E-07	-4.430E-07
8.25 (20.96 cm)	2.488E-07	0.000E+00	0.000E+00
8.75 (22.23 cm)	2.488E-07	-2.310E-07	----*
9.25 (23.50 cm)	4.944E-07	-4.650E-07	0.000E+00

***Note:** No data taken at this streamwise location for this condition.

Table 6 K, Pressure Gradient Parameter, grids 0, 2 and 3, Re = 250,000

x, inches	Grid 0 (0.8% TI)	Grid 2 (2% TI)	Grid 3 (3% TI)
1.75 (4.45 cm)	5.830E-06	5.870E-06	5.100E-06
2.25 (5.72 cm)	5.070E-06	4.160E-06	4.910E-06
2.75 (6.99 cm)	4.290E-06	3.360E-06	4.240E-06
3.25 (8.26 cm)	2.790E-06	2.940E-06	2.720E-06
3.75 (9.53 cm)	1.110E-06	1.350E-06	1.170E-06
4.25 (10.80 cm)	-1.360E-07	-3.280E-07	2.800E-08
4.75 (12.07 cm)	-6.420E-07	-8.220E-07	-5.110E-07
5.25 (13.34 cm)	-6.580E-07	-6.970E-07	-5.530E-07
5.75 (14.61 cm)	-7.340E-07	-8.660E-07	-6.510E-07
6.25 (15.88 cm)	-9.660E-07	-1.020E-06	-9.460E-07
6.75 (17.15 cm)	-8.190E-07	-8.680E-07	-1.080E-06
7.25 (18.42 cm)	-9.280E-07	-9.540E-07	-1.120E-06
7.75 (19.69 cm)	-1.140E-06	-1.340E-06	-1.170E-06
8.25 (20.96 cm)	-1.000E-06	-1.120E-06	-9.820E-07
8.75 (22.23 cm)	---*	---*	---*
9.25 (23.50 cm)	-1.280E-06	-8.370E-07	-7.890E-07

***Note:** No data taken at this streamwise location for this condition.

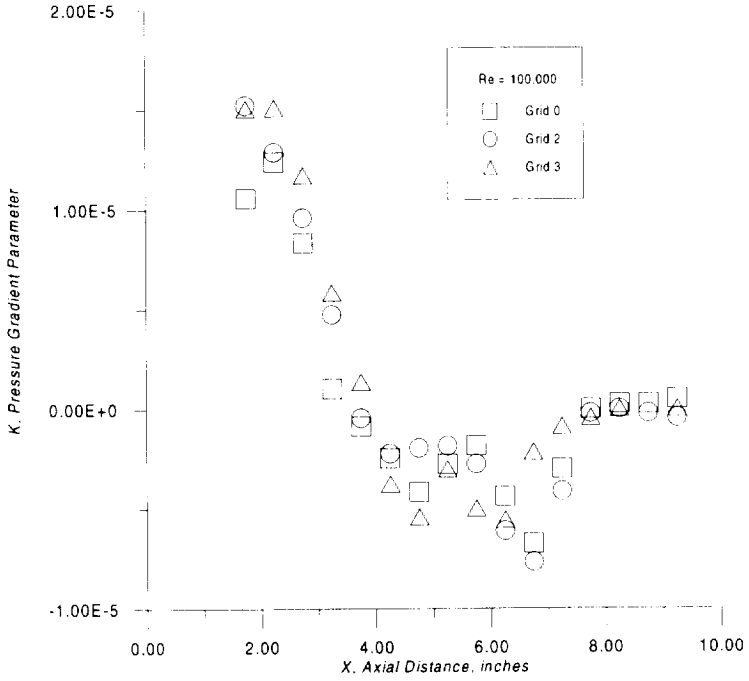

Figure 17 K, pressure gradient parameter, grids 0, 2, and 3, Re = 100,000

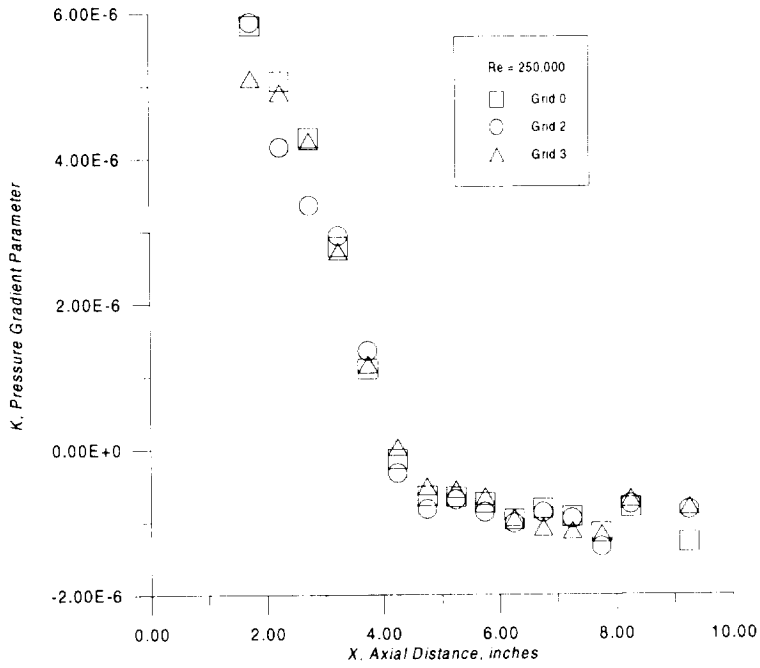

Figure 18 K, pressure gradient parameter, grids 0, 2, and 3, Re = 250,000

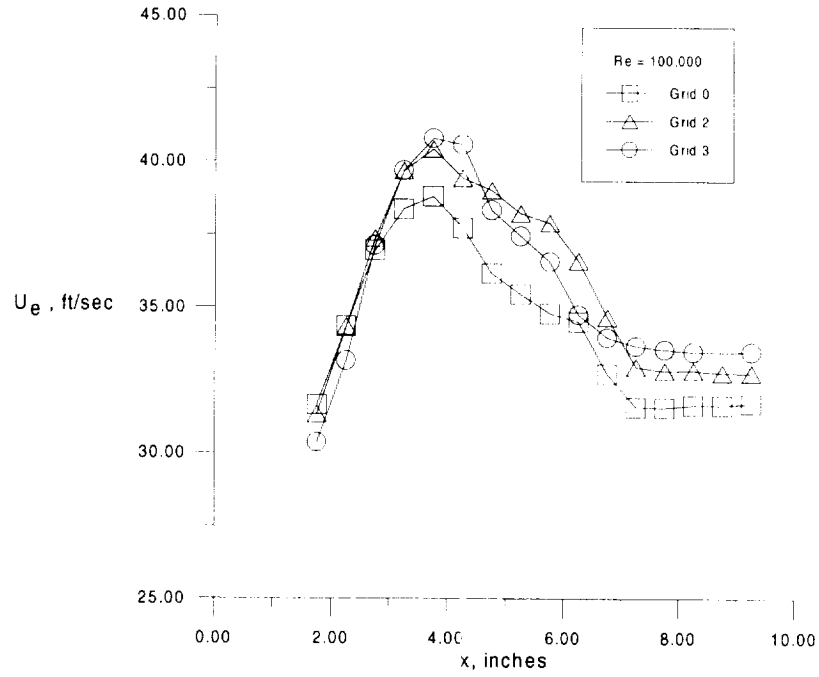

Figure 19 Edge velocity variation, grids 0, 2 and 3, Re = 100,000

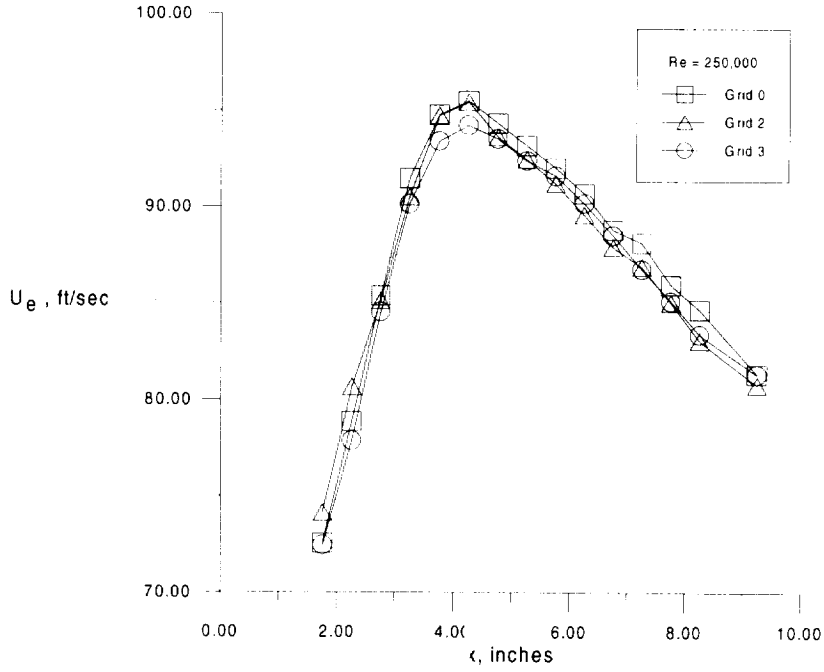

Figure 20 Edge velocity variation, grids 0, 2 and 3, Re = 250,000

B. Flow Visualization Data

Smoke wire flow visualization was conducted to capture the qualitative features of the flow field. Photographs of smoke traces were taken and used to validate the ability of the panel code generated contoured upper wall of the test section to mimic the flow physics of the generic LPT blade. The flow visualization was performed with grid 0 at a Reynolds number of 50,000 (based on an exit velocity of 15 ft/s (4.921 m/s), which is lower than a typical cruise Reynolds number. Due to rapid dispersion of the smoke at higher Reynolds numbers and intense mixing with higher turbulence levels, good quality photographs could not be obtained for higher Reynolds numbers and higher turbulence conditions.

Figure 21 is a smoke trace photograph of flow through the test section without suction. The photograph shows a region of separated flow on the upper wall that was previously predicted by the NPARC code. This photograph again verified the need for suction to prevent flow separation on the upper wall. Figure 22 contains smoke trace photographs with the upper wall suction turned on. These photographs are a time lapse sequence that clearly show a separation bubble on the lower wall and attached flow on the upper wall. The photographs show the absence of smoke in the region between the separated shear layer and the test surface within the front part of the separation bubble and this is due to infinitesimal viscous shear stresses. The flow-fields in this so-called 'dead-air' region look similar in each photograph, which indicates that the laminar region of the separation bubble is steady. However, the flow pattern in the region downstream of the maximum bubble height is substantially different than the one in the upstream laminar bubble region. This is evidence that the transition and reattachment

processes are unsteady. A large eddy structure is clearly seen in the photographs downstream from the maximum bubble height in the shear layer. These eddies eventually become unstable and, through interaction with each other, finally develop into a turbulent boundary layer. This transition process is similar in behavior to a laminar free shear layer flow, where discrete spanwise vortices form due to a Kelvin-Helmholtz instability and eventually break down into a fully turbulent shear layer. A detailed flow visualization study performed by Morin and Patrick (1991) also revealed this eddy formation in the shear layer. The presence of this separation bubble on the lower wall is a key parameter in the simulation of the generic LPT blade and these photographs help to validate that the test geometry generated by the panel code does indeed mimic the flow physics of the generic blade. During testing at Reynolds numbers of 100,000 and 250,000, tufts revealed that the upper wall flow stayed attached for all test conditions and suction flow rates tested. If the separation bubble shown in the photographs starts to burst at low Reynolds conditions in a real LPT, huge losses in performance will result.

Figure 21 Photograph of flow visualization without suction, grid 0, Re = 50,000

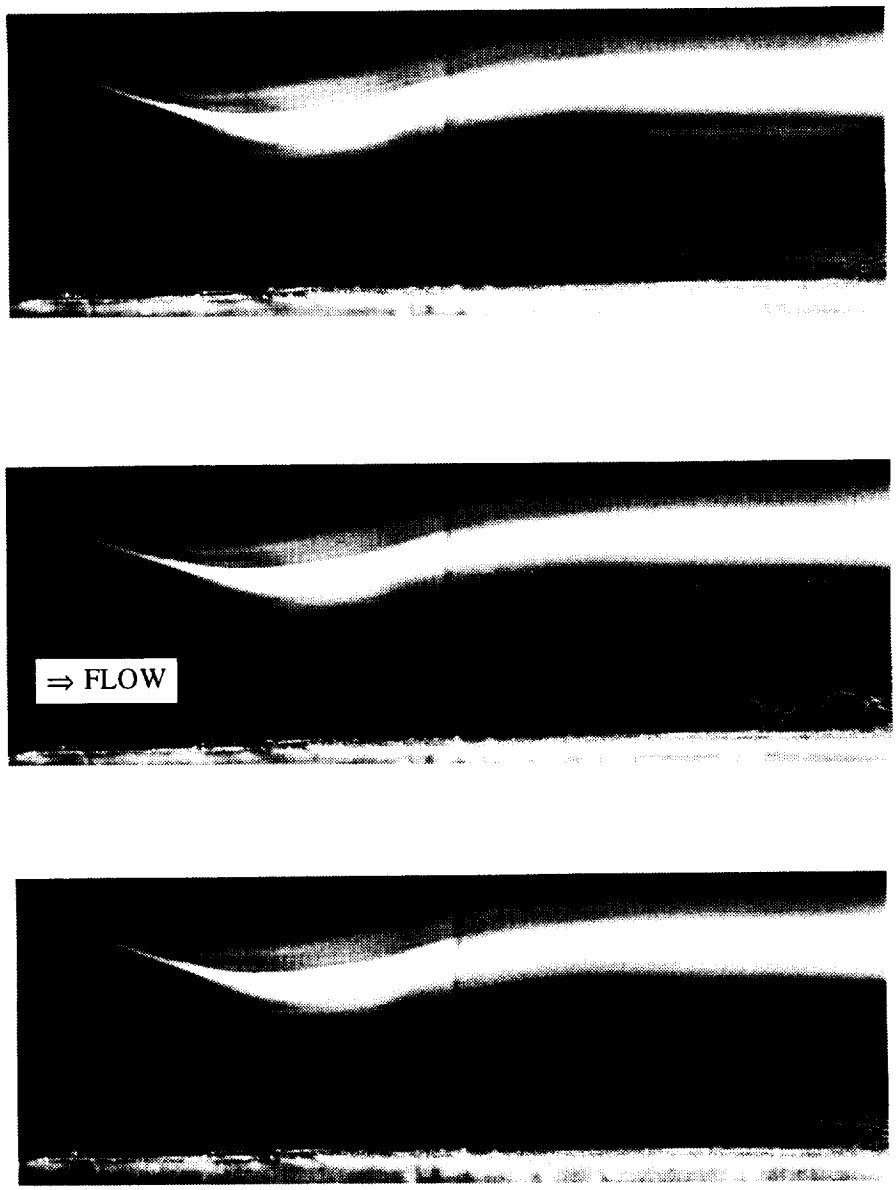

Figure 22 Photographs of flow visualization with suction, grid 0, Re = 50,000

C. Establishment of Test Conditions

Results from the flow visualization study were used to determine the proper amount of suction flow and to verify the existence of a separation bubble on the

lower wall. Since the flow visualization studies were performed at velocities lower than the actual test condition velocities, a methodology for determining the proper suction flow rates at the test conditions had to be determined. This methodology consists of setting the tunnel flow to the cruise Reynolds number flight conditions, varying the free-stream turbulence levels and suction mass flow rates and using tufts as the flow visualization technique. The procedure that was used is as follows: First, set tunnel flow to a Reynolds number of 100,000, increase the free-stream turbulence level, and decrease the suction mass flow rate to match the inviscid pressure distribution on the flat plate which defines an upper suction flow limit; second, remove the turbulence grids and increase the suction flow rate to define a lower suction flow limit identified by the tufts flow visualization. If too much suction is applied for a Reynolds number of 100,000 test condition, too much diffusion occurs and the separation bubble on the lower wall is overly large. If too little suction is applied for a Reynolds number of 100,000 test condition, the separation bubble collapses and the upper wall separates. Neither of these conditions are desirable since both cases represent a departure of the lower wall pressure distribution from the desired pressure distribution.

This flow visualization data compares favorably with data from an experiment performed by Morin and Patrick (1991) on a flat plate with a contoured wall modeled from a compressor blade.

D. Pressure Distribution Data

Plots of the pressure distributions measured along the flat test plate are shown in Figures 23 and 24. Off-centerline static pressure tap locations are shown in figure 15 and

listed in Table 3.

Figure 23 is a pressure coefficient plot for a Reynolds number of 100,000 test condition. The pressure coefficient behaves as expected in the upstream (converging) portion of the test section, decreasing to a minimum value at the throat as the flow accelerates. However, downstream of the throat in the diverging portion of the test section, the pressure coefficient increases and then becomes flat for a short distance indicating that the flow has separated from the lower wall. The behavior of the pressure coefficient is consistent for the three turbulence intensities tested for a Reynolds number of 100,000 except for the length of the flat region of the curve. The length of the flat region of the curve decreases as turbulence intensity increases which implies that the length of the separation bubble is inversely proportional to the freestream turbulence intensity. This result is consistent with those of Gaster (1967) and Morin and Patrick (1991) in their studies of separation bubbles.

Figure 24 is a plot of the experimental pressure distribution for a Reynolds number of 250,000 and the three levels of freestream turbulence tested. The pressure distributions for three turbulence levels collapse into a single curve, and it can be deduced from this data that freestream turbulence does not affect the freestream flow for the range of turbulence intensities tested. The pressure distributions for grids 0, 2 and 3 closely resemble a typical turbine blade suction surface pressure distribution with a decrease in pressure coefficient in the diverging region of the channel (favorable pressure gradient region) followed by an attendant increase of pressure in the converging region of the channel (adverse pressure gradient region). The pressure distributions for a Reynolds number of 250,000 compare favorably with the panel code generated pressure

distributions as shown in Figure 25.

A comparison of the pressure distributions for the generic LPT blade, Panel code simulated test section design and experiment is shown in Figure 25. The Reynolds number of 250,000 corresponds to the design point for the generic LPT blade. The pressure distributions compare favorably in the accelerating portion of the flow reflected by the closeness of the pressure coefficient curves as shown in the Figure 25. However, the minimum pressure point differs for each curve and this is primarily due to a slight difference in the ratio of the exit velocity to critical velocity. If the simulated test section and experiment ratios of exit velocity to critical velocity are increased the curves collapse on top of the LPT blade pressure distribution. In the adverse pressure gradient region (converging region of the channel), the difference in the experimental pressure distribution is more pronounced than the blade and test section pressure distributions primarily because of viscous effects and the exit velocity ratio mismatch .

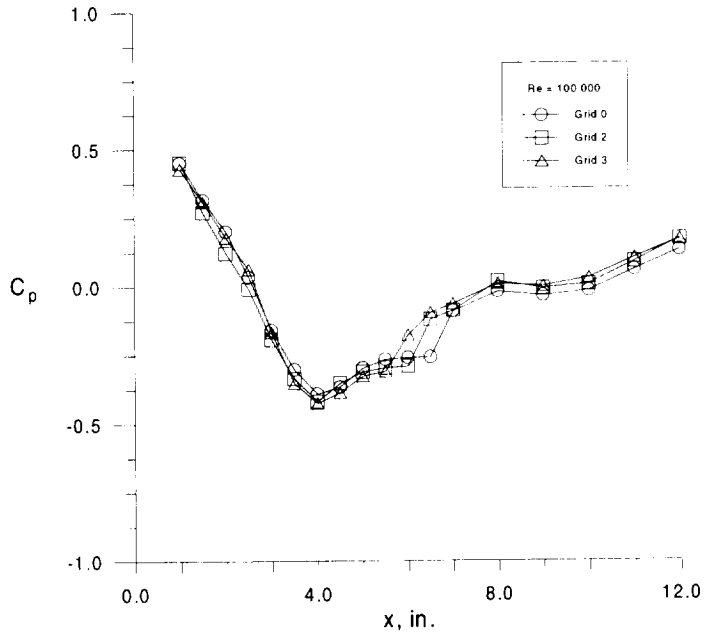

Figure 23 Experimental simulated test section lower wall pressure distributions, grids 0, 2 and 3, Re = 100,000

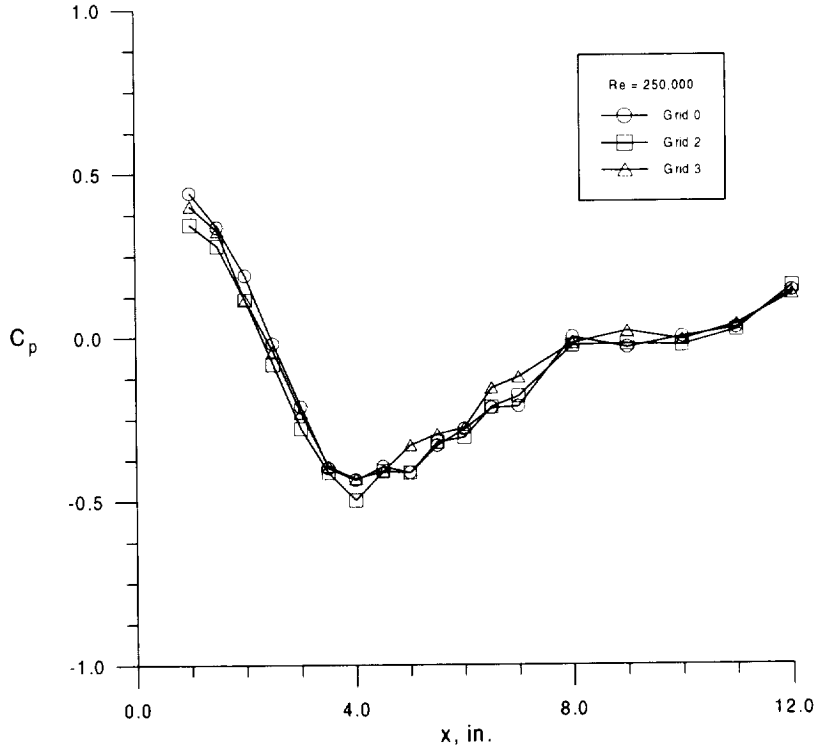

Figure 24 Experimental simulated test section lower wall pressure distributions, grids 0, 2 and 3, Re = 250,000

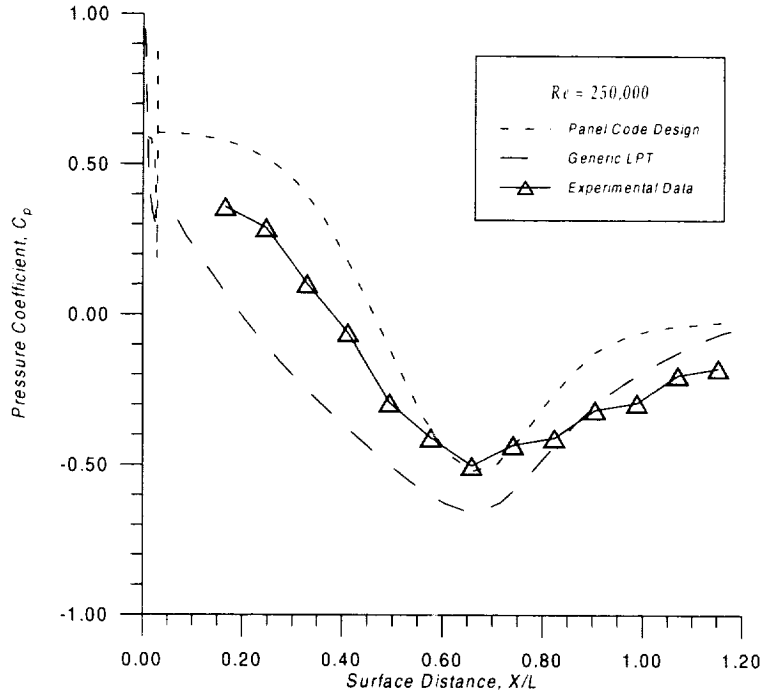

Figure 25 Comparison of computational and experimental lower wall pressure distributions, Re = 250,000

E. Hot-wire Data

Single sensor hot-wire data were obtained for Reynolds numbers of 100,000 and 250,000 operating conditions at free-stream turbulence levels of 0.8% (grid 0), 2% (grid 2) and 3% (grid 3). Table 1 lists the test matrix used for this experiment and the measurements were made at centerline axial locations shown in Table 7 (all distances are in inches and referenced from the leading edge of the flat plate).

1. Mean Velocity Contour Plots

Mean velocity contour plots for Reynolds numbers of 100,000 and 250,000 and for grids 0, 2 and 3 are shown in Figures 26 to 31. The velocity and streamline profiles were computed from reduced velocity profiles obtained from single sensor hot-wire probe digitized data.

Figures 26-28 are contour plots for a Reynolds number of 100,000 and freestream turbulence intensity levels of 0.8% (grid 0), 2% (grid 2) and 3% (grid 3), respectively. The contour plot for grid 0 is shown in Figure 26 and clearly shows a well defined separation bubble indicated by the deflection of the streamlines with the bubble starting at an axial position of approximately 5.25 inches (13.33 cm) and extending to approximately 7.25 inches (18.42 cm). The maximum separation bubble height and length of 0.040 and 2.00 inches (0.102 and 5.08 cm), respectively, occurs at this freestream turbulence level of 0.8%. The contour plot for grid 2 is shown in Figure 27 with the starting position of the bubble remaining the same as for grid 0, but the bubble height and length have decreased. This behavior is repeated in Figure 28 for grid 3 with the starting point of the separation bubble again remaining fixed, but the bubble height and length are further reduced due an increased level of freestream turbulence. It can be deduced from this behavior that the height and length of the separation bubble varies inversely with freestream turbulence intensity and that the separation bubble starts at the same streamwise location for the levels of turbulence intensity tested at this Reynolds number. A summary of the separation bubble characteristics for this Reynolds number condition with corresponding freestream turbulence levels is contained in Table 8.

Figures 29-31 are contour plots for a Reynolds number of 250,000 and they reveal that no separation occurs for the three turbulence levels tested. These contour plots show that for this Reynolds number, the flow in the adverse pressure gradient region is attached. The pressure distributions for this Reynolds number condition are representative of the pressure distributions that would be obtained in a LPT at takeoff conditions.

Table 7, Streamwise Hot-wire Measurement Locations

x, inches (Grid 0)	x, inches (Grid 2)	x, inches (Grid 3)
1.75 (4.45 cm)	1.75 (4.45 cm)	1.75 (4.45 cm)
2.25 (5.72 cm)	2.25 (5.72 cm)	2.25 (5.72 cm)
2.75 (6.99 cm)	2.75 (6.99 cm)	2.75 (6.99 cm)
3.25 (8.26 cm)	3.25 (8.26 cm)	3.25 (8.26 cm)
3.75 (9.53 cm)	3.75 (9.53 cm)	3.75 (9.53 cm)
4.25 (10.80 cm)	4.25 (10.80 cm)	4.25 (10.80 cm)
4.75 (12.07 cm)	4.75 (12.07 cm)	4.75 (12.07 cm)
5.25 (13.34 cm)	5.25 (13.34 cm)	5.25 (13.34 cm)
5.75 (14.61 cm)	5.75 (14.61 cm)	5.75 (14.61 cm)
6.25 (15.88 cm)	6.25 (15.88 cm)	6.25 (15.88 cm)
6.75 (17.15 cm)	6.75 (17.15 cm)	6.75 (17.15 cm)
7.25 (18.42 cm)	7.25 (18.42 cm)	7.25 (18.42 cm)
7.75 (19.69 cm)	7.75 (19.69 cm)	7.75 (19.69 cm)
8.25 (20.96 cm)	8.25 (20.96 cm)	8.25 (20.96 cm)
8.75 (22.23 cm)	8.75 (22.23 cm)*	**
9.25 (23.50 cm)	9.25 (23.50 cm)	9.25 (23.50 cm)

Note :

* No data taken at this streamwise location for Reynolds number = 250,000

** No data taken at this streamwise location for Reynolds number = 100,000 and 250,000

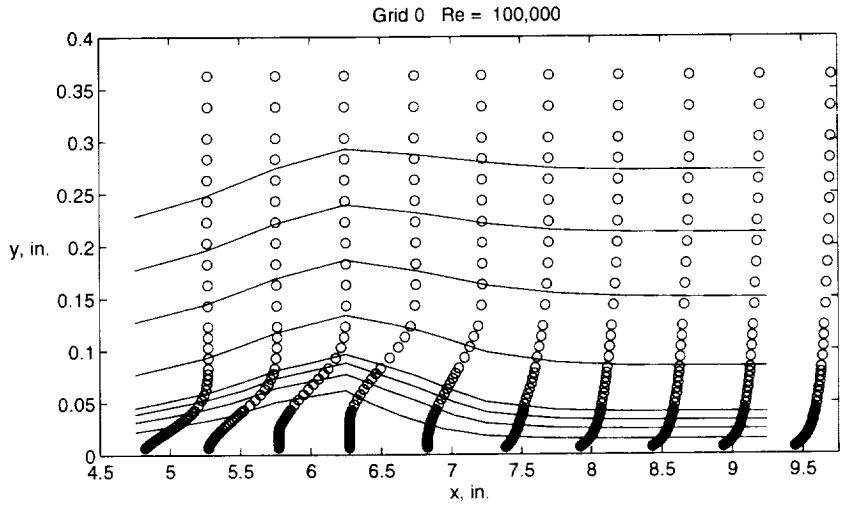

Figure 26 Mean velocity and streamline contour, grid 0, Re = 100,000

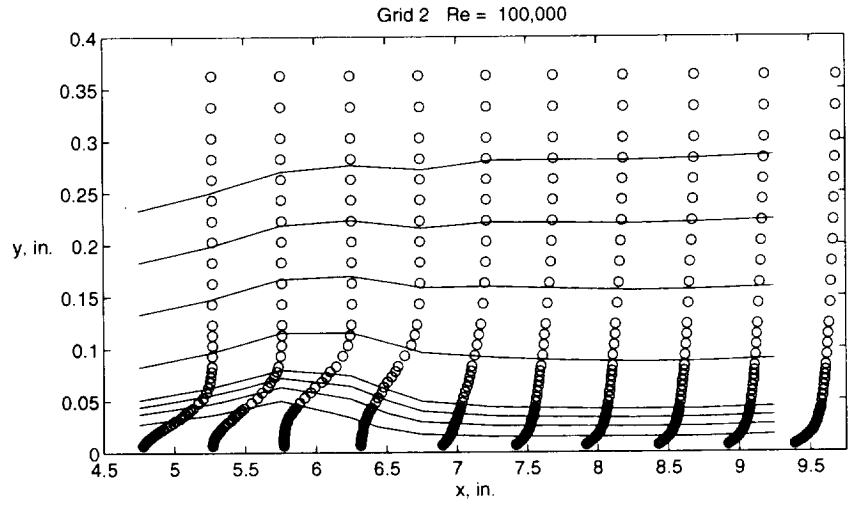

Figure 27 Mean velocity and streamline contour, grid 2, Re = 100,000

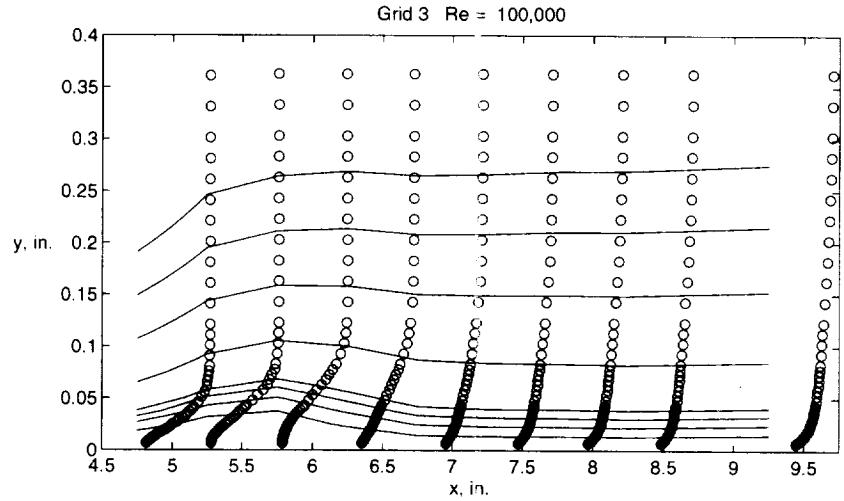

Figure 28 Mean velocity and streamline contour, grid 3, Re = 100,000

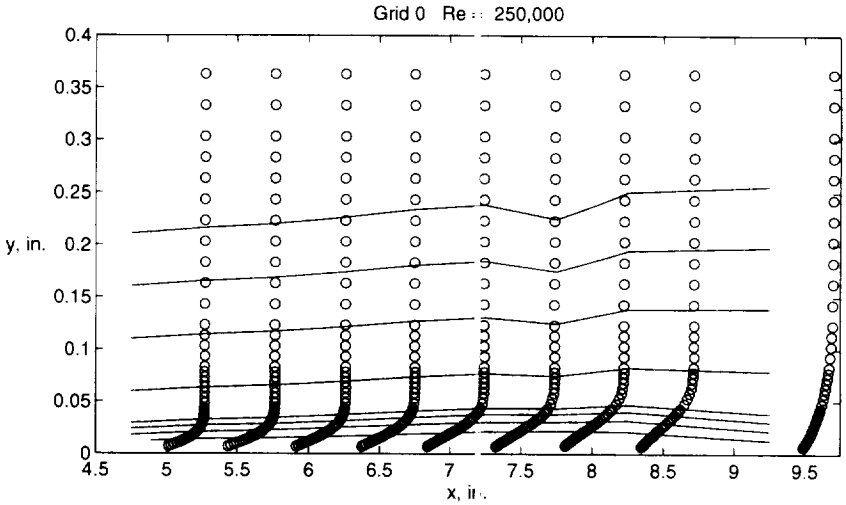

Figure 29 Mean velocity and streamline contour, grid 0, Re = 250,000

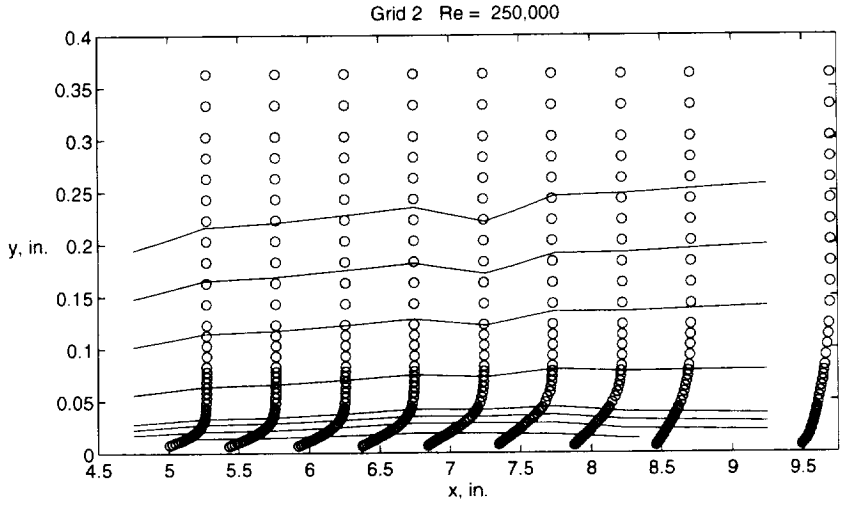

Figure 30 Mean velocity and streamline contour, grid 2, Re = 250,000

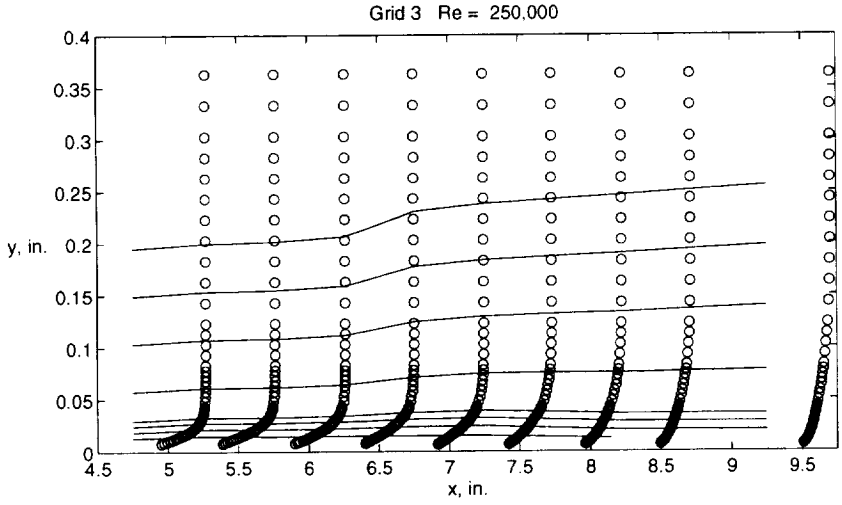

Figure 31 Mean velocity and streamline contour, grid 3, Re = 250,000

2. Law of the Wall Plots

The onset of transition on the lower wall can be clearly visualized by normalizing the mean velocity profiles and plotting these variables using logarithmic and semi-logarithmic scale axes. The wall unit variables u^+ and y^+ are defined by the following relations:

$$u^+ = \frac{u_e}{u_\tau} \text{ and } y^+ = \frac{yu^+}{\nu} .$$

The quantity u_e is the velocity at the edge of the boundary layer, u_τ is the friction velocity and is defined as the square root of the wall shear stress divided by the local density, i.e., $\sqrt{\frac{\tau_w}{\rho}}$, y is the vertical distance from the test surface and ν is the kinematic viscosity. A curve fit technique developed by Clauser (1956) was used to plot the mean velocity profiles in the above coordinates and further details of this technique can be found in this reference, as well as in Suder et al. (1988) and Sohn and Reshotko (1991). This technique involves iterating on a skin friction coefficient value for the measured mean velocity profile and plotting the best fit value of the skin friction coefficient on the u^+ versus y^+ curve.

The mean velocity plots of these variables are shown in Figures 32-37 for the upstream measurements at Reynolds numbers of 100,000 and 250,000 and for downstream measurements at a Reynolds number of 250,000. Downstream mean velocity profiles for a Reynolds number of 100,000 could not be constructed because the skin friction coefficient is zero for separated flow. Additionally, for comparative purposes, reference curves for u^+ versus y^+, Blasius' laminar boundary layer solution and Musker's (1979) continuous law-of-the-wall turbulent boundary layer solution are also plotted. Figures 32-34 are plots of the upstream mean velocity profiles for a

Reynolds number of 100,000 and for grids 0, 2 and 3. These plots show excellent agreement with the $u^+ = y^+$ curve for all of the upstream axial stations plotted except at x=4.25 inches (10.80 cm). This deviation from the $u^+ = y^+$ curve at x=4.25 inches (10.80 cm) is present for each freestream turbulence level, but grid 0 has the largest discrepancy from the $u^+ = y^+$ curve. The deviation at x=4.25 inches (10.80 cm) may be attributed to the impending flow separation at x=5.25 (13.34 cm) inches for a Reynolds number of 100,000. For each grid, the u^+ value increases or, alternatively, the skin friction coefficient decreases as the flow progresses downstream from x=1.75 (4.45 cm) to 4.25 inches (10.80 cm). The upstream mean velocity profiles for a Reynolds number of 250,000 are presented in Figures 35-37 and show excellent agreement with the $u^+ = y^+$ curve for all axial locations including x=4.25 inches (10.80 cm). These profiles follow the same trend that the upstream profiles for a Reynolds number of 100,000 exhibit with the u^+ value increasing as the flow progresses downstream from x=1.75 (4.45 cm) to 4.25 inches (10.80 cm).

The downstream mean velocity profiles for a Reynolds number of 250,000 are shown in Figures 38-40 for grids 0, 2 and 3, respectively. Excellent agreement is obtained with the $u^+ = y^+$ curve for each axial location as with the Reynolds number of 100,000 profiles. Again, these profiles exhibit a similar behavior to the Reynolds number of 100,000 profiles with the u^+ value increasing as the flow progresses downstream until the onset of transition occurs. The u^+ value then decreases or alternatively the skin friction coefficient increases after the onset of transition. The skin friction coefficient continues to increase until the flow becomes fully turbulent. As the

flow approaches a fully turbulent profile, the mean velocity profiles approach the Musker curve on the plot as this curve represents fully turbulent flow. Fully turbulent flow does not occur for any of the axial measurement stations for grid 0 as shown in Figure 38, but fully turbulent flow is achieved for grids 2 and 3 as shown in Figures 39 and 40. Onset of transition can also be deduced from these plots and for grid 0 transition onset starts to occur at approximately x=7.75 inches (19.68 cm). Additionally, transition onset starts to occur for grid 2 at approximately x=6.75 inches (17.15 cm) and at approximately x=5.75 inches (14.61 cm) for grid 3. Approximate transition onset locations determined from intermittency profiles will be presented in a later section. These law of the wall plots show similar trends with those presented by Simon and Qiu (1996).

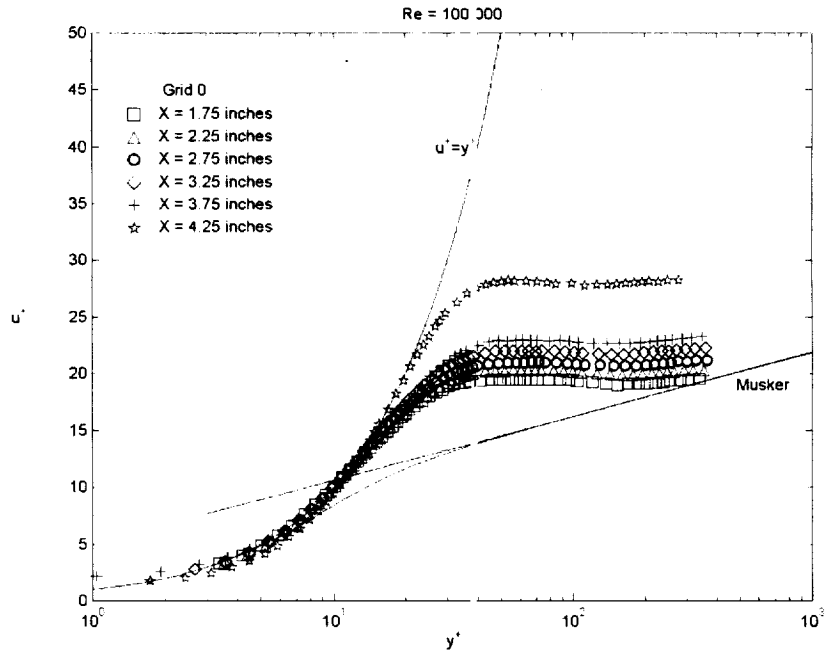

Figure 32 Upstream mean velocity profiles in wall units, grid 0, Re = 100,000

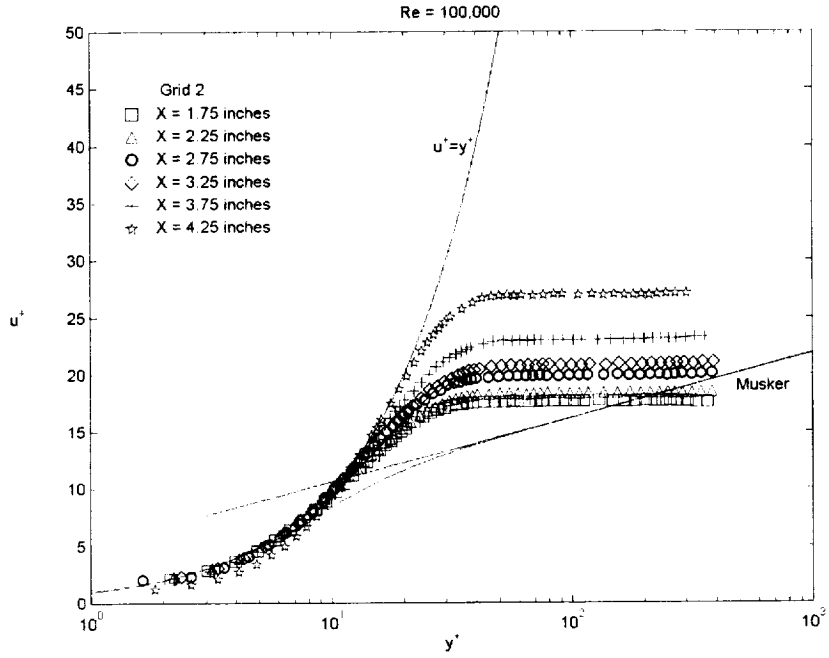

Figure 33 Upstream mean velocity profiles in wall units, grid 2, Re = 100,000

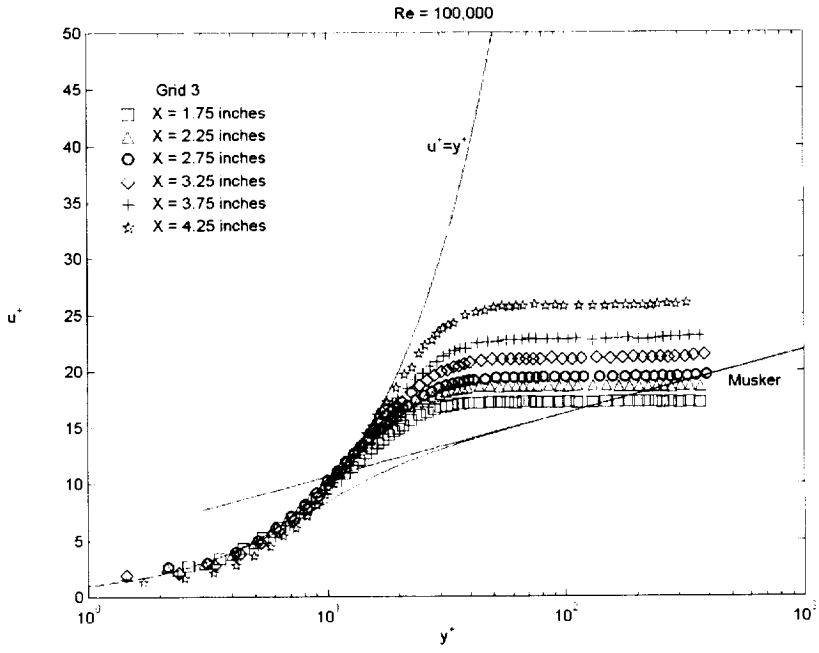

Figure 34 Upstream mean velocity profiles in wall units, grid 3, Re = 100,000

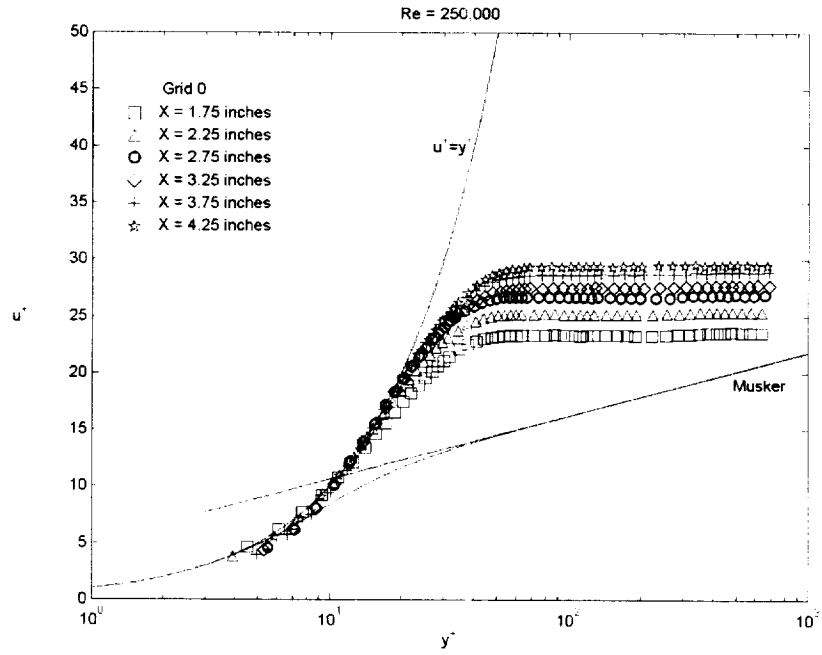

Figure 35 Upstream mean velocity profiles in wall units, Re = 250,000

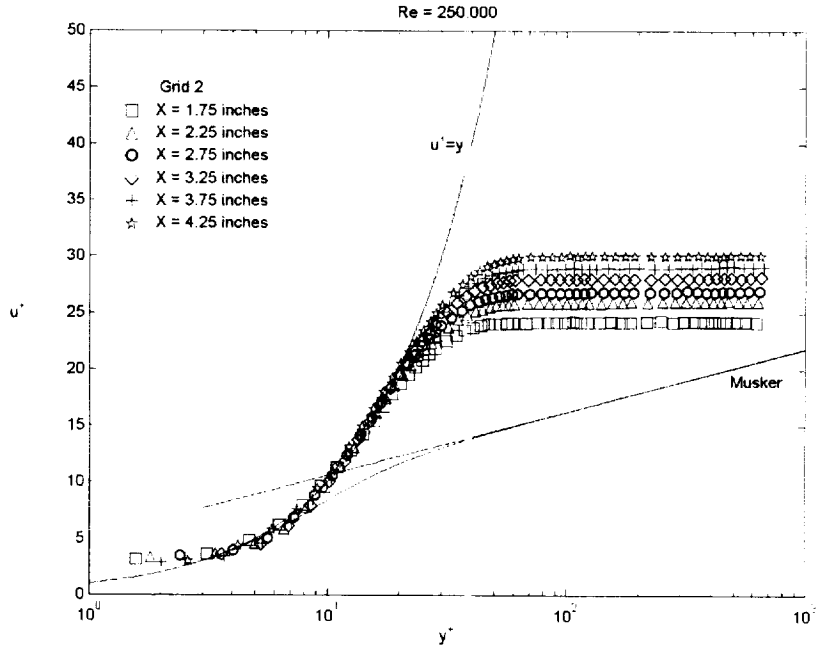

Figure 36 Upstream mean velocity profiles in wall units, grid 2, Re = 250,000

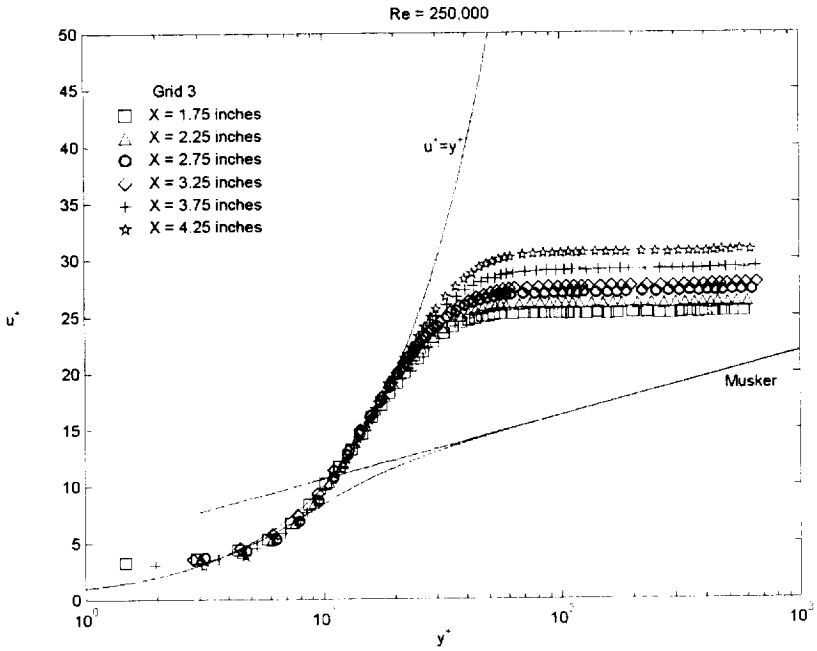

Figure 37 Upstream mean velocity profiles in wall units, grid 3, Re = 250,000

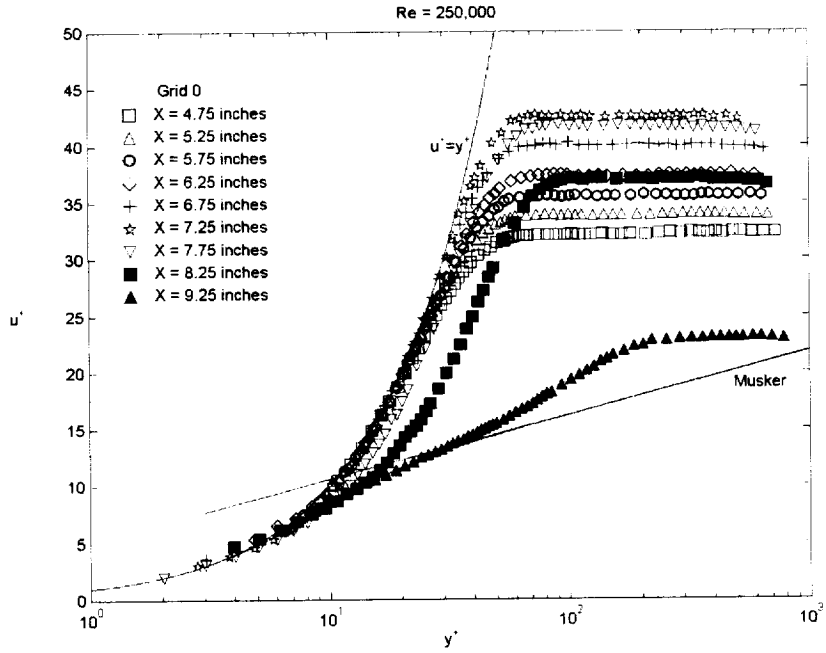

Figure 38 Downstream mean velocity profiles in wall units, grid 0, Re = 250,000

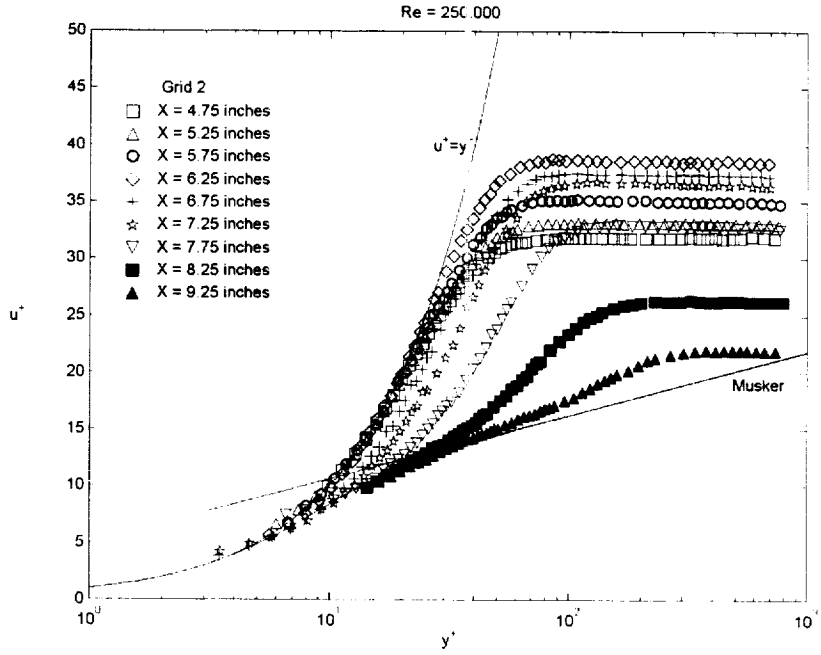

Figure 39 Downstream mean velocity profiles in wall units, grid 2, Re = 250,000

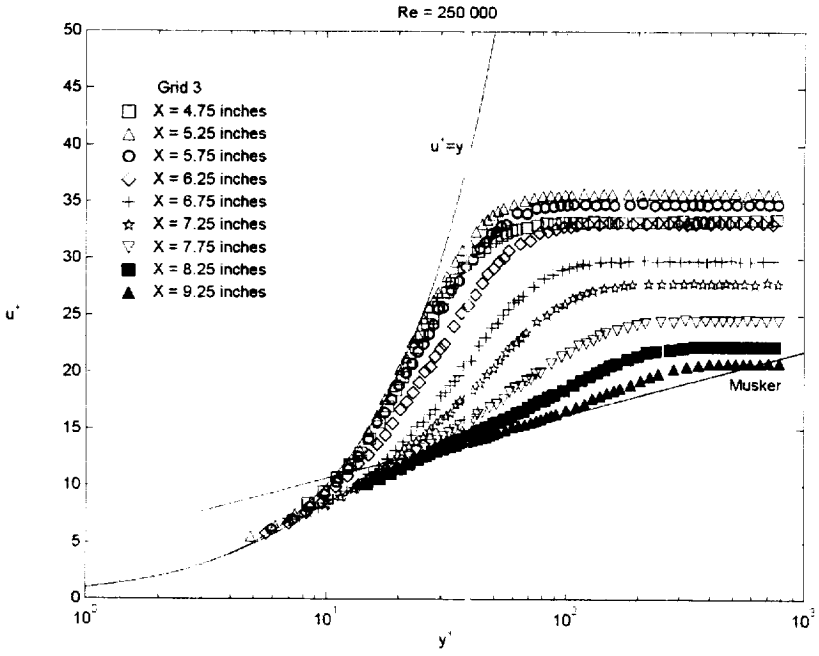

Figure 40 Downstream mean velocity profiles in wall units, grid 3, Re = 250,000

3. Fluctuating (rms) Velocity Profiles

Fluctuating (rms) velocity profiles are shown in Figures 41-46 for grids 0, 2 and 3 along with the same streamline patterns plotted for the mean velocity profiles in Figures 26-31. Figures 47-58 show the upstream and downstream rms profiles in outer coordinates. The upstream rms velocity profiles shown in Figures 47-52 are consistent in behavior in that the rms velocity levels increases as the free-stream trubulence increases. In the laminar boundary layer at a low freestream turbulence level (grid 0, Figure 53) and a Reynolds number of 100,000, the rms velocity profile is nearly flat with small magnitudes for the entire flow field except for a small hump near the wall. This small peak grows in magnitude and moves away from the wall to the shear layer as the flow proceeds downstream from the separation location. This peak in the shear layer grows rapidly after the maximum bubble height location and triggers a slowdown of bubble growth due to turbulent energy dispersion. Additionally, the small peak can be seen inside the bubble at x=6.25 inches (15.88 cm). Due to the limited number of measurement stations within the separation bubble and the inability of the hot-wire to correctly measure velocity profiles in the reverse flow region, the peak that developed inside the bubble could not be studied. However, in the LDV experiment on the diverging channel flow performed by Morin and Patrick (1991), it was observed that the second peak which developed inside the bubble substantially outgrew the first peak and they merged together further downstream. They also found that a third peak developed around the edge of the boundary layer. For higher freestream turbulence levels (grids 2 and 3), the peak is much larger than that for grid 0 at the first measurement station because the laminar boundary layer is buffeted by higher freestream turbulence. Note that

the fluctuating velocity profiles measured at the last measurement station (x=9.25 inches, 23.50 cm) are different from that of the equilibrium turbulent boundary layer suggested by Klebanoff (1955) for each condition, which indicates that even though an attached turbulent boundary layer profile was measured at x=9.25 inches (23.50 cm), the nature of the boundary layer is different due to the separation bubble that occurs upstream.

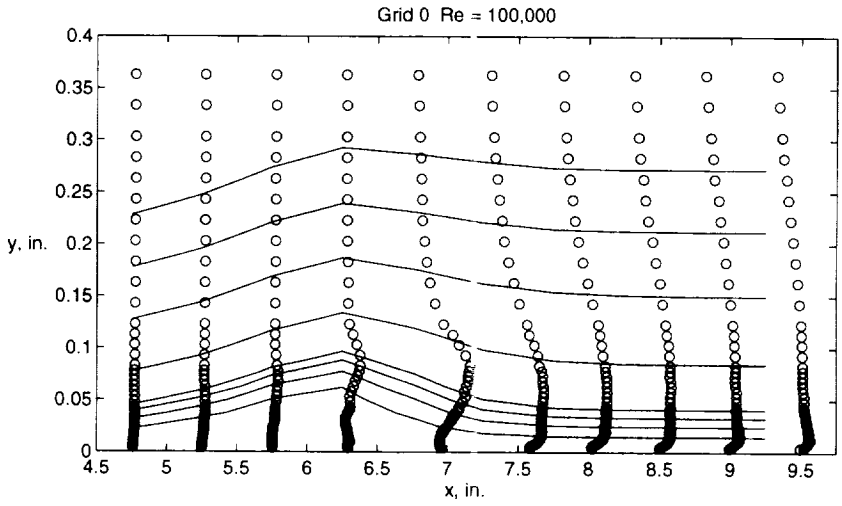

Figure 41 Downstream rms velocity and streamline profiles, grid 0, Re = 100,000

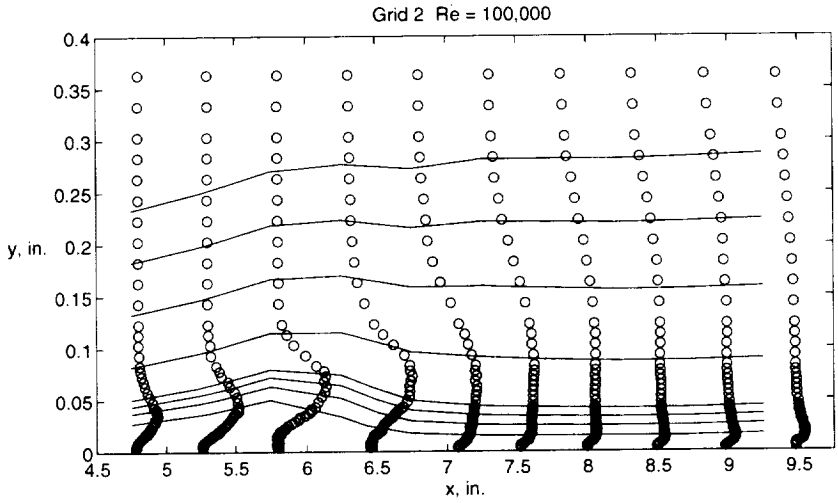

Figure 42 Downstream rms velocity and streamline profiles, grid 2, Re = 100,000

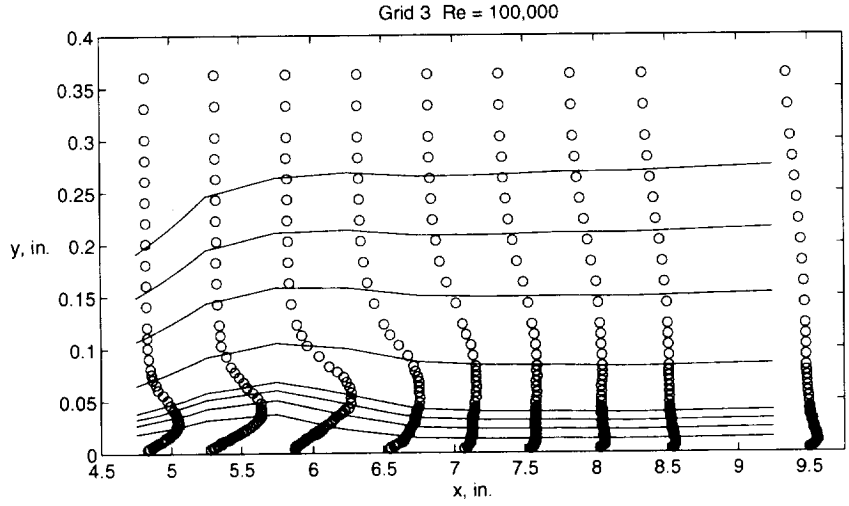

Figure 43 Downstream rms velocity and streamline profiles, grid 3, Re = 100,000

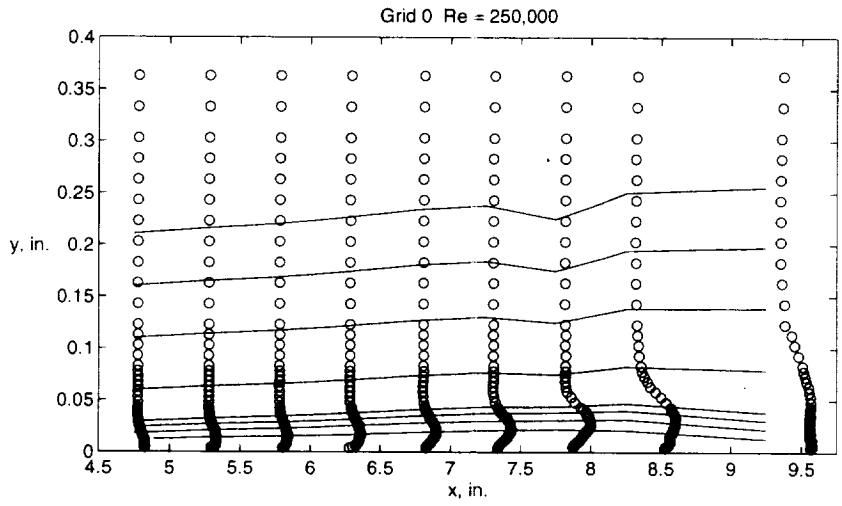

Figure 44 Downstream rms velocity and streamline profiles, grid 0, Re = 250,000

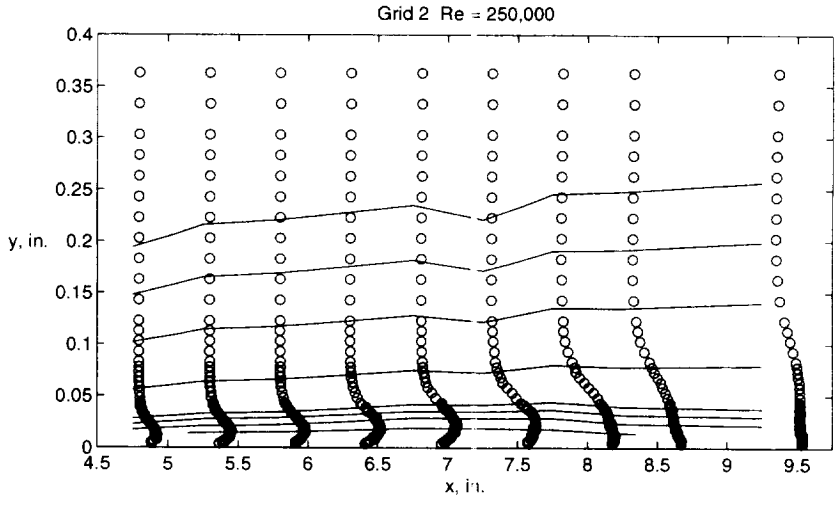

Figure 45 Downstream rms velocity and streamline profiles, grid 2, Re = 250,000

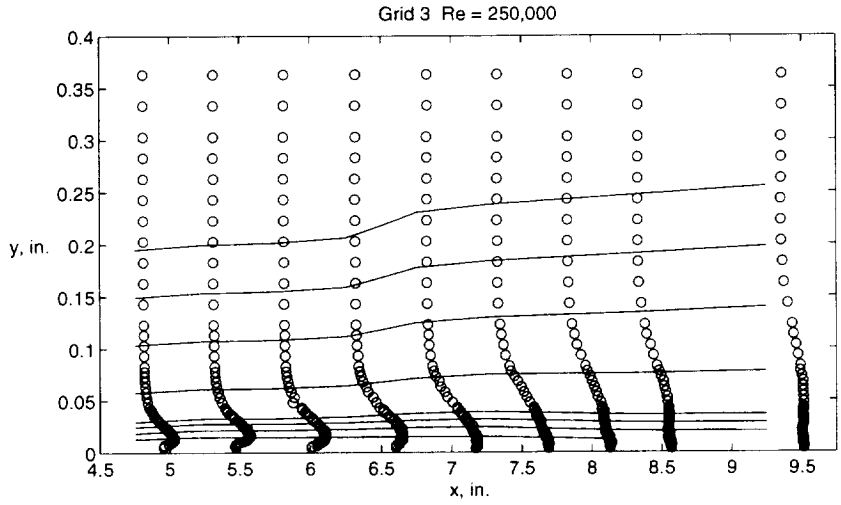

Figure 46 Downstream rms velocity and streamline profiles, grid 3, Re = 250,000

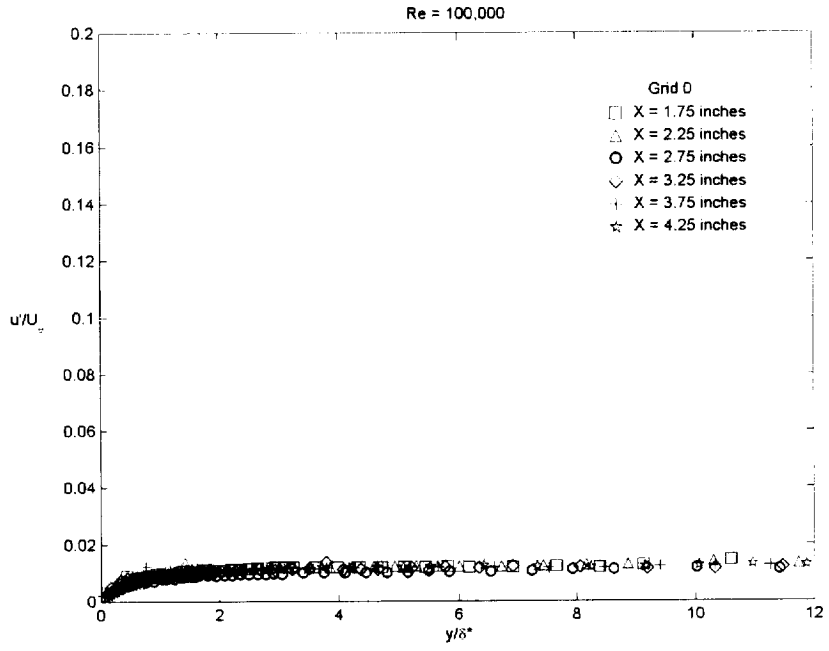

Figure 47 Upstream rms velocity profiles, grid 0, Re = 100,000

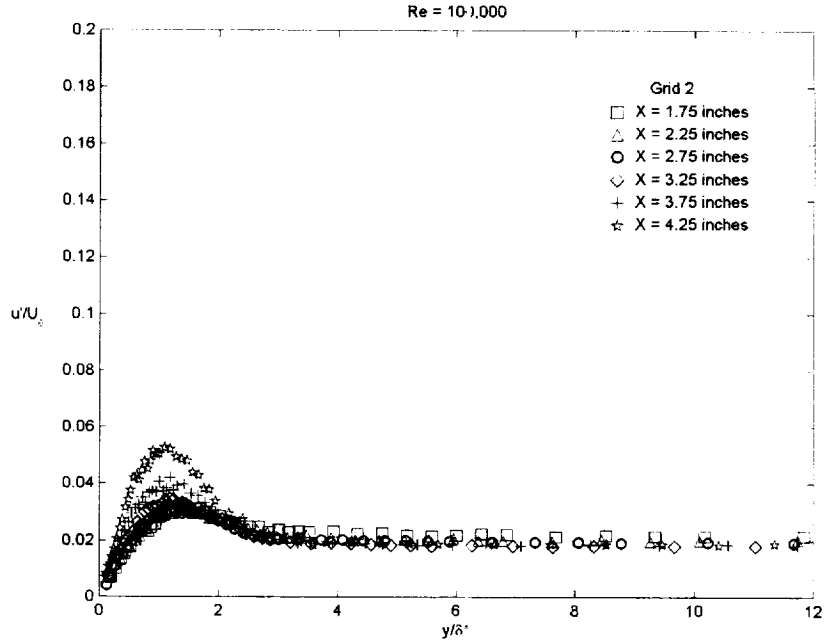

Figure 48 Upstream rms velocity profiles, grid 2, Re = 100,000

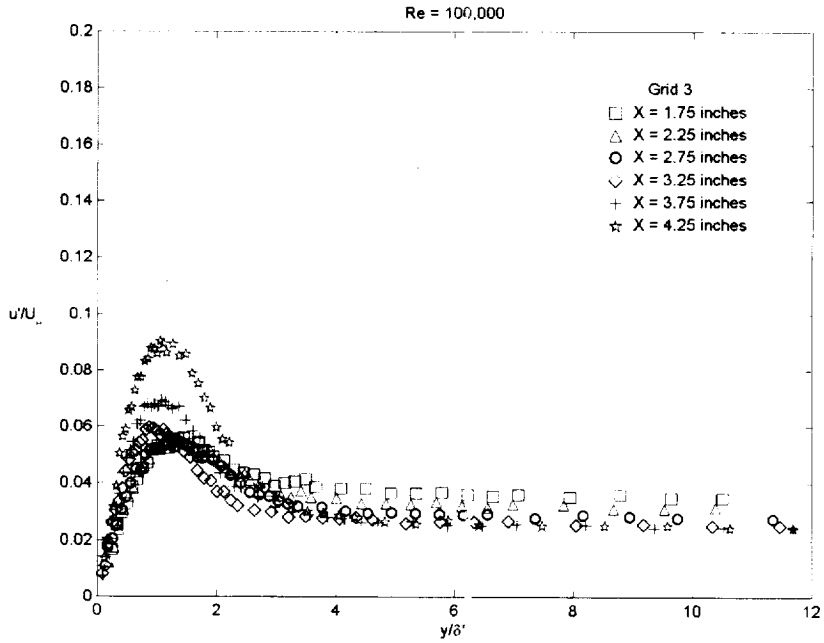

Figure 49 Upstream rms velocity profiles, grid 3, Re = 100,000

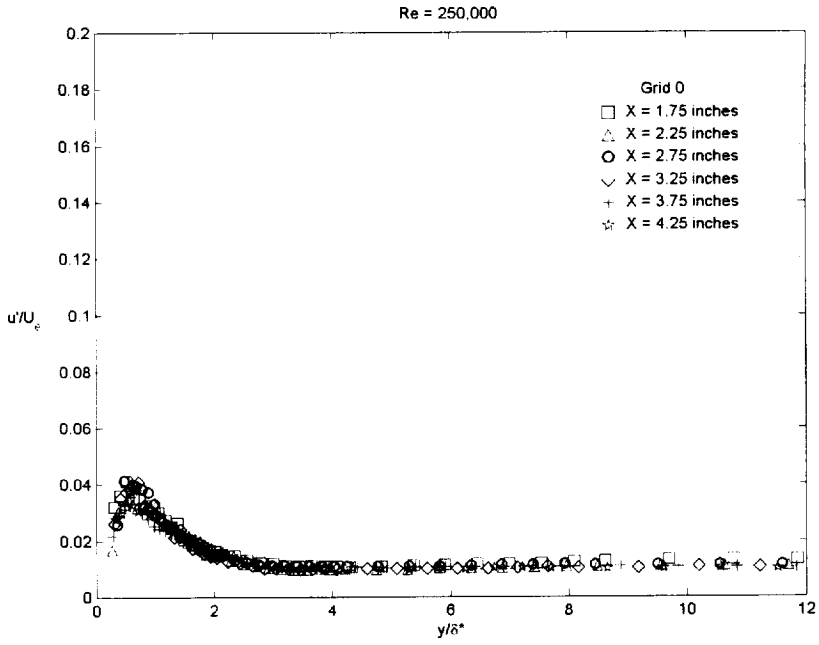

Figure 50 Upstream rms velocity profiles, grid 0, Re = 250,000

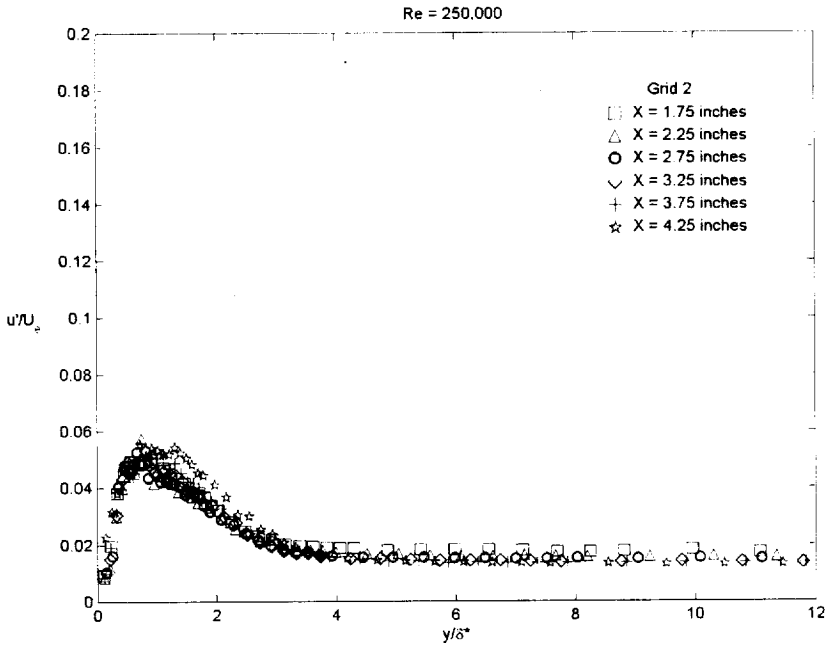

Figure 51 Upstream rms velocity profiles, grid 2, Re = 250,000

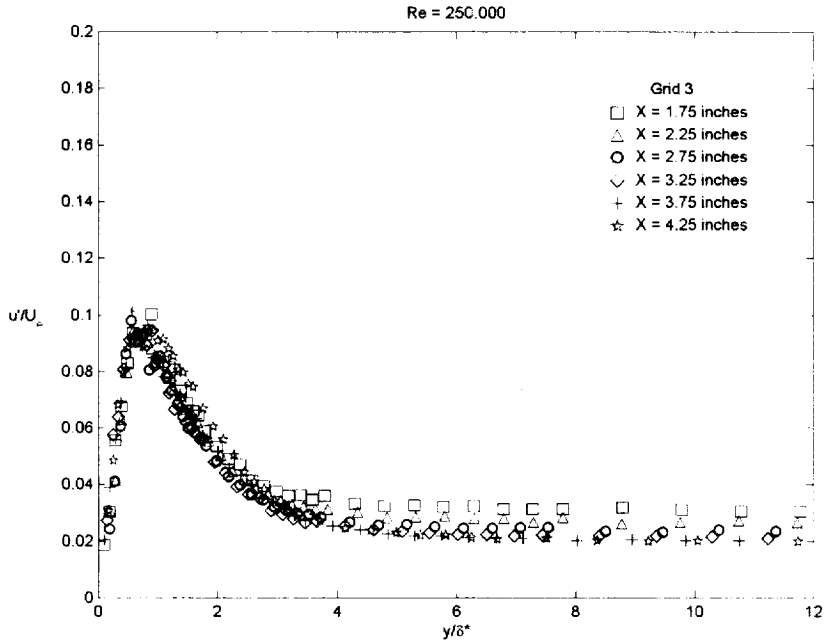

Figure 52 Upstream rms velocity profiles, grid 3, Re = 250,000

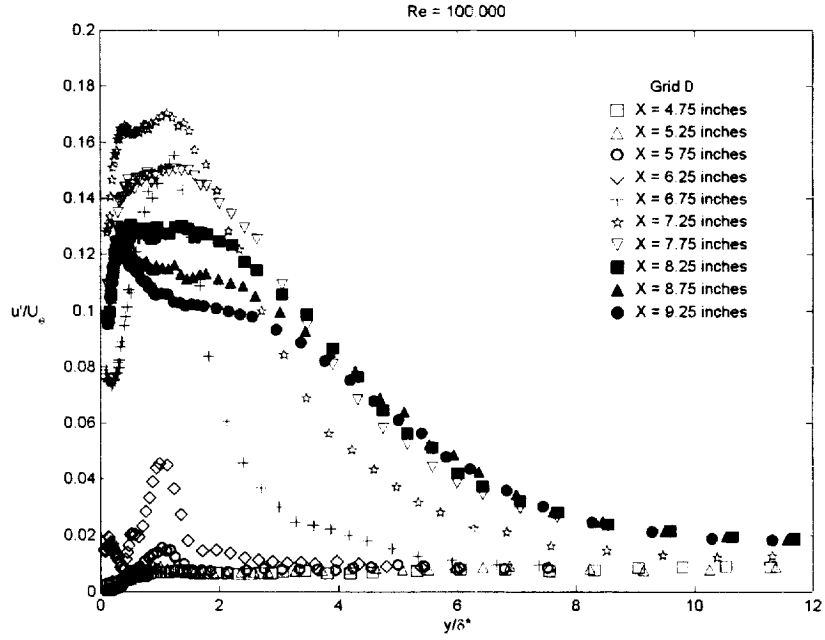

Figure 53 Downstream rms velocity profiles, grid 0, Re = 100,000

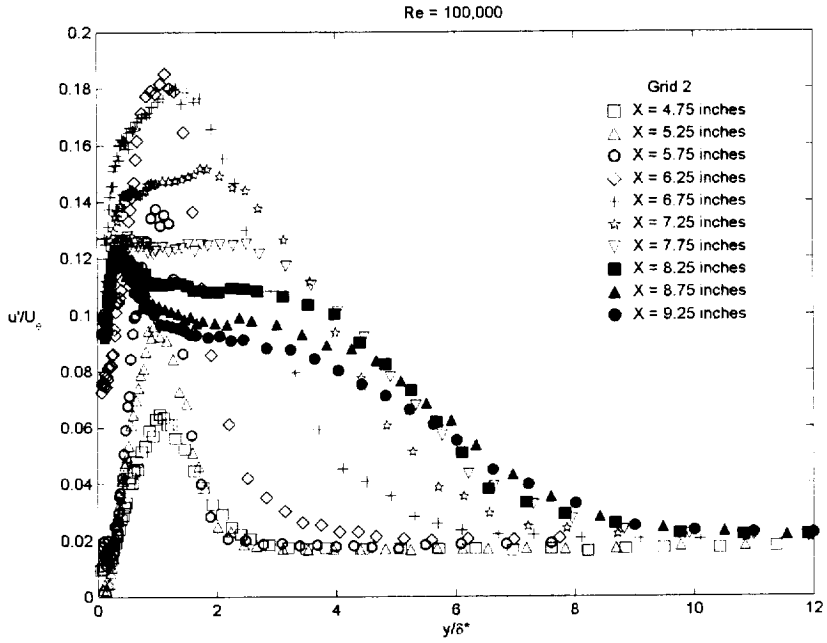

Figure 54 Downstream rms velocity profiles, grid 2, Re = 100,000

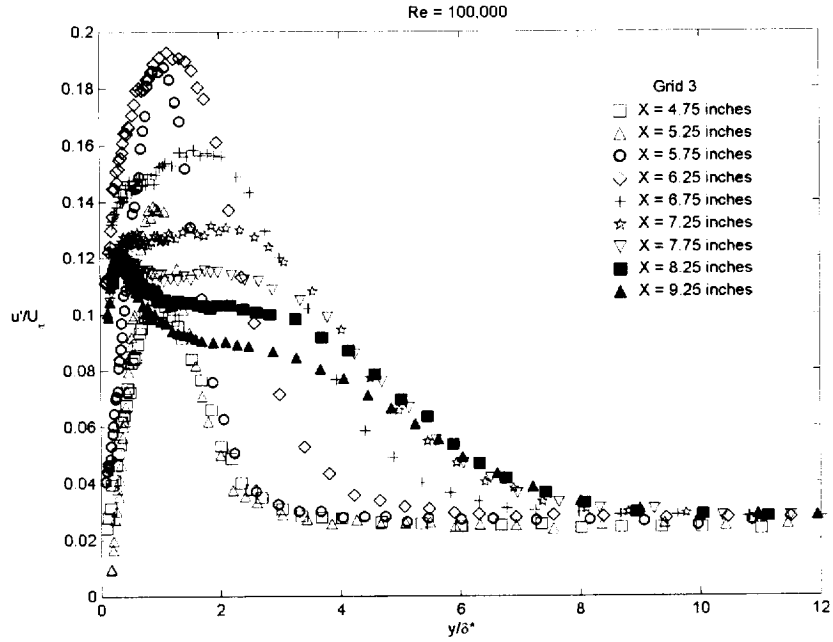

Figure 55 Downstream rms velocity profiles, grid 3, Re = 100,000

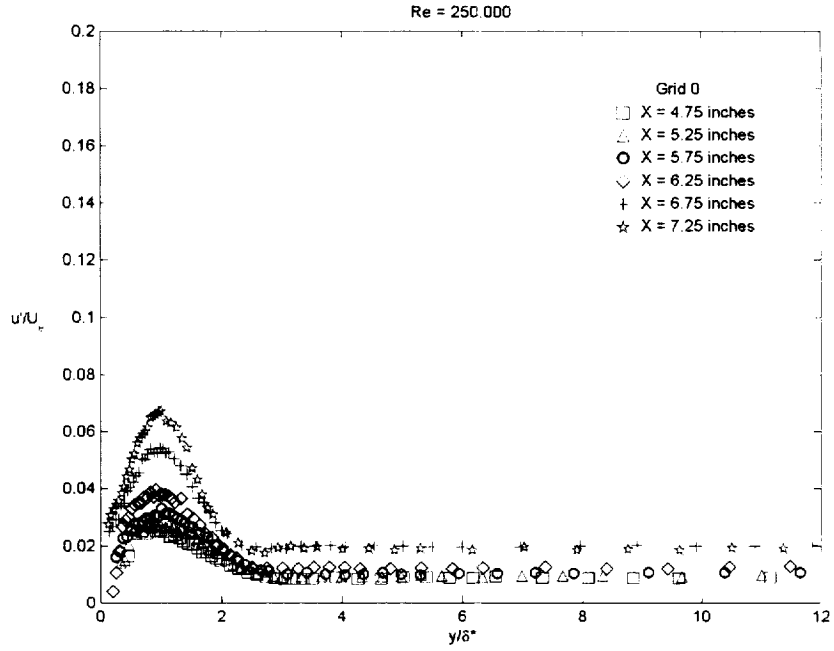

Figure 56 Downstream rms velocity profiles, grid 0, Re = 250,000

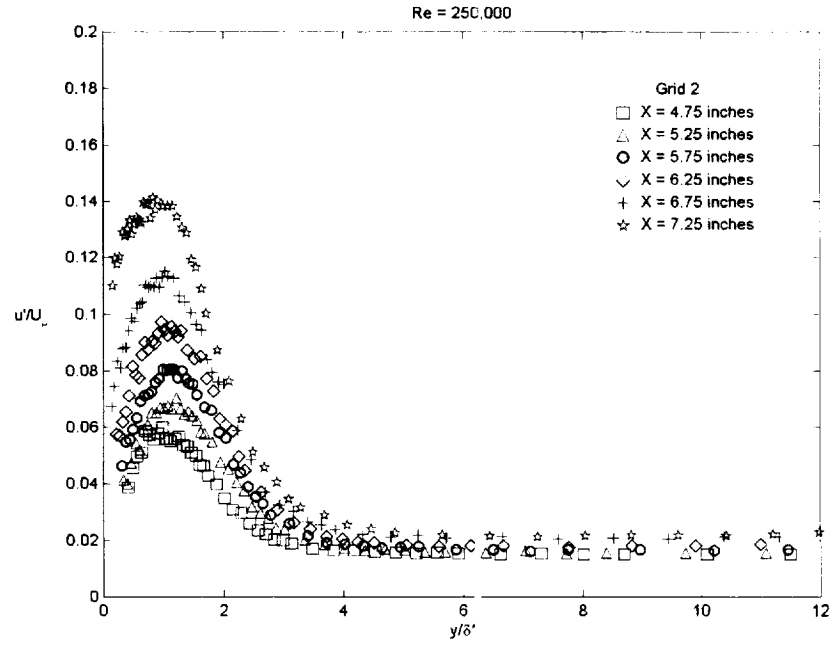

Figure 57 Downstream rms velocity profiles, grid 2, Re = 250,000

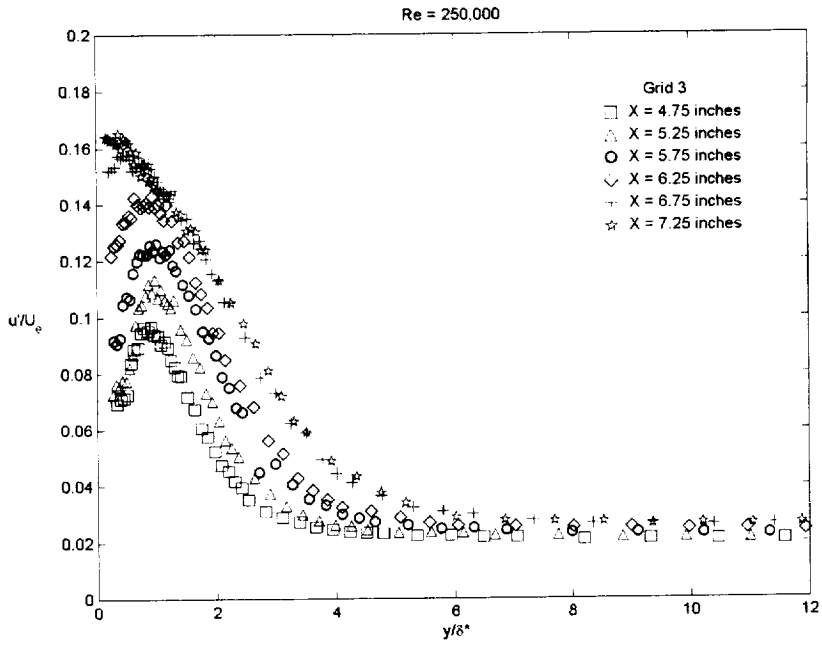

Figure 58 Downstream rms velocity profiles, grid 3, Re = 250,000

4. Boundary Layer Parameters

Plots of the variation of displacement (δ^*), momentum (θ) and energy (ε) thicknesses determined from integrating the mean velocity profiles along the test surface for grids 0, 2 and 3 are presented in Figures 59-68. Additionally, a skin friction coefficient plot is presented in Figure 69 for a Reynolds number of 250,000 only, since the skin friction coefficient is zero for separated flow (Reynolds number of 100,000). Boundary layer parameters were also computed from a code developed by Crawford and Keys (1987) to assist in the reducing of the pre-separation and pre-transition experimental data.

For a Reynolds number of 100,000 and all three turbulence intensities, the displacement thickness increases rapidly to a local maximum near transition and decreases to a local minimum downstream from the reattachment point and then slightly

increases again as shown in Figure 59. The maximum and minimum values of δ^* are inversely proportional to the freestream turbulence level. The momentum and energy thicknesses increase monotonically throughout the test section. The growth rates of both θ and ε, Figures 60 and 61, are the greatest and similar to each other in the separated flow region with both θ and ε increasing as the freestream turbulence level increases up to transition. There is, however, no clear trend downstream from the point of reattachment. The characteristics of the bubble are generally described by the properties at separation. At separation the displacement thickness changes rather rapidly, but the momentum thickness varies slowly due to negligible skin friction. Thus θ is a much more suitable choice than δ^* to describe bubble behavior (Gaster, 1969; O'Meara and Mueller, 1986). The variation of shape factors, H_{12} ($= \delta^*/\theta$) and H_{32} ($= \varepsilon/\theta$), for each condition are presented in Figures 62 and 63. For each condition, H_{12} monotonically increases to a local maximum around transition and sharply decreases to a local minimum downstream from reattachment and then levels out to the values of a turbulent boundary layer. The peak values move upstream with increasing freestream turbulence and this trend is very similar to that observed in the δ^* variation. Opposite trends are observed in the variation of H_{32} for each condition. The most commonly used parameter for determining the separation location is the shape factor H_{12}; however, as noted in the Figure 62, H_{12} varies rapidly at separation due to the large gradient of δ^* and scatters in the upstream region up to transition for different levels of freestream turbulence. On the other hand, H_{32} changes quite slowly throughout the separated flow and is nearly identical up to separation regardless of freestream turbulence levels, so H_{32} is a more logical choice for determining the separation location. The separation locations are determined in this study where H_{32}

is equal to 1.522 for each condition. The separation bubble characteristics for all three grids are summarized for a Reynolds number of 100,000 and are listed in Table 8.

Reattachment models based on shape factors H_{12} and H_{32} have proven to be useful in previous separation bubble calculations. Horton (1968) suggested a universal velocity profile at reattachment with values of H_{12} and H_{32} of 3.50 and 1.51, respectively. The reattachment locations in this study were determined to be where H_{32} is equal to 1.51 for each condition. The separation and reattachment locations determined from the shape factors agree quite well with those obtained from the pressure distribution data.

The variation of the skin friction coefficient, C_f for a Reynolds number of 250,000 is shown Figure 69. C_f is defined below for laminar and turbulent flows as found in Schlichting (1959):

$$C_f = \frac{0.664}{\sqrt{Re_{lam}}} \text{ and } C_f = 0.026\ Re_{tur}^{-1/7}.$$

The skin friction coefficient behaves as expected for an attached laminar boundary layer, decreasing in magnitude as the flow passes from the favorable pressure gradient region into the adverse pressure gradient region. The skin friction coefficient decreases to a minimum value just before the onset of transition and then begins to increase as transition onset occurs. It continues to steadily increase until it reaches a fully turbulent value before finally leveling off to a nearly constant value. This behavior is also consistent for grids 2 and 3, but for grid 0 the skin friction coefficient does not reach the fully turbulent value. These trends are consistent with those obtained from the mean velocity profiles obtained from the Clauser fit technique which also show that for a Reynolds number of 250,000 and grid 0, the last measurement station (x=9.25 inches, 23.50 cm) is not fully

turbulent. Additionally, the trends observed in the skin friction coefficient are similar to those presented by Mayle (1991). The boundary layer properties for each axial measuring station are summarized in Tables 9-14 for grids 0, 2 and 3 and Reynolds numbers of 100,000 and 250,000, respectively.

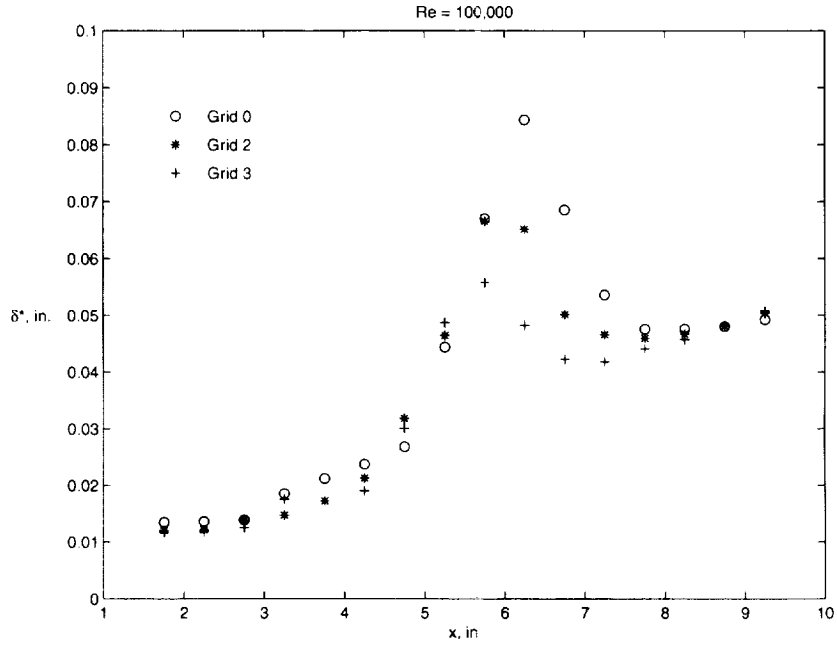

Figure 59 Displacement thickness profiles, grids 0, 2 and 3, Re = 100,000

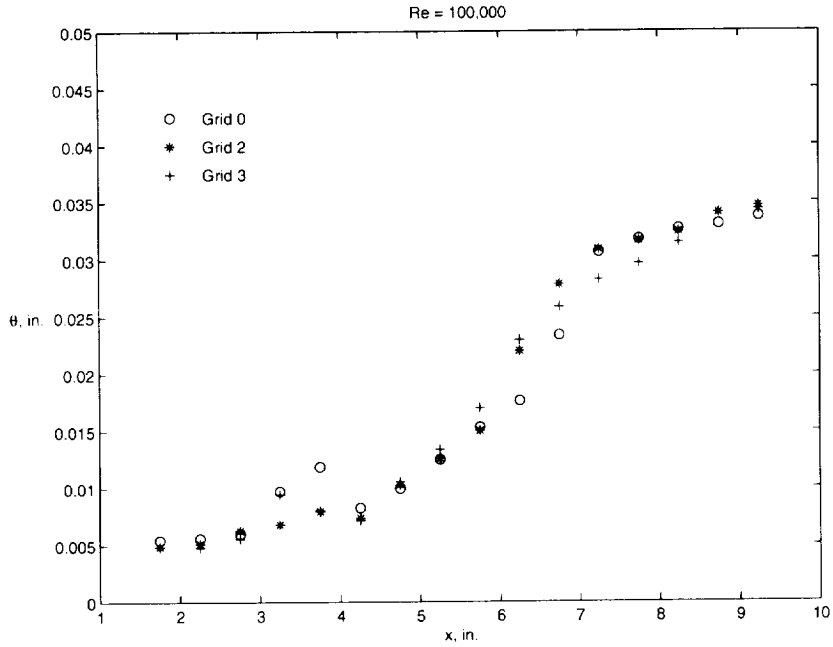

Figure 60 Momentum thickness profiles, grids 0, 2 and 3, Re = 100,000

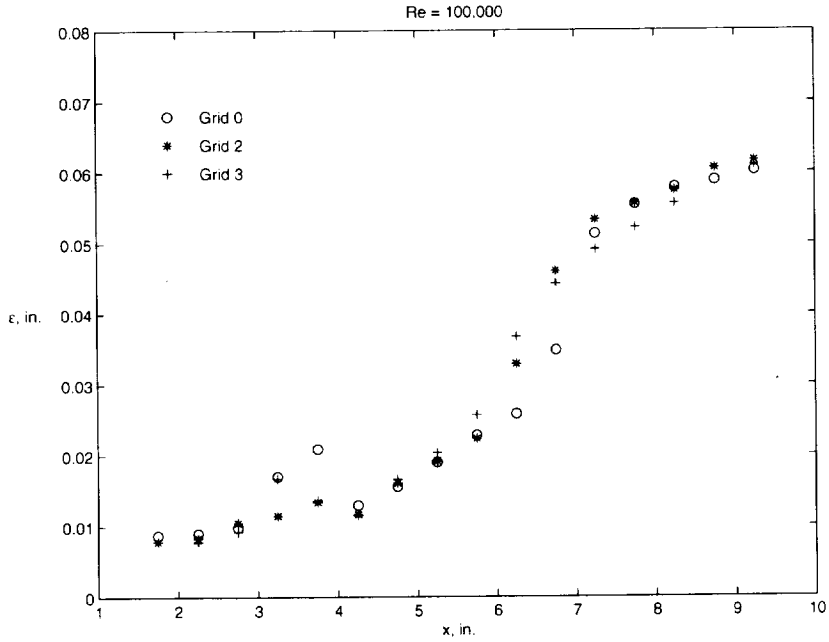

Figure 61 Energy thickness profiles, grids 0, 2 and 3, Re = 100,000

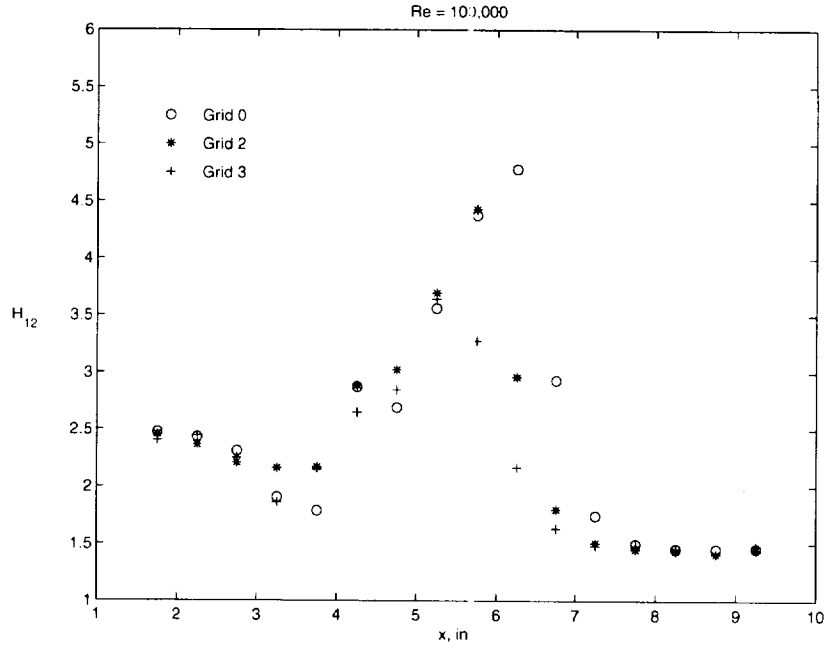

Figure 62 Shape factor profiles, grids 0, 2 and 3, Re = 100,000

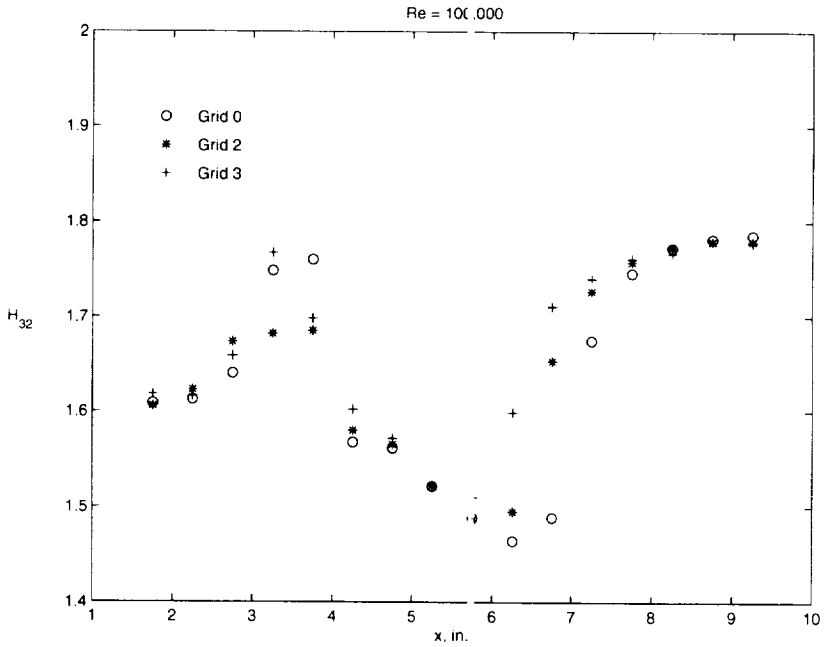

Figure 63 Energy shape factor profiles. grids 0, 2 and 3, Re = 100,000

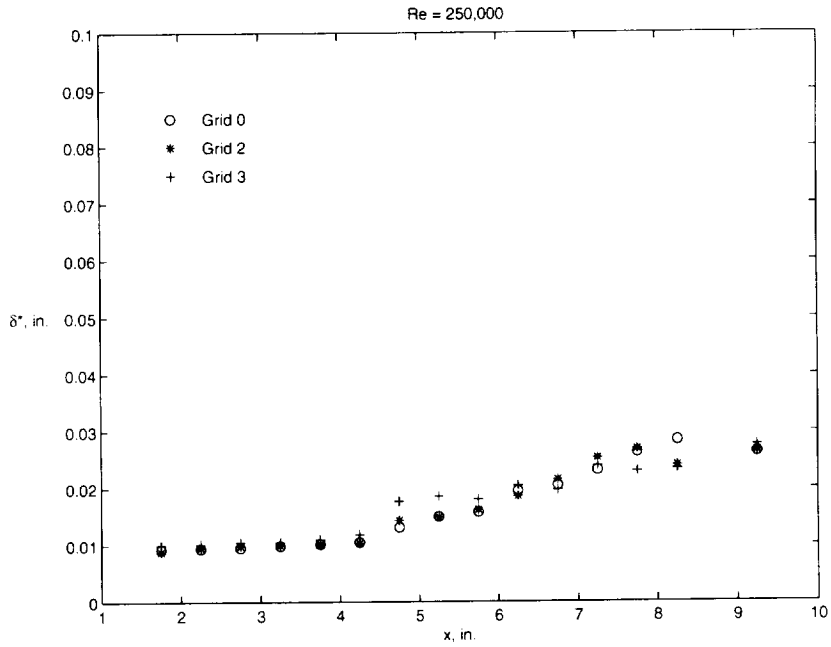

Figure 64 Displacement thickness profiles, grids 0, 2 and 3, Re = 250,000

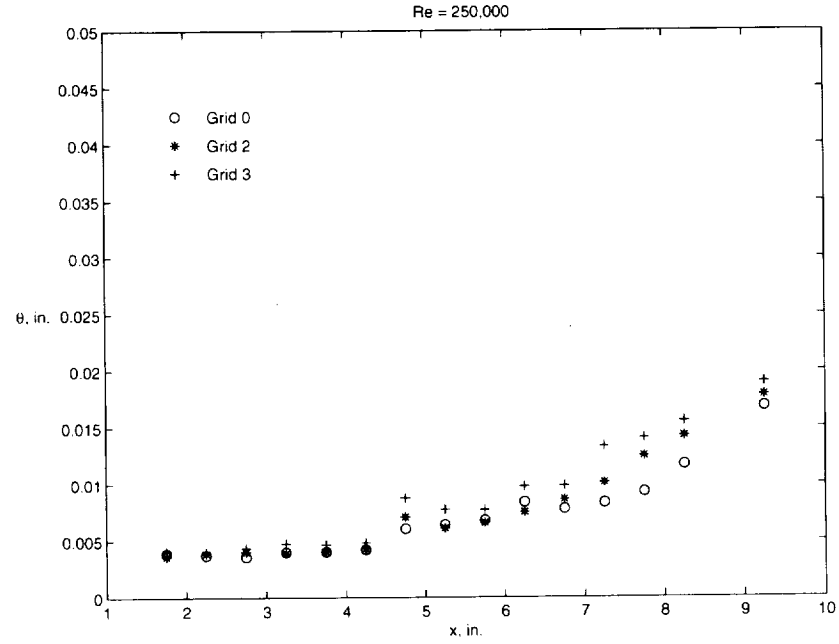

Figure 65 Momentum thickness profiles, grids 0, 2 and 3, Re = 250,000

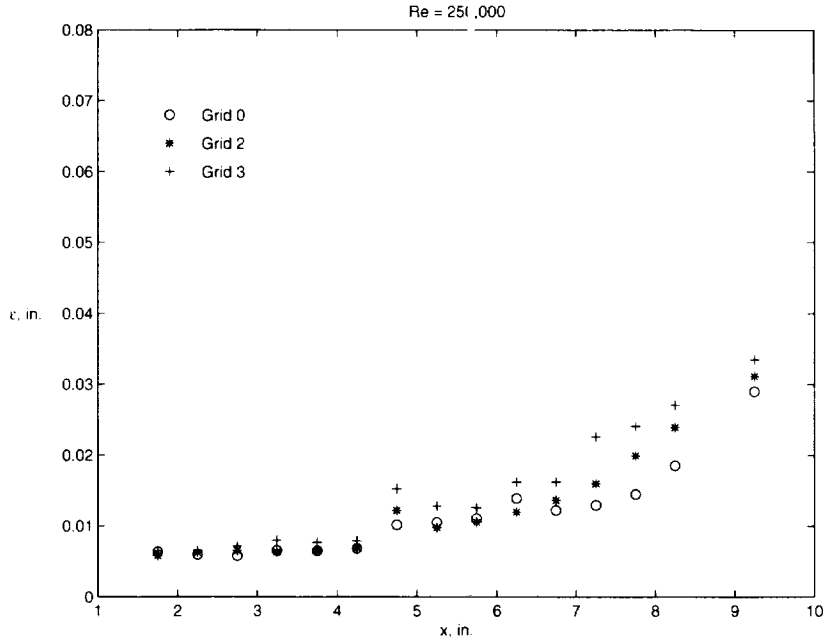

Figure 66 Energy thickness profiles, grids 0, 2 and 3, Re = 250,000

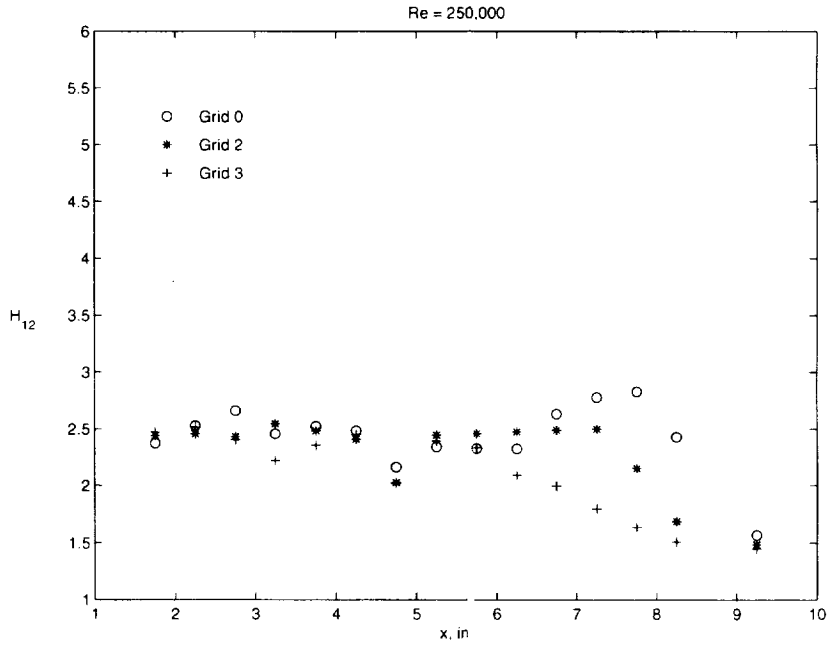

Figure 67 Shape factor profiles, grids 0, 2 and 3, Re = 250,000

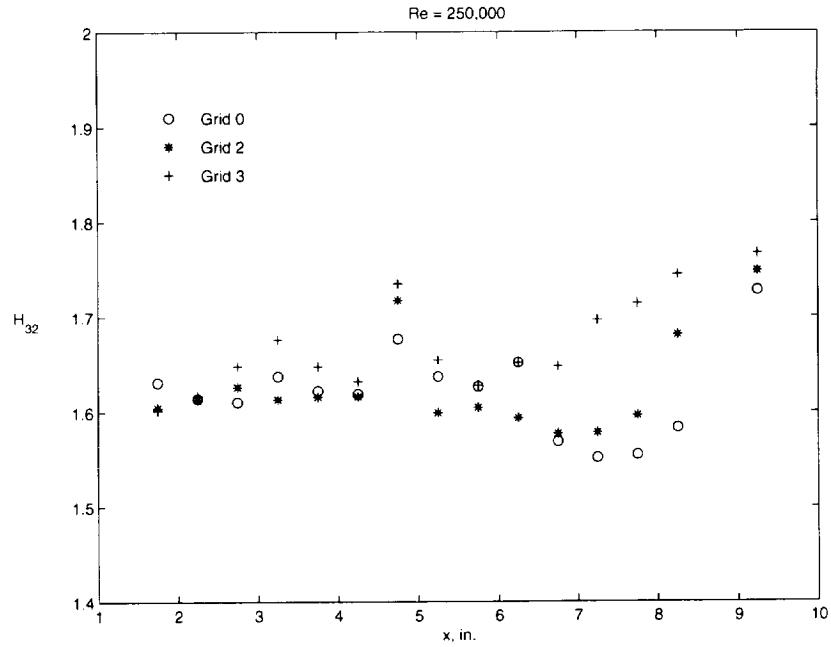

Figure 68 Energy shape factor profiles, grids 0, 2 and 3, Re = 250,000

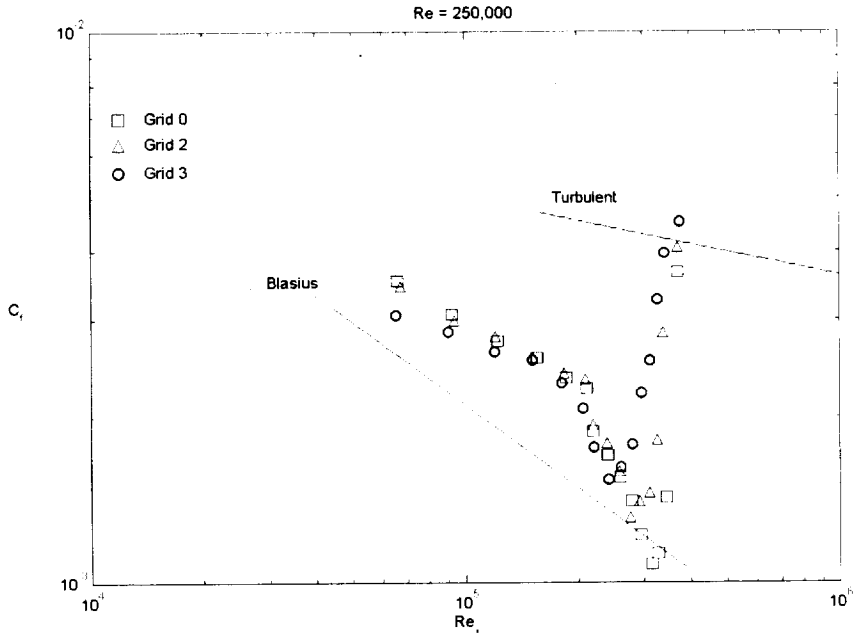

Figure 69 Skin friction coefficient, grids 0, 2 and 3, Re = 250,000

Table 8 Boundary Layer Properties at Separation, Re = 100,000

	δ^*, in.*	θ, in.*	ε, in.*	H_{12}	H_{32}	Re_x	Re_θ
Grid 0	0.04441	0.01247	0.01897	3.562	1.522	93913	223
Grid 2	0.04646	0.01257	0.01914	3.696	1.522	101315	243
Grid 3	0.04871	0.01337	0.02036	3.643	1.523	99615	254

*__Note:__ 1 inch = 2.54 cm.

Table 9 Boundary Layer Properties, Grid 0, Re = 100,000

x, in.**	u_e, ft/s**	δ^*, in.**	θ, in.**	ε, in.**	H_{12}	H_{32}	Re_x	Re_θ	c_f
1.75	31.650	0.01357	0.00544	0.00875	2.495	1.608	29015	90	-
2.25	33.540	0.01400	0.00562	0.00905	2.486	1.610	40385	101	-
2.75	36.952	0.01436	0.00605	0.00990	2.374	1.637	53134	117	-
3.25	38.087	0.01762	0.00965	0.01691	1.825	1.752	65081	193	-
3.75	37.628	0.02140	0.01187	0.02089	1.803	1.759	76025	241	-
4.25	37.621	0.02207	0.00819	0.01287	2.694	1.571	83732	161	-
4.75	36.158	0.02960	0.01001	0.01553	2.956	1.551	89729	189	0.18271
5.25	35.443	0.04441	0.01247	0.01897	3.562	1.522	93913	223	0*
5.75	34.777	0.06703	0.01531	0.02279	4.377	1.488	100822	268	0*
6.25	34.495	0.08432	0.01763	0.02582	4.782	1.464	108846	307	0*
6.75	32.707	0.06855	0.02339	0.03483	2.931	1.489	111498	386	0*
7.25	31.572	0.05353	0.03064	0.05132	1.747	1.675	115838	490	0.20679
7.75	31.549	0.04758	0.03176	0.05545	1.498	1.746	124207	509	0.22520
8.25	31.644	0.04756	0.03264	0.05785	1.457	1.773	132712	525	0.22987
8.75	31.637	0.04803	0.03303	0.05886	1.454	1.782	140728	531	0.23037
9.25	31.696	0.04921	0.03372	0.06022	1.459	1.786	149003	543	0.23036

*__Note:__ Separated flow at this location.
**__Note:__ 1 inch = 2.54 cm. 1 ft/sec = 0.3048 m/sec.

Table 10 Boundary Layer Properties, Grid 2, Re = 100,000

x, in.**	u_e, ft/s**	δ^*, in.**	θ, in.**	ε, in.**	H_{12}	H_{32}	Re_x	Re_θ	c_f
1.75	31.329	0.01315	0.00525	0.00851	2.506	1.622	28601	86	-
2.25	34.334	0.01475	0.00674	0.01150	2.189	1.706	40278	121	-
2.75	37.356	0.01606	0.00810	0.01413	1.981	1.743	53517	158	-
3.25	39.669	0.01682	0.00817	0.01410	2.058	1.726	67181	169	-
3.75	40.423	0.01886	0.00914	0.01571	2.063	1.719	79057	193	-
4.25	39.423	0.02060	0.00868	0.01435	2.372	1.653	87363	178	-
4.75	39.006	0.03180	0.01028	0.01609	3.024	1.565	93737	203	0.15358
5.25	38.209	0.04646	0.01257	0.01914	3.696	1.522	101315	243	0*
5.75	37.884	0.06653	0.01502	0.02233	4.429	1.486	109947	287	0*
6.25	36.585	0.06515	0.02200	0.03289	2.961	1.495	115409	406	0*
6.75	34.639	0.05013	0.02782	0.04600	1.802	1.653	118255	487	0.20600
7.25	32.946	0.04658	0.03086	0.05329	1.509	1.727	120888	515	0.22311
7.75	32.812	0.04594	0.03164	0.05560	1.452	1.758	128872	526	0.22895
8.25	32.825	0.04668	0.03239	0.05742	1.441	1.773	137193	539	0.23103
8.75	32.753	0.04806	0.03404	0.06056	1.412	1.779	145236	565	0.22983
9.25	32.740	0.05035	0.03462	0.06161	1.454	1.779	153423	574	0.22924

*__Note:__ Separated flow at this location.
**__Note:__ 1 inch = 2.54 cm. 1 ft/sec = 0.3048 m/sec.

Table 11 Boundary Layer Properties, Grid 3, Re = 100,000

x, in.**	u_e, ft/s**	δ^*, in.**	θ, in.**	ε, in.**	H_{12}	H_{32}	Re_x	Re_θ	c_f
1.75	30.354	0.01385	0.00566	0.00935	2.449	1.653	27935	90	-
2.25	33.166	0.01404	0.00579	0.00974	2.424	1.681	39187	101	-
2.75	37.116	0.01592	0.00787	0.01377	2.024	1.751	53527	153	-
3.25	39.685	0.01842	0.00999	0.01780	1.844	1.783	67598	208	-
3.75	40.791	0.01834	0.00930	0.01620	1.972	1.741	80129	199	-
4.25	40.574	0.01985	0.00937	0.01594	2.118	1.700	90241	199	-
4.75	38.324	0.03004	0.01055	0.01658	2.847	1.572	92291	205	0.15358
5.25	37.438	0.04871	0.01337	0.02036	3.643	1.523	99615	254	0*
5.75	36.552	0.05572	0.01701	0.02569	3.275	1.510	106414	315	0*
6.25	34.738	0.04821	0.02296	0.03671	2.169	1.599	109963	404	0.18893
6.75	33.947	0.04223	0.02584	0.04421	1.634	1.711	116251	445	0.22246
7.25	33.661	0.04181	0.02823	0.04911	1.481	1.740	124020	483	0.22801
7.75	33.547	0.04410	0.02964	0.05220	1.488	1.761	132121	505	0.23067
8.25	33.468	0.04576	0.03145	0.05557	1.455	1.767	140312	535	0.23049
9.25	33.465	0.05074	0.03430	0.06098	1.479	1.778	157357	584	0.22901

***Note:** Separated flow at this location.

****Note:** 1 inch = 2.54 cm. 1 ft/sec = 0.3048 m/sec.

Table 12 Boundary Layer Properties, Grid 0, Re = 250,000

x, in.**	u_e, ft/s **	δ^*, in.**	θ, in.**	ε, in.**	H_{12}	H_{32}	Re_x	Re_θ	c_f
1.75	72.569	0.00926	0.00390	0.00637	2.372	1.631	66186	148	0.00356
2.25	78.871	0.00936	0.00370	0.00597	2.529	1.614	92263	151	0.00309
2.75	85.361	0.00952	0.00358	0.00577	2.659	1.611	122527	159	0.00276
3.25	91.480	0.00981	0.00400	0.00655	2.455	1.638	155750	192	0.00257
3.75	94.777	0.01014	0.00402	0.00652	2.524	1.622	186208	199	0.00237
4.25	95.486	0.01046	0.00421	0.00682	2.485	1.619	212402	210	0.00226
4.75	94.334	0.01319	0.00501	0.00815	2.635	1.629	220673	233	0.00189
5.25	93.179	0.01434	0.00547	0.00871	2.621	1.593	240586	251	0.00171
5.75	92.024	0.01605	0.00609	0.00964	2.633	1.582	260233	276	0.00156
6.25	90.689	0.01798	0.00693	0.01093	2.593	1.576	279037	309	0.00141
6.75	88.809	0.02021	0.00755	0.01182	2.675	1.564	295825	331	0.00123
7.25	88.137	0.02287	0.00821	0.01273	2.783	1.549	315204	357	0.00108
7.75	85.948	0.02518	0.00916	0.01419	2.749	1.549	328270	388	0.00114
8.25	84.652	0.02730	0.01096	0.01701	2.491	1.560	344940	458	0.00144
9.25	81.332	0.02783	0.01599	0.02772	1.740	1.734	371495	642	0.00368

**__Note:__ Separated flow at this location.

**__Note:__ 1 inch = 2.54 cm. 1 ft/sec = 0.3048 m/sec.

Table 13 Boundary Layer Properties, Grid 2, Re = 250,000

x, in.**	u_e, ft/s**	δ^*, in.**	θ, in.**	ε, in.**	H_{12}	H_{32}	Re_x	Re_θ	c_f
1.75	74.157	0.00921	0.00414	0.00677	2.223	1.635	67237	159	0.00363
2.25	80.663	0.01022	0.00493	0.00834	2.073	1.692	93929	206	0.00319
2.75	85.105	0.01116	0.00556	0.00959	2.009	1.727	120713	244	0.00288
3.25	90.512	0.01116	0.00529	0.00905	2.110	1.710	151445	247	0.00258
3.75	94.751	0.01133	0.00512	0.00863	2.215	1.686	184021	251	0.00228
4.25	95.433	0.01168	0.00509	0.00845	2.296	1.661	209893	251	0.00214
4.75	93.622	0.01525	0.00717	0.01227	2.127	1.711	220072	332	0.00199
5.25	92.464	0.01490	0.00609	0.00974	2.445	1.599	240309	279	0.00173
5.75	91.204	0.01672	0.00659	0.01056	2.538	1.603	258562	296	0.00160
6.25	89.590	0.01904	0.00752	0.01198	2.532	1.592	276256	332	0.00145
6.75	87.904	0.02141	0.00862	0.01360	2.483	1.578	292926	374	0.00145
7.25	86.880	0.02378	0.01001	0.01585	2.375	1.583	311783	431	0.00159
7.75	85.010	0.02683	0.01247	0.01990	2.152	1.596	326768	526	0.00199
8.25	83.045	0.02538	0.01463	0.02445	1.735	1.671	338786	601	0.00329
9.25	80.761	0.02753	0.01809	0.03151	1.522	1.742	370633	725	0.00445

***Note:** Separated flow at this location.

****Note:** 1 inch = 2.54 cm. 1 ft/sec = 0.3048 m/sec.

Table 14 Boundary Layer Properties, Grid 3, Re = 250,000

x, in.**	u_e, ft/s**	δ^*, in.**	θ, in.**	ε, in.**	H_{12}	H_{32}	Re_x	Re_θ	c_f
1.75	72.457	0.01024	0.00490	0.00826	2.087	1.683	65492	383	0.00361
2.25	77.874	0.01048	0.00508	0.00867	2.065	1.707	90494	422	0.00327
2.75	84.514	0.01133	0.00582	0.01012	1.948	1.740	120130	495	0.00293
3.25	90.141	0.01238	0.00658	0.01158	1.881	1.761	151481	577	0.00261
3.75	93.412	0.01286	0.00670	0.01177	1.919	1.756	181306	622	0.00239
4.25	94.226	0.01303	0.00647	0.01116	2.015	1.725	207416	636	0.00221
4.75	93.530	0.01751	0.00877	0.01522	1.997	1.736	221119	815	0.00190
5.25	92.389	0.01730	0.00767	0.01274	2.254	1.660	241895	797	0.00171
5.75	91.608	0.01782	0.00770	0.01254	2.315	1.629	261306	810	0.00170
6.25	90.177	0.01981	0.00966	0.01601	2.051	1.658	280061	888	0.00194
6.75	88.524	0.02119	0.00997	0.01636	2.126	1.641	296920	932	0.00224
7.25	86.759	0.02433	0.01338	0.02267	1.818	1.695	312555	1049	0.00264
7.75	85.085	0.02362	0.01415	0.02419	1.670	1.710	327886	999	0.00369
8.25	83.360	0.02333	0.01550	0.02704	1.505	1.745	342678	969	0.00472
9.25	81.316	0.02816	0.01915	0.03376	1.470	1.763	375916	1144	0.00477

*__Note:__ Separated flow at this location.
**__Note:__ 1 inch = 2.54 cm. 1 ft/sec = 0.3048 m/sec.

5. Intermittency Profiles

Intermittency profiles were computed from the digitally recorded mean velocity profile data. Intermittency, Γ, is defined as the fraction of time during which the flow at a given position remains turbulent after the onset of transition. A flow is considered fully turbulent if $\Gamma = 1$ and fully laminar if $\Gamma = 0$. The instantaneous velocity signal was segregated into turbulent and non-turbulent parts based on the squares of the first and second derivatives of the signals. The details of this technique can be found in papers by Hedley and Keffer (1974) and Sohn and Reshotko (1991). An illustration of this technique is shown in Figure 70. The intermittency profiles are shown in Figures 71-76.

Figure 71 is an intermittency profile plot for a Reynolds number of 100,000, grid 0, and it shows that transition begins between x=5.75 (14.61 cm) and x=6.25 inches (15.88 cm). A peak intermittency value occurs for x=6.25 inches (15.88 cm) at an approximate y/δ value of 0.5. As the flow proceeds downstream in the test section, the peak intermittency values move towards the wall with the flow becoming fully turbulent. Figures 72 and 73 are the intermittency profile plots for grids 2 and 3 for a Reynolds number of 100,000. These plots exhibit similar trends to the grid 0 intermittency plot except the transition point moves upstream and the transition length decreases. This transition process occurs in the shear layer which bounds the freestream flow and bubble surface. Additionally, the flat portions of the intermittency profiles for y/δ values < 0.2 for each condition correspond to the constant velocity region inside the separation bubble. Shear flow transition starts at approximately x=5.75 inches (14.61 cm) for grid 2 and before x=5.75 inches (14.61 cm) for grid 3, respectively. Peak intermittency values occur for grid 2 at x=5.75 inches (14.61 cm) at a y/δ value of approximately 0.25. Fully

turbulent flow occurs at approximately x=6.75 inches (17.14 cm) for grid 2 and at approximately x=6.25-6.75 inches (15.88-17.14 cm) for grid 3. Approximate transition onset and fully turbulent flow locations obtained from the intermittency profiles agree favorably with those deduced from the hot-film data for each condition.

Figures 74-76 are intermittency profile plots for a Reynolds number of 250,000 and grids 0, 2 and 3, respectively. Transition initiates at approximately x=7.25 inches (18.42 cm) for grid 0, between x=6.25-6.75 inches (15.88-17.14 cm) for grid 2 and between x=5.25-5.75 inches (13.33-14.61 cm) for grid 3. The transition length increases for each grid for a Reynolds number of 250,000 in comparison to the transition lengths for the same grids for a Reynolds number of 100,000. This difference can be attributed to the nature and type of transition that occurs at a particular Reynolds number. For the Reynolds number of 100,000, laminar shear flow transition occurs due to the separated flow region, whereas for the Reynolds number of 250,000, bypass transition occurs. Because of the intense mixing (energy) in the shear layer due to turbulent diffusion from the freestream for the Reynolds number of 100,000, the transition length is shorter as a result of the higher level of turbulent diffusion.

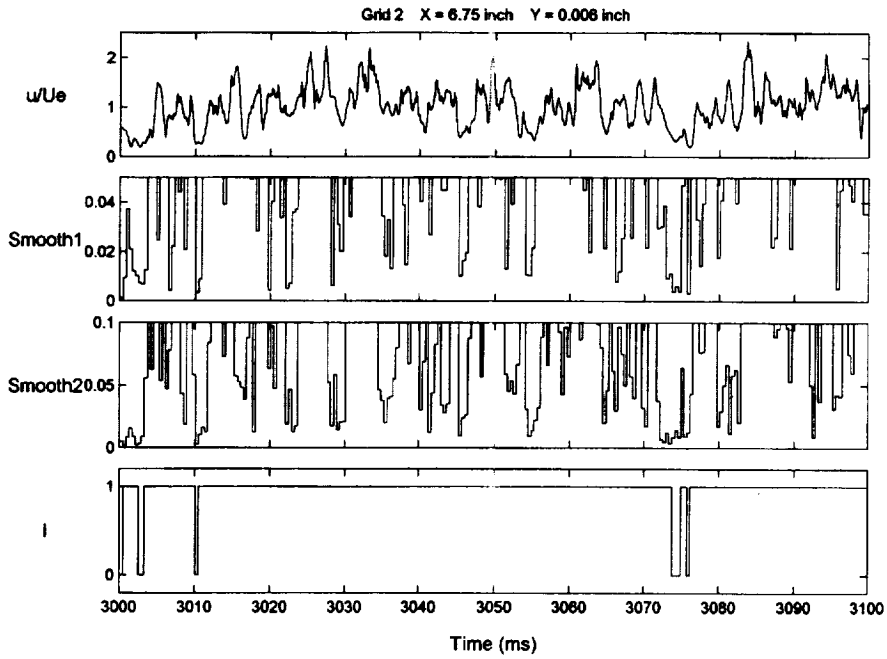

Figure 70 Indicator function determination technique for single wire

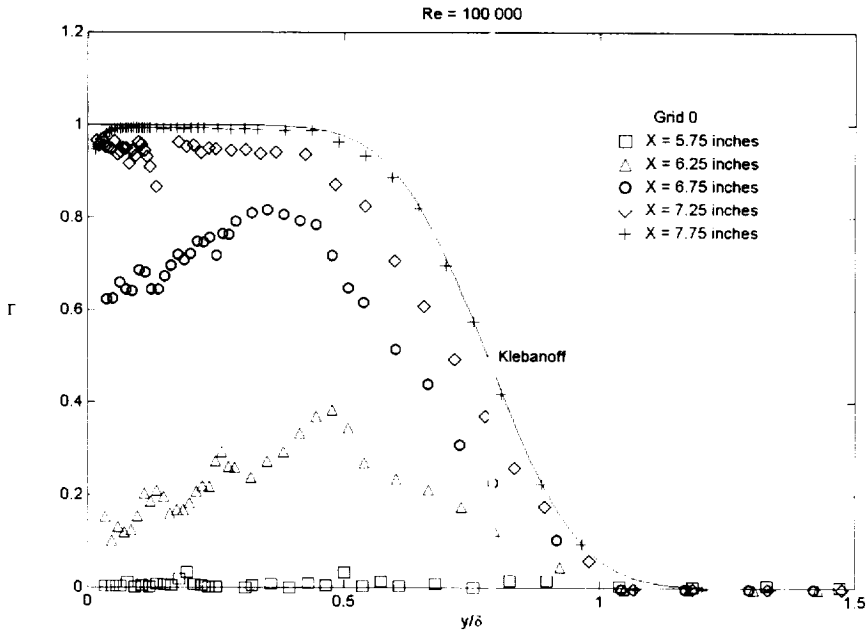

Figure 71 Downstream intermittency profiles, grid 0, Re = 100,000

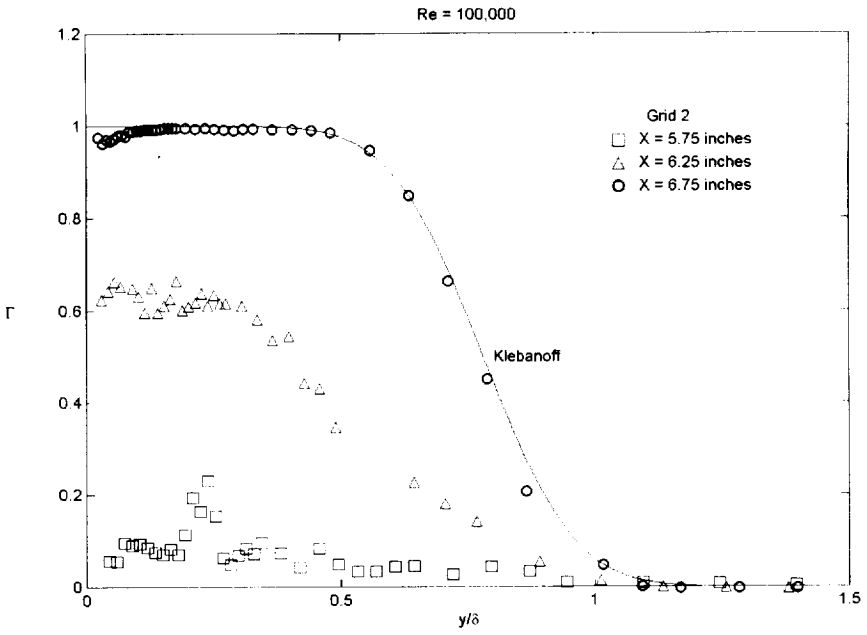

Figure 72 Downstream intermittency profiles, grid 2, Re = 100,000

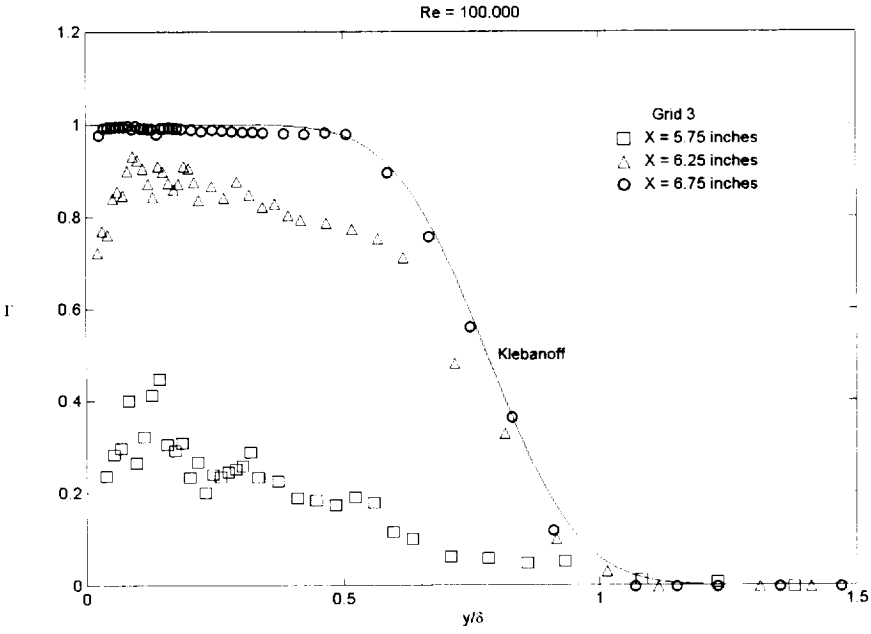

Figure 73 Downstream intermittency profiles, grid 3, Re = 100,000

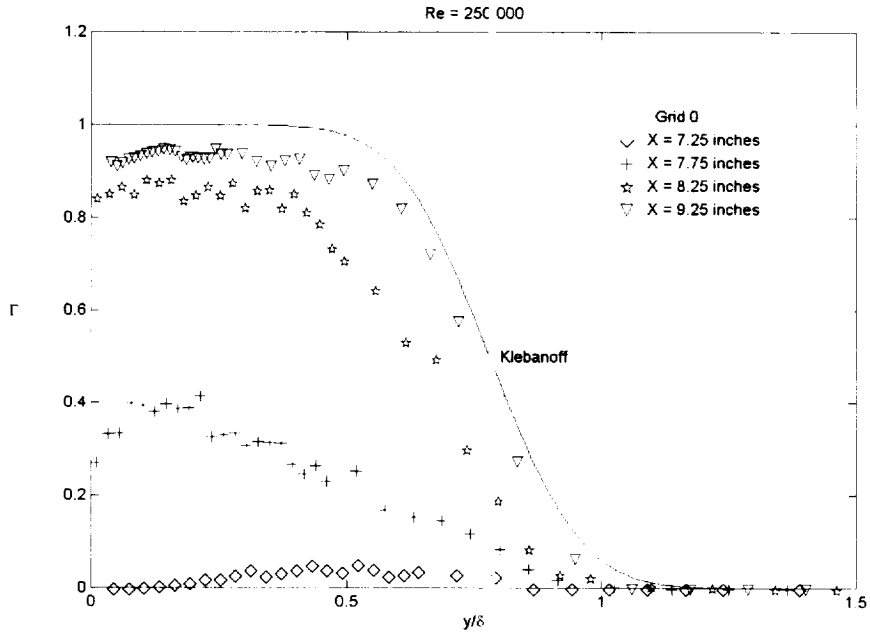

Figure 74 Downstream intermittency profiles, grid 0, Re = 250,000

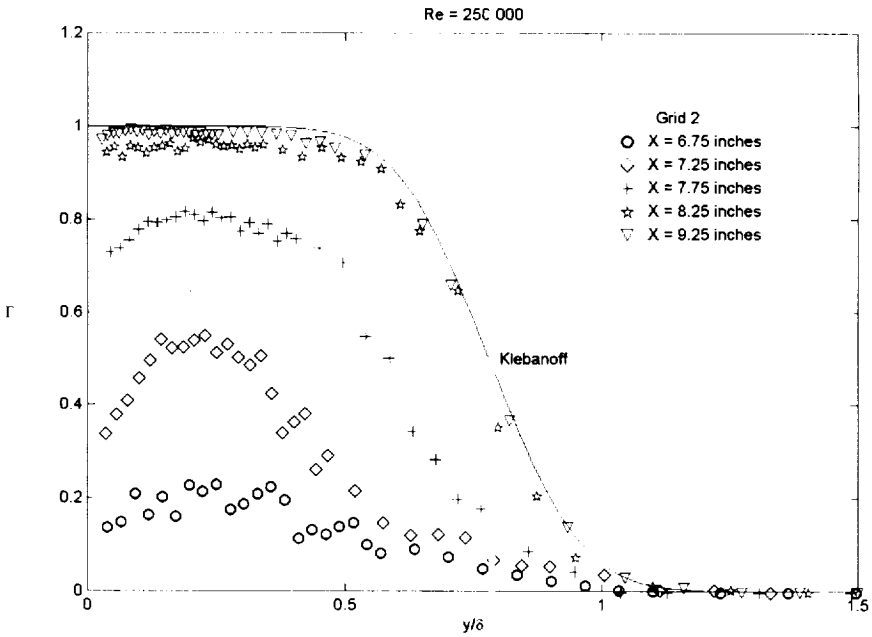

Figure 75 Downstream intermittency profiles, grid 2, Re = 250,000

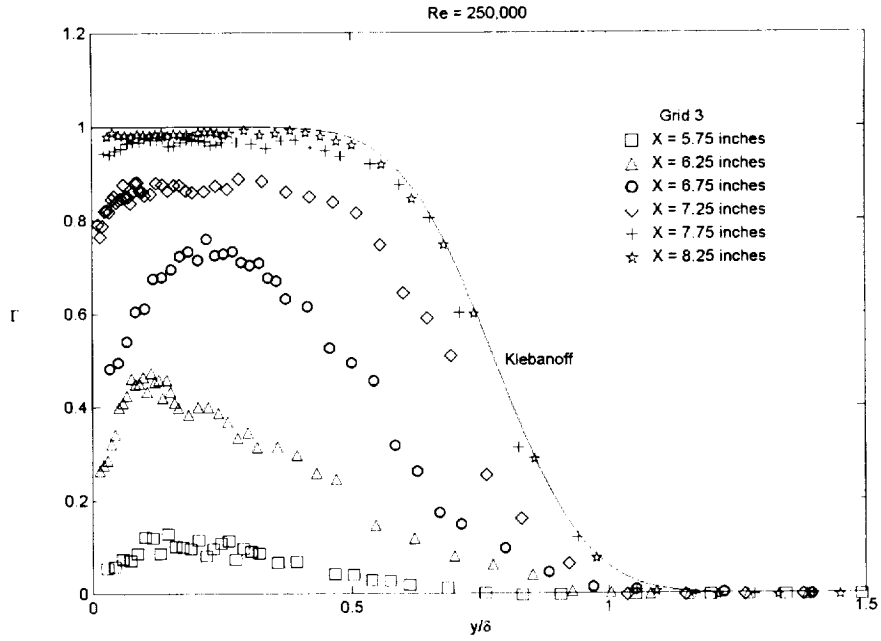

Figure 76 Downstream intermittency profiles, grid 3, Re = 250,000

6. Power Spectra Density Data

Results of power spectra density (PSD) data for Reynolds numbers of 100,000 and 250,000 are contained Figures 77-92. PSD data were taken in order to better understand the character and nature of the disturbances in the boundary layer and freestream regions of the flow field. Data was taken for grids 0, 2 and 3 at vertical distances above the plate corresponding to locations where the fluctuating velocity signal (rms) is a maximum and in the freestream of the flow field. For a Reynolds number of 100,000 the corresponding y values are $y = y(u'_{max}) = 0.015$ inches (0.038 cm) and $y = y(u'_{fs}) = 0.5$ inches (1.27 cm) for x=1.75 and 2.25 inches (4.45 and 5.72 cm) and $y = y(u'_{fs}) = 0.7$ inches (1.78 cm) for x=7.25 and 7.75 inches (18.14 and 19.68 cm). For a Reynolds number of 250,000 the corresponding y values are $y = y(u'_{max}) = 0.010$ inches

(0.0254 cm) and $y = y(u'_{fs}) = 0.5$ inches (1.27 cm) for x=1.75 and 2.25 inches (4.45 and 5.72 cm) and $y = y(u'_{fs}) = 0.7$ inches (1.78 cm) for x=7.25 and 7.75 inches (18.14 and 19.68 cm). The Nicolet FFT spectral analyzer used to make the PSD measurements is described in the instrumentation section. Spectral data was taken using an average of 100 scans and a sampling rate of 12.8 kHz.

Figures 77-82 are PSD plots for the maximum rms location at Reynolds numbers of 100,000 and 250,000. Figure 77 shows the PSD plot at the maximum rms position for grid 0 and a Reynolds number of 100,000. This data shows that almost all of the fluctuating energy is confined in low frequencies less than 700 Hz. at x= 4.75 and 5.25 inches (12.07 and 13.34 cm), resembling a laminar flow-field spectra. The flow field was contaminated by main and bleed blower noise and their sub-harmonics. A two-order of magnitude jump in PSD occurs at x=5.75 inches (14.61 cm) for low frequencies less than 1200 Hz. followed by a larger jump in the spectra for all frequency bands measured at x=6.25-6.75 inches (15.88-17.15 cm). This small jump around x= 5.75 inches (14.61 cm) indicates transition onset and the spectra increases in magnitude as the flow becomes fully turbulent as it moves downstream. This behavior agrees with the intermittency profile for grid 0 as shown in Figure 71. The PSD spectra over the separation bubble shows no broad band disturbance hump around 1500 Hz., which would be caused by a Kelvin-Helmholtz type instability in the flow-field. Additionally, the approximate locations of transition onset and fully turbulent flow deduced from the PSD agree favorably with those deduced from the intermittency profiles.

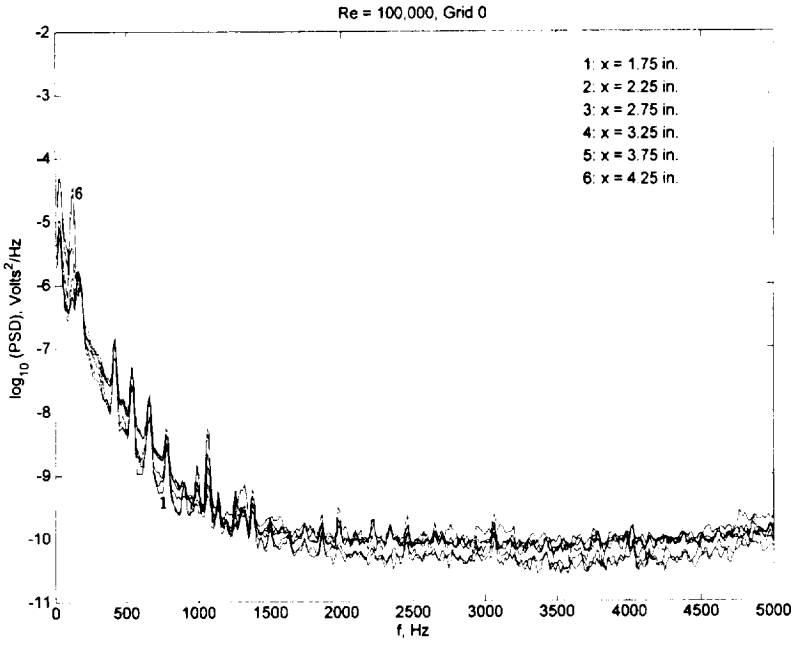

Figure 77 Upstream boundary layer spectra, $y = y(u'_{max})$, grid 0, Re = 100,000

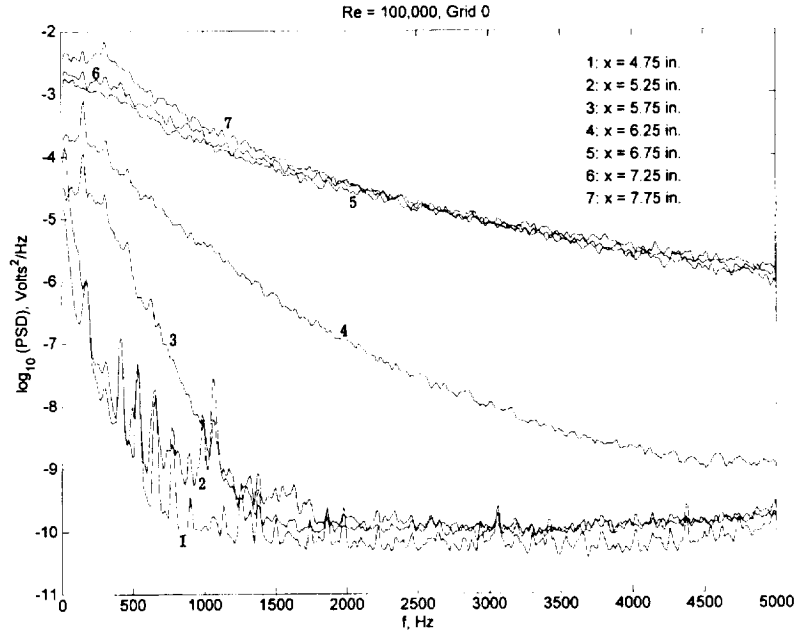

Figure 78 Downstream boundary layer spectra, $y = y(u'_{max})$, grid 0, Re = 100,000

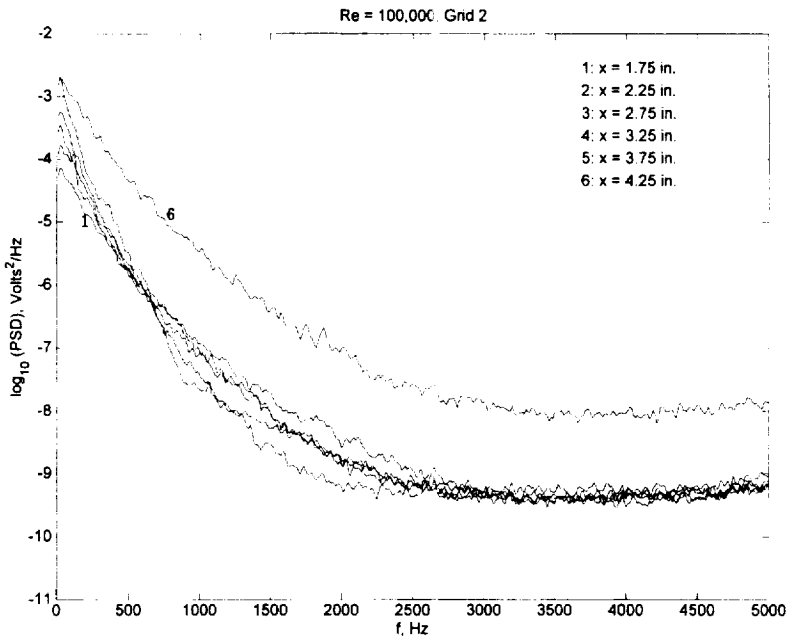

Figure 79 Upstream boundary layer spectra, $y = y(u'_{max})$, grid 2, Re = 100,000

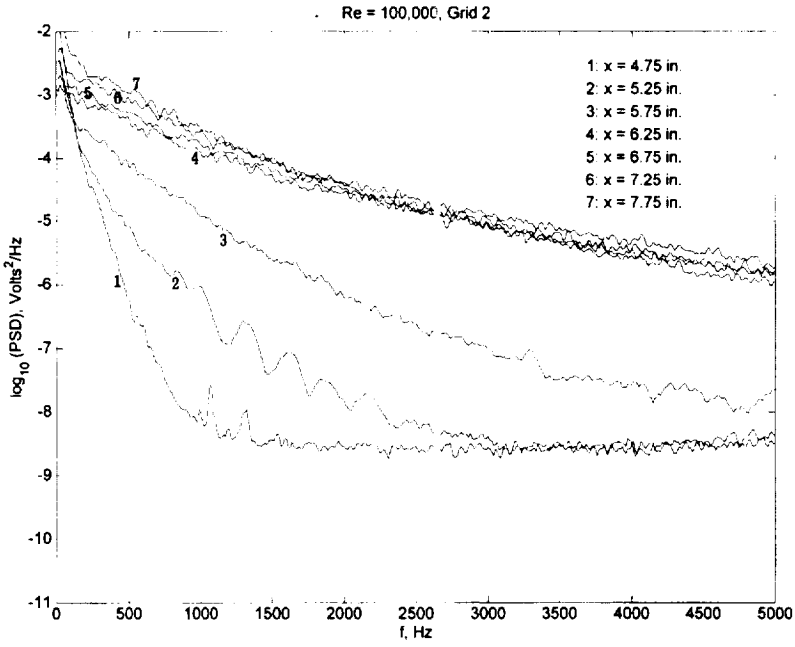

Figure 80 Downstream boundary layer spectra, $y = y(u'_{max})$, grid 2, Re = 100,000

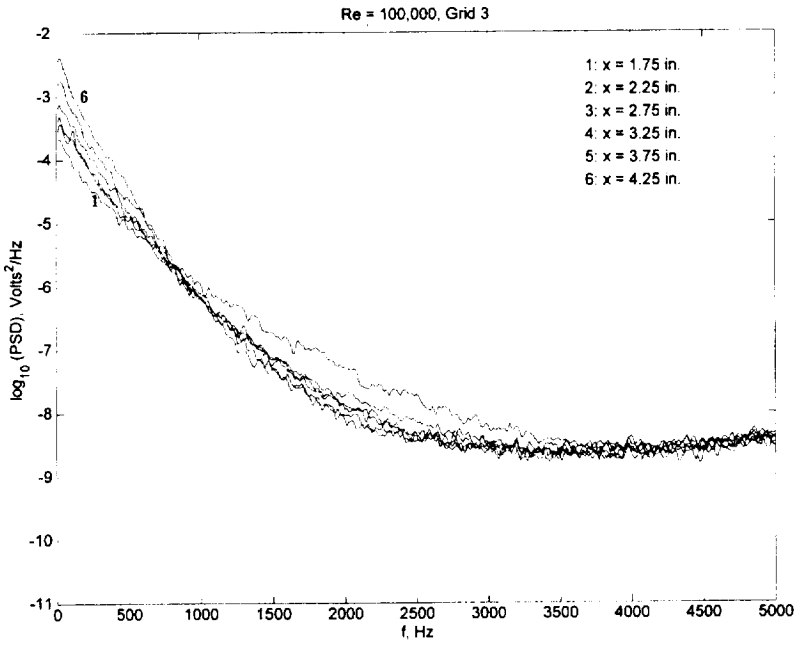

Figure 81 Upstream boundary layer spectra, $y = y(u'_{max})$, grid 3, Re = 100,000

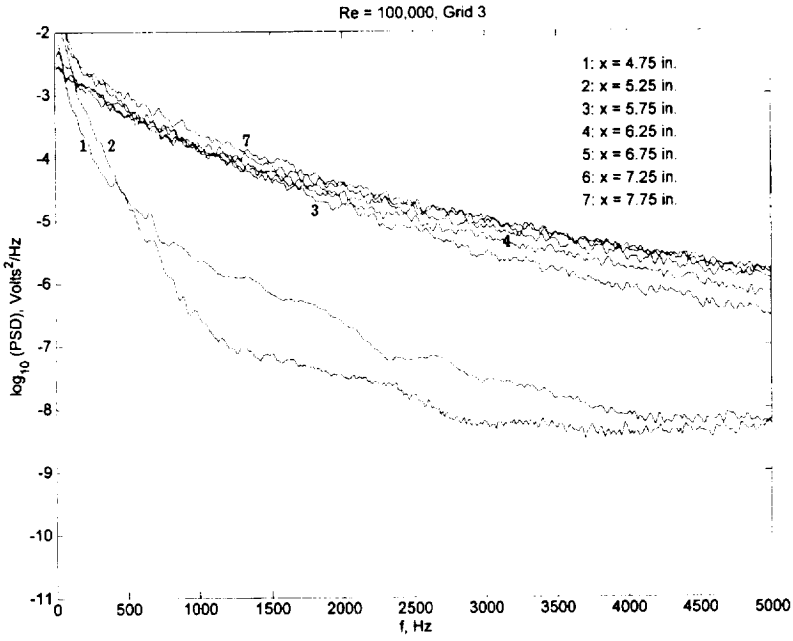

Figure 82 Downstream boundary layer spectra, $y = y(u'_{max})$, grid 3, Re = 100,000

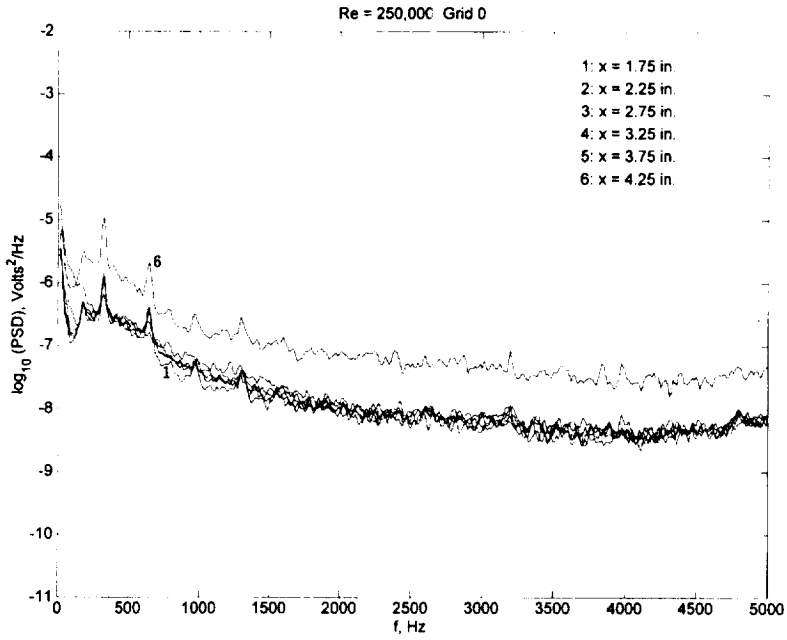

Figure 83 Upstream boundary layer spectra, $y = y(u'_{max})$, grid 0, Re = 250,000

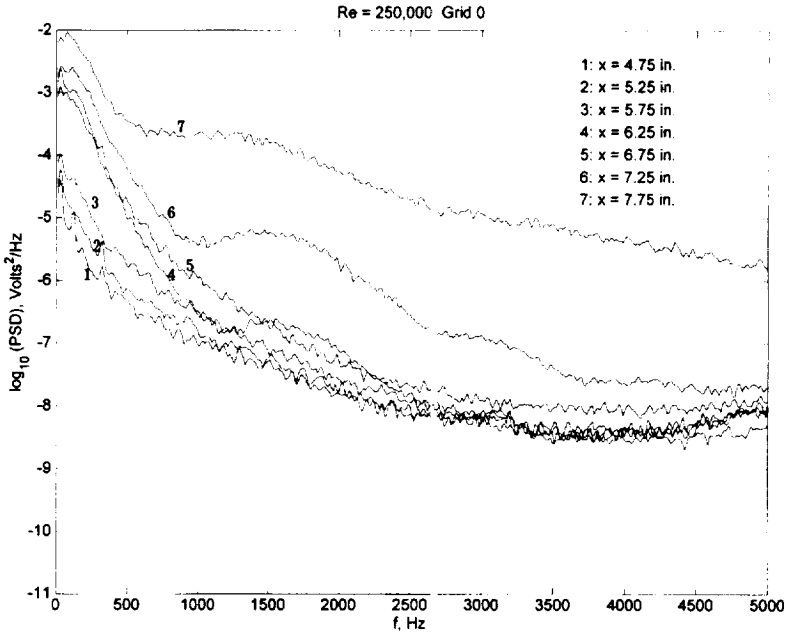

Figure 84 Downstream boundary layer spectra, $y = y(u'_{max})$, grid 0, Re = 250,000

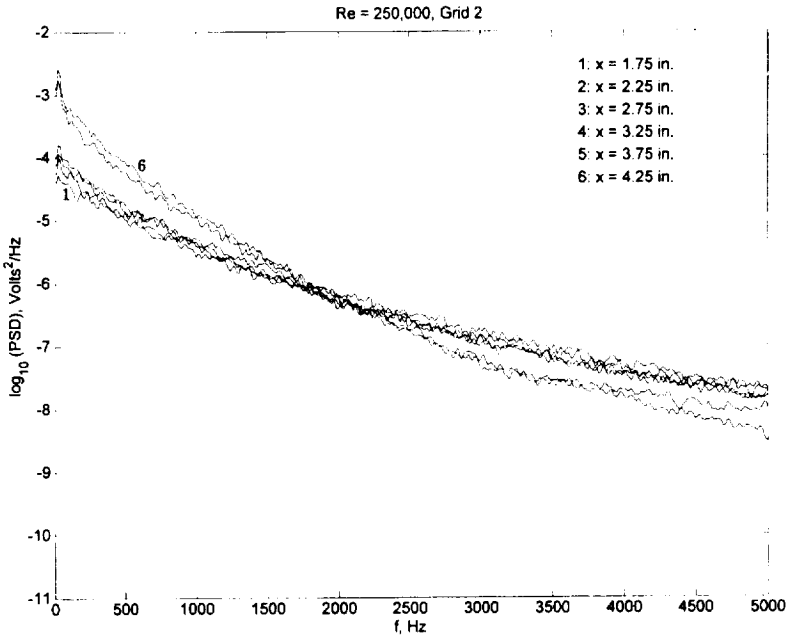

Figure 85 Upstream boundary layer spectra, $y = y(u'_{max})$, grid 2, Re = 250,000

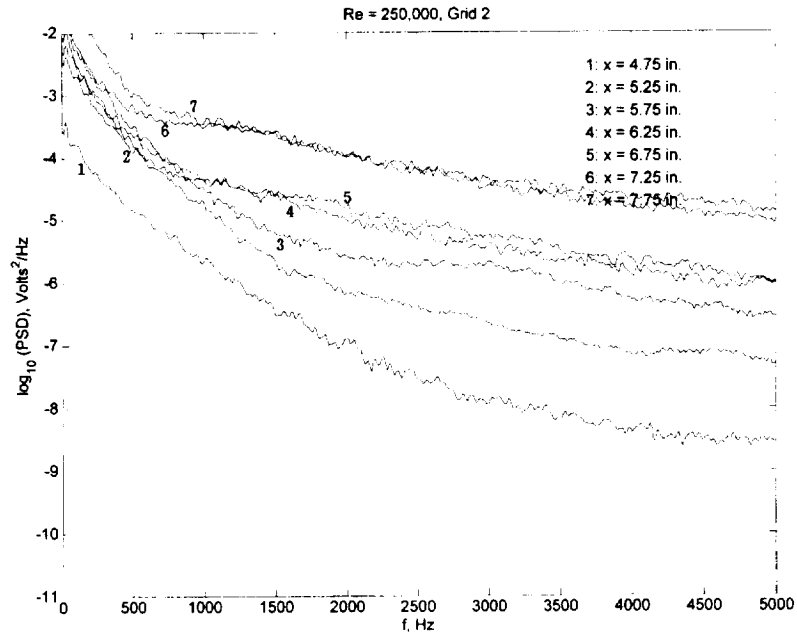

Figure 86 Downstream boundary layer spectra, $y = y(u'_{max})$, grid 2, Re = 250,000

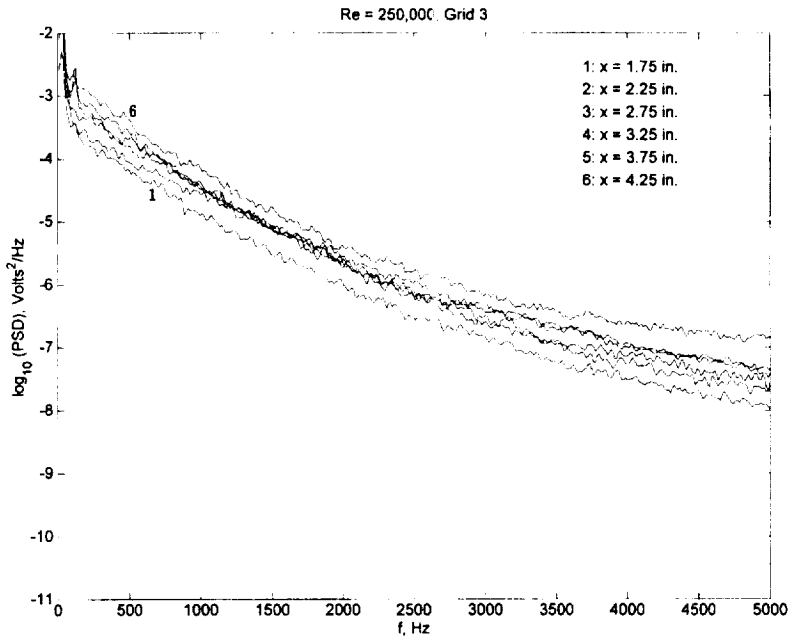

Figure 87 Upstream boundary layer spectra, $y = y(u'_{max})$, grid 3, Re = 250,000

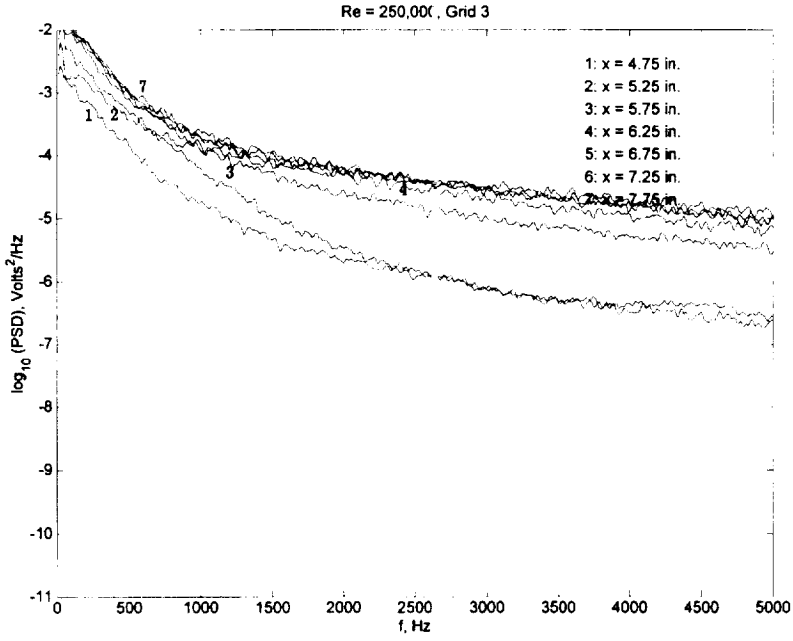

Figure 88 Downstream boundary layer spectra, $y = y(u'_{max})$, grid 3, Re = 250,000

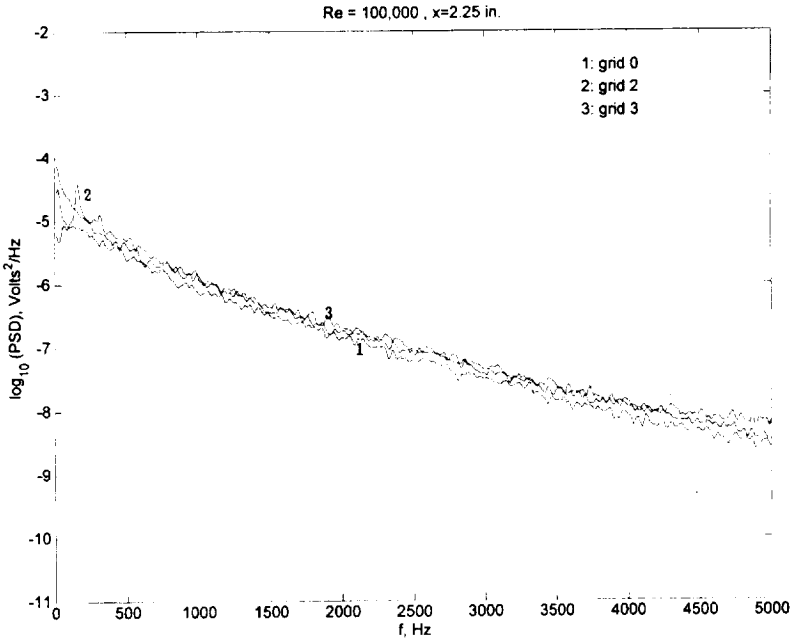

Figure 89 Boundary layer spectra, $y = y(u'_{fs})$, grids 0, 2 and 3, Re = 100,000, x=2.25 inches (5.72 cm)

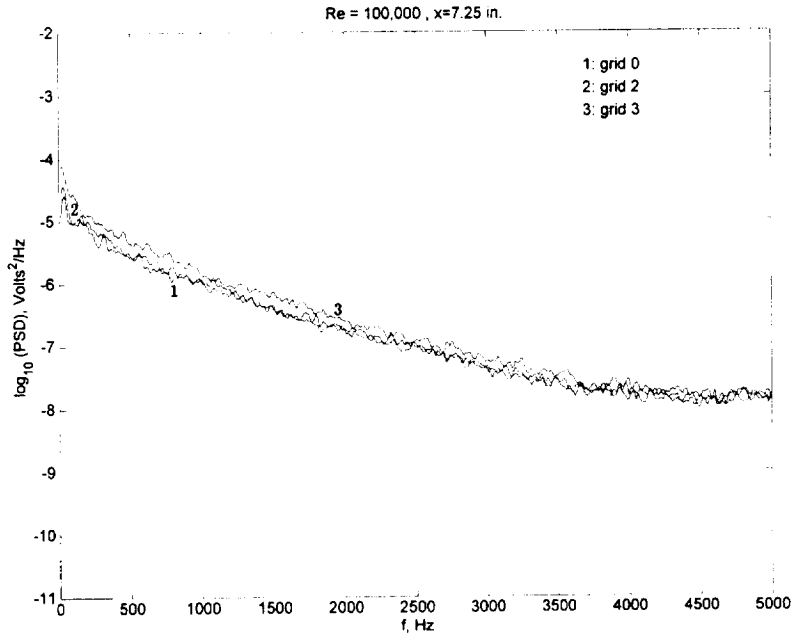

Figure 90 Boundary layer spectra, $y = y(u'_{fs})$, grids 0, 2 and 3, Re = 100,000, x=7.25 inches (18.42 cm)

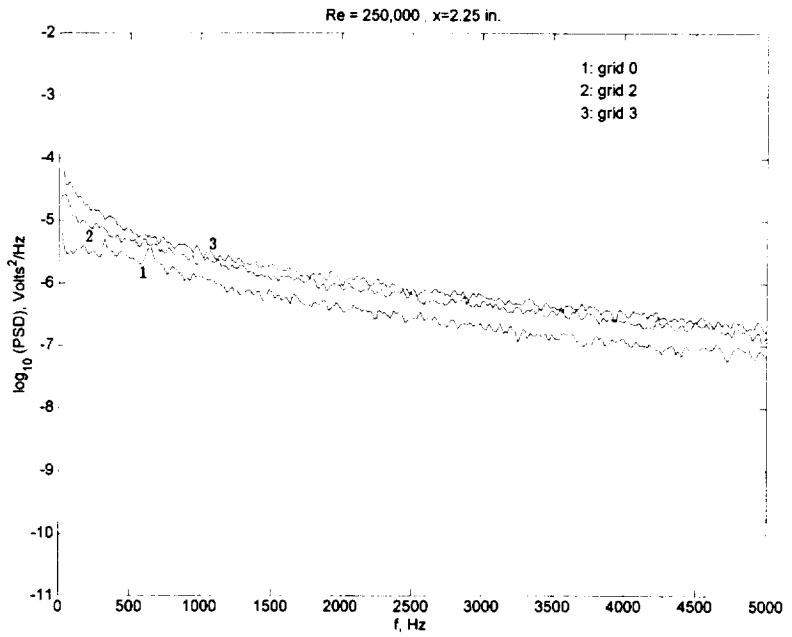

Figure 91 Boundary layer spectra, $y = y(u'_{fs})$, grids 0, 2 and 3, Re = 250,000, x=2.25 inches (5.72 cm)

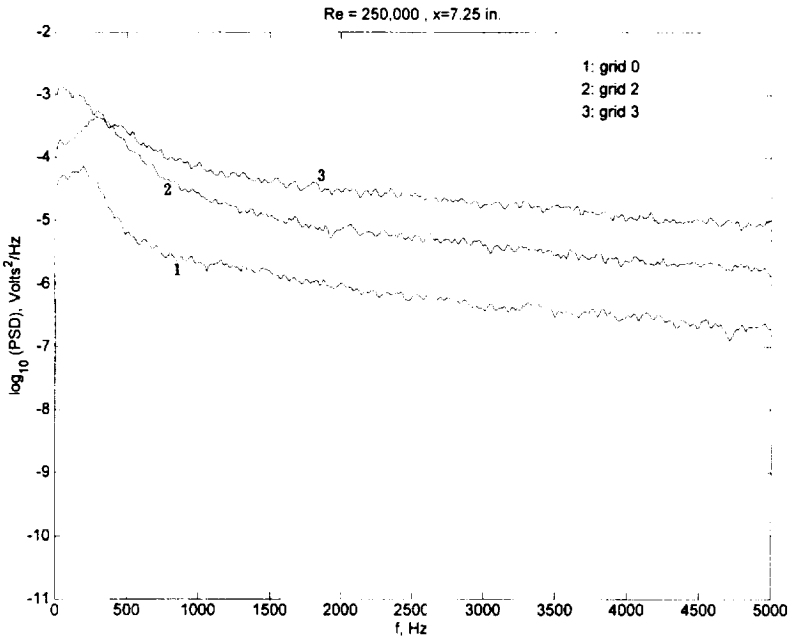

Figure 92 Boundary layer spectra, $y = y(u'_{s})$, grids 0, 2 and 3, Re = 250,000, x=7.25 inches (18.42 cm)

7. Integral Length Scales

The longitudinal integral length scales computed from the power spectral density data is summarized in Table 15. The integral scale is a measure of the characteristic length of the turbulent structure in the flow and it also gives a measure of the average size of the turbulent eddies. The length scales were computed from the following equations:

$$R = \frac{\overline{u_1' u_2'}}{\sqrt{\overline{u_1'^2}} \cdot \sqrt{\overline{u_2'^2}}}$$

$$L = \int_0^{1/2d} R(r)\, dr\,,$$

where u_1' and u_2' are axial fluctuating velocities measured at the same location, but at a different instant in time t_1 and $t_2 = t_1+t$, respectively. The integral length scale increases as the turbulence level increases and this is consistent for both Reynolds numbers tested.

Table 15 Λ, Longitudinal Integral Length Scale

	Grid 0	Grid 2	Grid 3
Re = 100,000	0.21 in. (0.53 cm)	0.62 in. (1.57 cm)	1.20 in. (3.05 cm)
Re = 250,000	0.33 in. (0.84 cm)	0.74 in. (1.88 cm)	1.34 in. (3.40 cm)

8. Classification of Separation Bubble

Gaster (1969) proposed a two parameter bubble bursting criterion using a relationship between momentum Reynolds number at separation Re_{θ_s}, and pressure parameter $\bar{P} = (\theta_s^2/\nu)(\Delta U/\Delta x)$. The criterion was based on his two sets of airfoil data and other researcher's experimental and calculated data. In the pressure parameter, ΔU is the rise in freestream velocity that would occur over the bubble length Δx in an unseparated

inviscid flow since the bubble shape is dependent on the pressure distribution that would occur without separation. Gaster's two parameter bursting criterion with pressure parameters measured in the present experiments are plotted in Figure 93. Three domains are defined in this figure. For $\bar{P} < -0.09$, the flow will not separate regardless of Reynolds number. To the right of the bursting boundary, a short bubble will be formed, and to the left, a long (bursting) bubble will be developed. It is clear that the bubbles formed in the present experiment are all of the short variety. In the present experiment, the inviscid pressure and ΔU are estimated from the Reynolds number of 250,000 case at which the boundary layers are attached for the entire test section.

Several empirical correlations have been developed accounting for the effects of freestream turbulence on the separation bubble length. Roberts (1975, 1980) related the transition length of the separation bubble to the turbulence scale factor, in which the turbulence scale is involved. The turbulence scale is a quantity not easily obtainable in experiments. Davis et al. (1985) modified the Roberts' correlation to replace the freestream turbulence factor with the local freestream turbulence level, which is $\mathrm{Re}_{l_1} = 25000 \times \log_{10}\{\coth[17.32 \times Tu)]\}$. The variation of transition length Reynolds number at separation along with Roberts' modified correlation is presented in Figure 94. The transition region determined from the intermittency profiles for each freestream turbulence level shows excellent agreement with this empirical correlation. Additionally, the boundary layer properties at separation are shown in Table 16 for grids 0, 2 and 3 and a Reynolds number of 100,000.

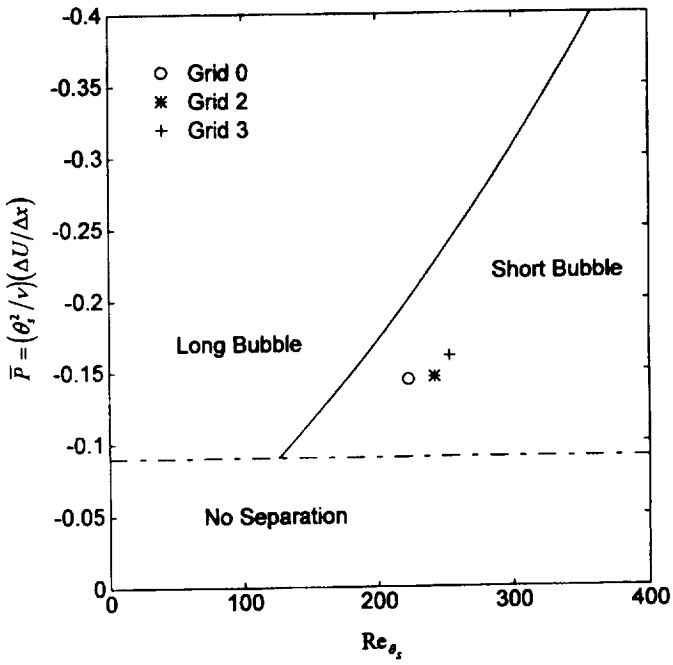

Figure 93 Gaster's two parameter bubble bursting criterion, Re = 100,000

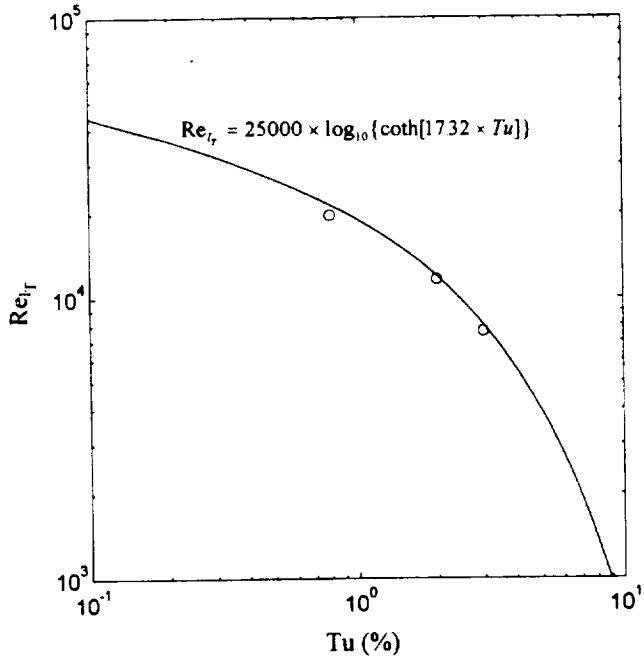

Figure 94 Modified Roberts' correlation, grids 0, 2 and 3, Re = 100,000

Table 16 Separation Bubble Characteristics, Re = 100,000

	X_S (in.)*	X_T (in.)*	X_R (in.)*	L_B (in.)*	L_T (in.)*	H_B (in.)*
Grid 0	≈5.25	5.75-6.25	≈6.85	≈1.60	0.5-1.10	≈0.042
Grid 2	≈5.25	≈5.75	≈6.25	≈1.00	≈0.50	≈0.022
Grid 3	≈5.25	<5.75	≈5.85	≈0.60	<0.50	≈0.012

***Note:** 1 inch =2.54 cm.

F. Hot-Film Data

A series of flush-mounted hot-film gages were used to identify and study the transition process on the flat plate. Figures 95-100 show results of the traces obtained from the flush mounted surface hot-film gages. The test matrix used for the hot-film traces is listed in Table 17. All fourteen gages could not be operated simultaneously due to the availability of only six constant temperature anemometer modules; therefore, four groups of six modules were used to obtain all of the traces. Hot-film signals are shown for the second set of gages only (7-12) which correspond to axial locations of 4.0, 4.5, 5.0, 5.5, 6.0 and 7.0 inches, (10.16, 11.43, 12.70, 13.97, 15.24 and 17.78 cm), respectively, measured from the leading edge. Hot-film traces for Figures 95-97 are for a Reynolds number of 100,000 with a separation bubble present and Figures 98-100 are for a Reynolds number of 250,000 with fully attached flow.

Figure 95 represents the hot-film traces obtained for grid 0 (0.8% TI) at a Reynolds number of 100,000. This figure shows the traces of the second six gages (7-12) which start downstream (x=4.0 inches, 10.16 cm) of the test section throat (x=3.75 inches, 9.53 cm) and extends into the adverse pressure gradient region to x=7.0 inches (17.78 cm). These hot-film traces exhibit a typical laminar behavior as shown by the

signals for x= 4.0, 4.5, 5.0, 5.5 and 6.0 inches (10.16, 11.43, 12.70, 13.97 and 15.24 cm), respectively. This can be attributed to the low freestream turbulence and acceleration of the flow through the converging region which stabilizes (relaminarizes) the flow and suppresses some of the effects of the freestream turbulence and pressure gradient. However, as the flow progresses downstream the hot-film signal becomes highly intermittent, indicating the presence of some type of flow instability. The instability encountered in this case is transition as shown by the signal at x=7.0 inches (17.78 cm). This signal shows that the flow is in the late stages of transition and close to becoming fully turbulent. The detection of transition at this location correlates well with the hot-wire (intermittency and velocity contour, figures 71 and 26) measurement data which shows that the flow is almost fully turbulent at x=7.0 inches (17.78 cm).

This behavior is more pronounced for grids 2 and 3 (freestream turbulence levels of 2% and 3%, respectively) as shown in Figures 96 and 97. For grid 2 the onset of transition is initiated at approximately x=6.0 inches (15.24 cm). Turbulent spots can be seen in the signal at times of approximately 142-145 milliseconds, 170-172 milliseconds and 176-178 milliseconds at x=6.0 inches. The hot-film signal at x=7.0 inches (17.78 cm) is representative of a near fully turbulent flow and its highly intermittent signal. The hot-film traces for grid 3 reveals that transition onset is detected by the hot-film gage located at x=5.5 inches (13.97 cm). Turbulent spots are evident in the signal at times of approximately 1355-1356 milliseconds, 1391-1396 milliseconds and 1398-1402 milliseconds, respectively. At the next hot-film location, x=6.0 inches (15.24 cm), the turbulent spots have grown significantly and are close to completely merging and forming a fully turbulent flow. The hot-film trace at x=7.0 inches (17.78 cm) is again

representative of a fully turbulent signal and these traces for grids 2 and 3 demonstrate the effect freestream turbulence intensity has on the transition process. The hot-film traces for all three grids for a Reynolds number of 100,000 show that the transition process experienced by the flow is of a shear layer type in contrast to a bypass or natural transition process. A bypass transition type flow is characterized by the development of turbulent spots, whereas in a shear layer transition type flow turbulent spots do not form.

Figures 98-100 show the hot-film traces for a Reynolds number of 250,000 and grids 0, 2 and 3. As expected the transitional process begins farther upstream than the lower Reynolds case (100,000) and intermittent turbulent spots begin to develop at x=5.5 inches (13.97 cm), x=5.0 inches (12.70 cm) and x=4.0 inches (10.16 cm) for grids 0, 2 and 3, respectively. For grid 0, turbulent spots are visible in the hot-film traces at x=5.5, 6.0 and 7.0 inches (12.70, 15.24 and 17.78 cm) at a time interval of approximately 1493-1496 milliseconds. Turbulent spots can be seen in the hot film traces for grid 2 at x=5.5, 6.0 and 7.0 inches (13.97, 15.24 and 17.78 cm) at approximate times of 78-82 milliseconds and also at times of 117-118 milliseconds and 60-70, 98-101, 133-136 and 140-150 milliseconds at x= 7.0 inches (17.78 cm). For grid 3, numerous turbulent spots are clearly visible at all hot-film locations at 324-326, 333-336 and 342-344 milliseconds and multiple spots appear as the flow moves downstream. The transitional process for this Reynolds number is of the bypass type and is contrast to the case for a Reynolds number of 100,000 in which transition starts earlier, but takes a longer time and has to travel farther downstream to achieve fully turbulent flow.

Table 17 Hot-film Gage Test Matrix

	Set 1	Set 2	Set 3	Set 4
Gages	1-6	7-12	9-14	5, 7, 9, 11, 12, 13, 14

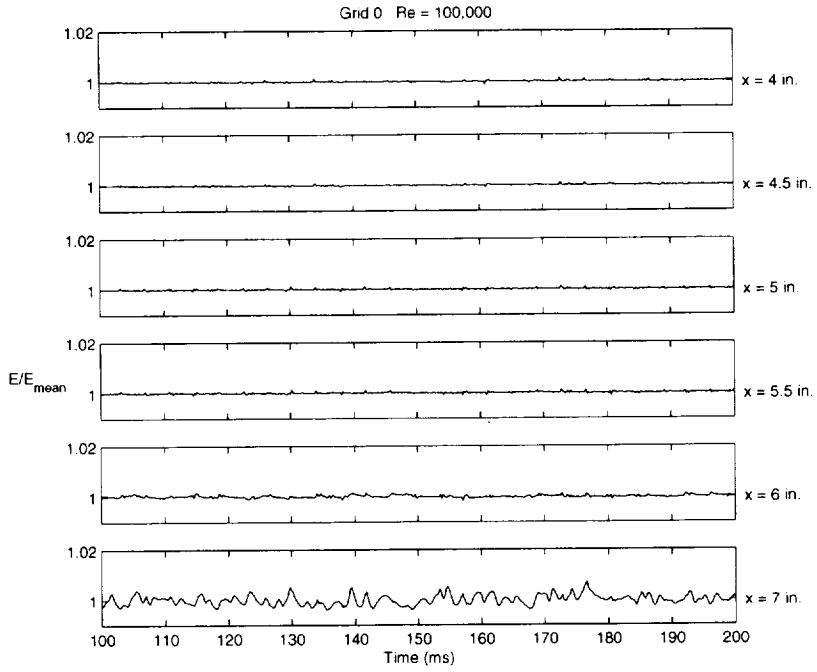

Figure 95 Hot-film gage voltage traces, grid 0, Re = 100,000

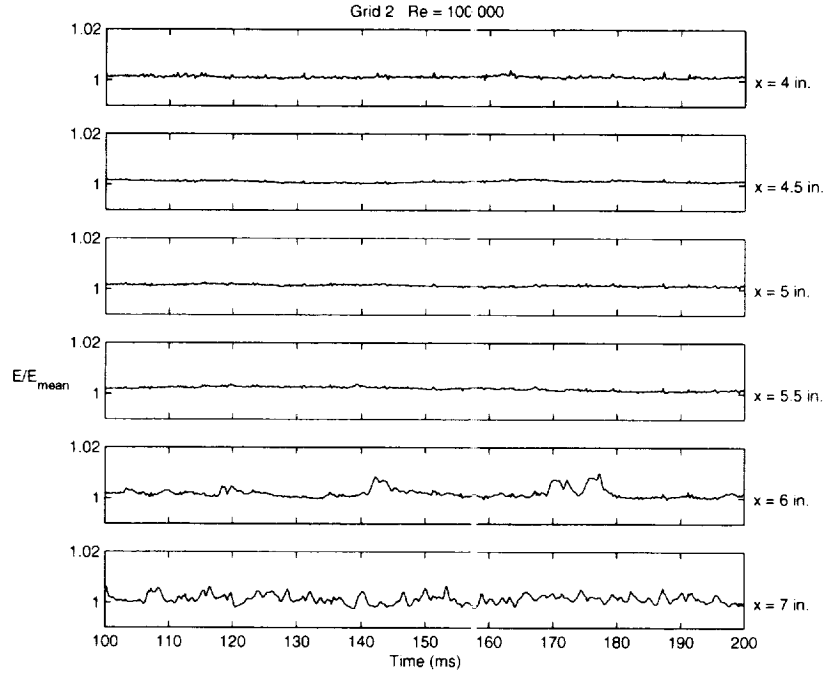

Figure 96 Hot-film gage voltage traces, grid 2, Re = 100,000

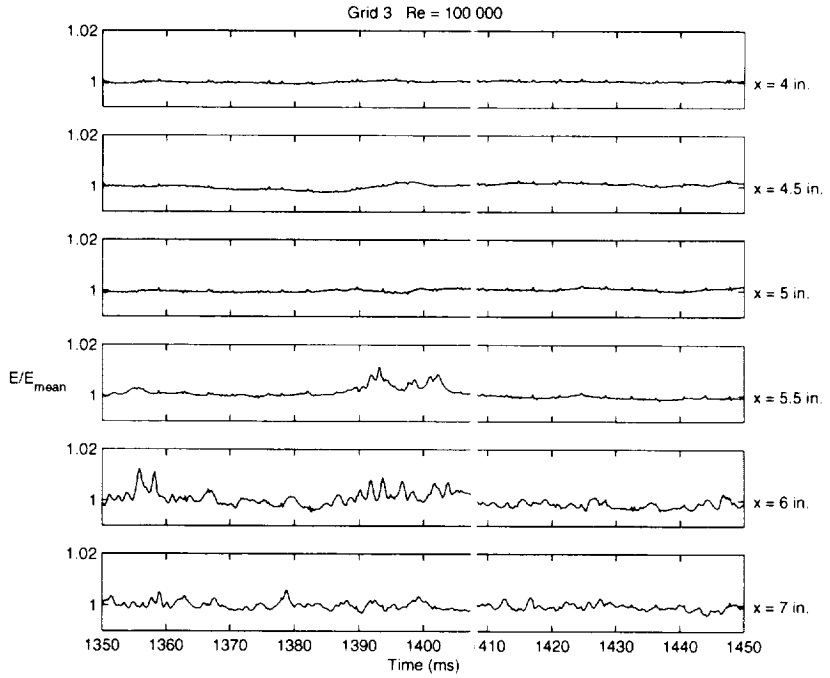

Figure 97 Hot-film gage voltage traces, grid 3, Re = 100,000

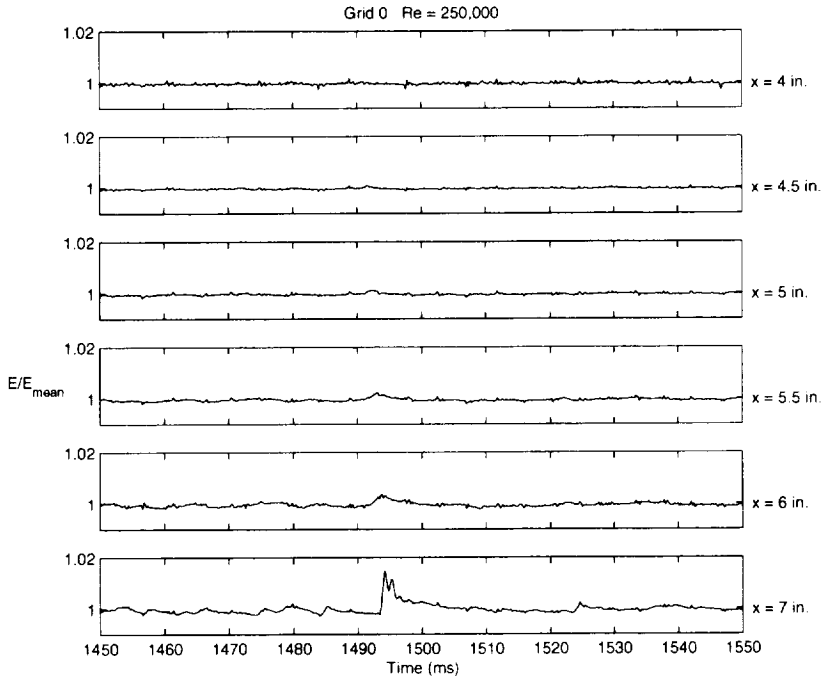

Figure 98 Hot-film gage voltage traces, grid 0, Re = 250,000

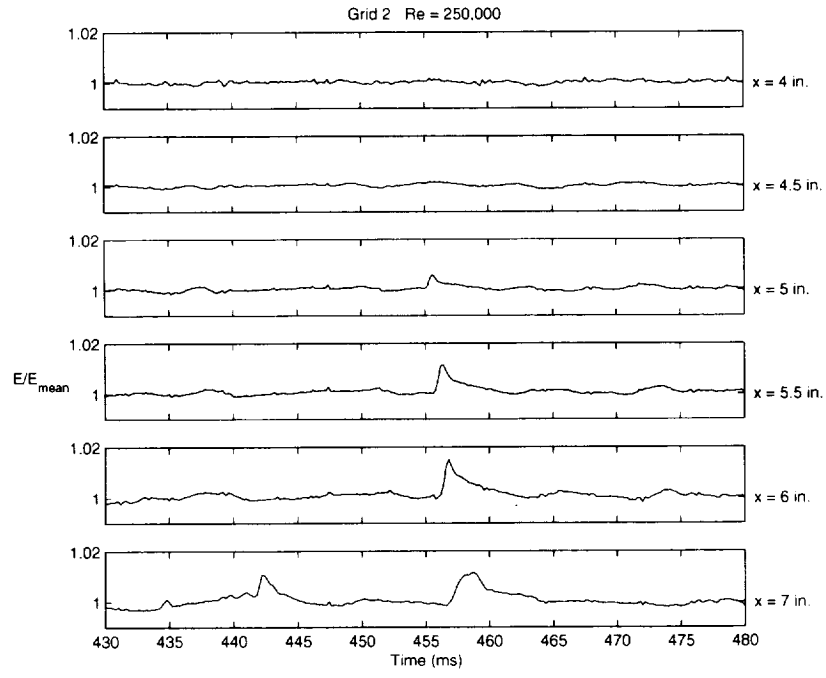

Figure 99 Hot-film gage voltage traces, grid 2, Re = 250,000

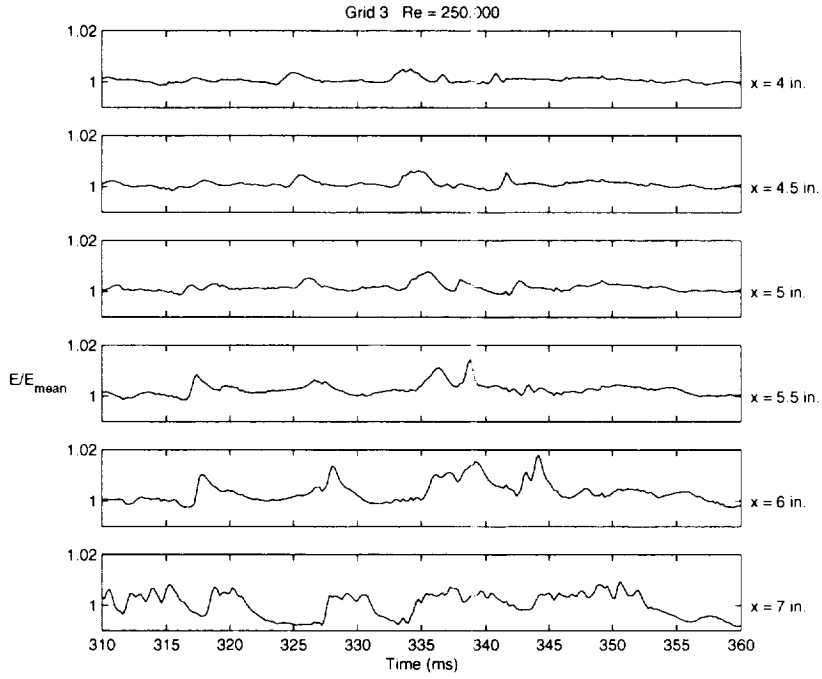

Figure 100 Hot-film gage voltage traces, grid 3, Re = 250,000

G. X-wire Data

Normalized velocity and shear stress profiles from an x-type hot-wire probe are presented in Figures 101-118. Profiles are presented for grids 0, 2 and 3 at Reynolds numbers of 100,000 and 250,000. Downstream profiles only were made with the x-wire.

1. X-wire u′ Velocity Profiles

The streamwise fluctuating velocity profiles for grids 0, 2 and 3 are shown in Figures 101-106. These profiles compare favorably in magnitude and shape with those obtained from the single wire probe. Figure 101 is the x-wire streamwise fluctuating velocity profile for grid 0 and a Reynolds number of 100,000. The low rms values obtained for profiles at x=5.25 and 5.75 inches (13.34 and 14.61 cm) for grid 0 occur within the separated flow region and are indicative of values that would occur in a

separated flow. As the flow undergoes transition the rms values increase in magnitude as the flow progresses downstream. The behavior of this x-wire profile is similar to that of the single wire probe profile in that the peak u′ value occurs at a y/δ^* value of approximately 1.0 for all axial locations tested; however, the magnitude of the x-wire peak rms values are slightly lower than those of the single wire. The peak rms value increases in magnitude as the flow proceeds downstream, reaching a maximum value of approximately 0.158 between x=6.75 and 7.25 inches (17.15 and 18.42 cm) which corresponds to the approximate location of transition onset that was obtained from the intermittency profiles. The peak rms value decreases in magnitude as the flow passes through transition, finally decreasing to a value of approximately 0.1 at the last measurement station (x=9.25 inches, 23.50 cm). Additionally, all of the u′ profiles collapse on top of each other as the flow proceeds downstream and approaches a u'/U_e value of approximately 0.01. The behavior of the u′ profiles described above is repeated for grids 2 and 3, at a Reynolds number of 100,000 in Figures 102 and 103 with peak rms values occurring at axial locations of x=6.25 and x=5.75 inches (15.88 and 14.61 cm) for grids 2 and 3 respectively. These values correspond to the approximate locations of transition onset and are also consistent with transition onset values obtained from the intermittency profiles.

Figures 104-106 show the x-wire rms profiles for grids 0, 2 and 3 and at a Reynolds number of 250,000. These rms profiles are also consistent with the single wire rms profiles except that the x-wire peak rms values are again slightly lower than the single wire values. Peak rms values occur again at a y/δ^* value of approximately 1 with

a maximum occurring at approximate u'/U_e values of 0.115 at x=8.25 inches (20.96 cm) for 0, 0.12 at x=7.75 inches (19.69 cm) for grid 2 and 0.11 at 6.75 inches (17.15 cm) for grid 3, respectively. However, the rms profiles for this Reynolds number differs from those for a Reynolds number of 100,000 in that these rms profiles do not collapse on top of each other as the flow progresses downstream. Instead of collapsing to a single value as the flow progresses downstream, the rms levels steadily increase, which can be attributed to the merging of boundary layers from the lower (test plate) and upper wall. The deviation is more pronounced at downstream measurement stations x=7.25-9.25 inches (18.42-23.50 cm) for all levels of turbulence intensities tested and this behavior was also seen in the single wire data.

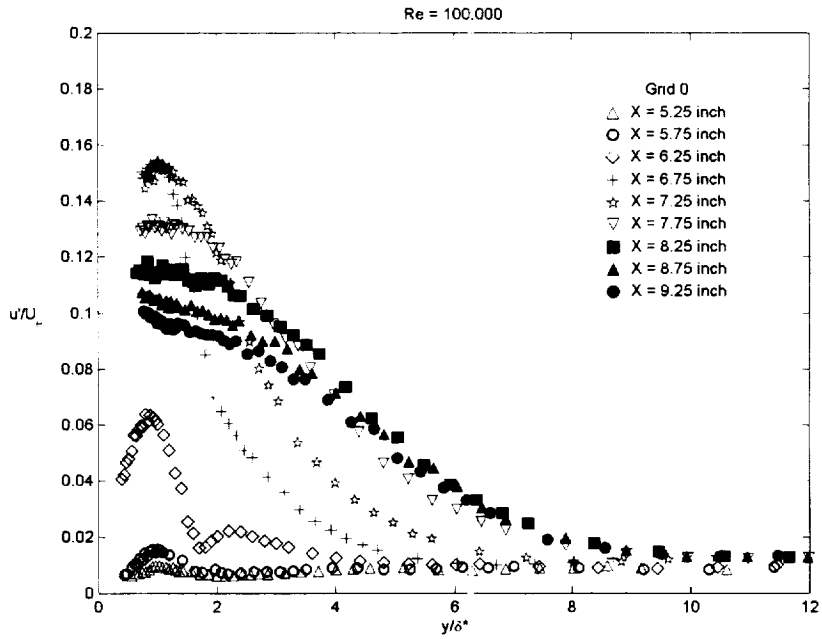

Figure 101 X-wire u′ velocity prcfile, grid 0, Re = 100,000

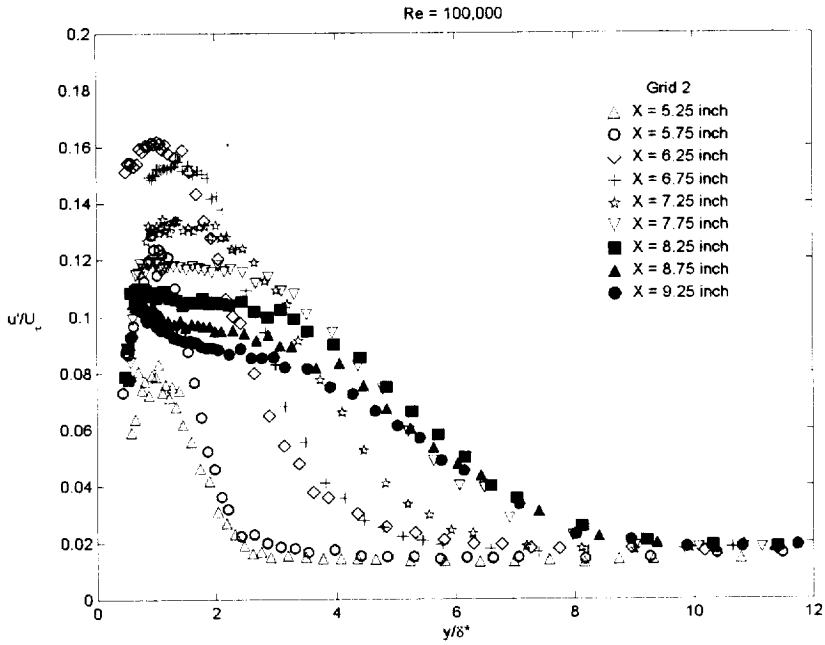

Figure 102 X-wire u′ velocity profile, grid 2, Re = 100,000

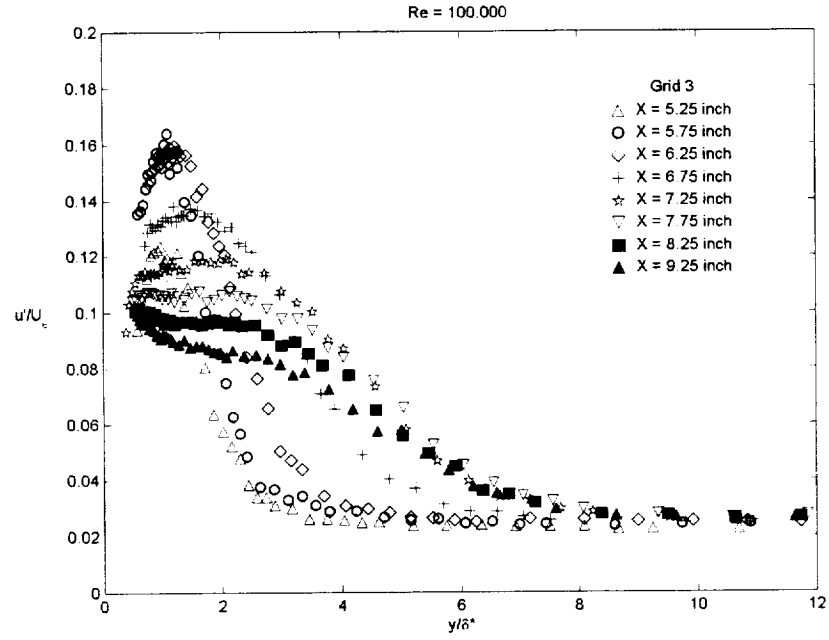

Figure 103 X-wire u′ velocity profile, grid 3, Re = 100,000

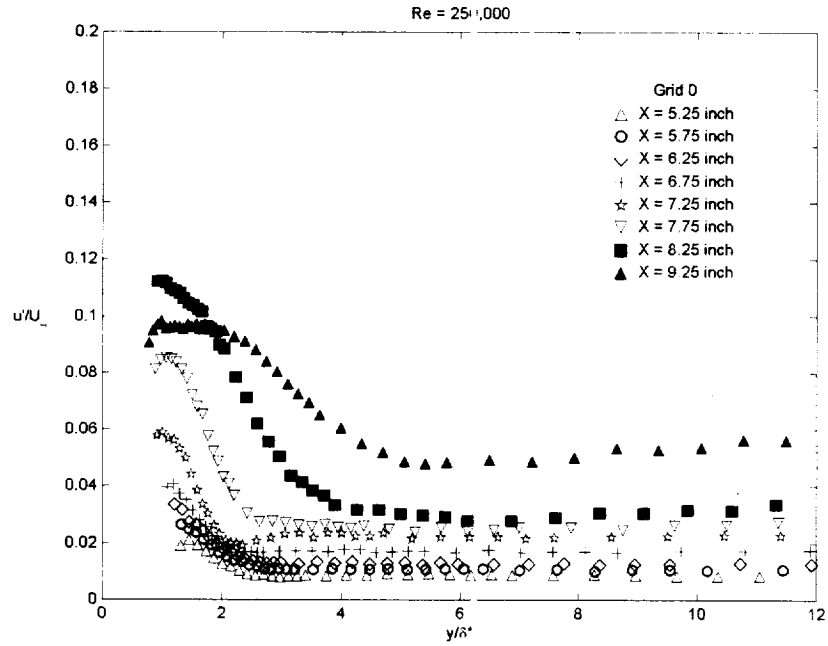

Figure 104 X-wire u′ velocity profile, grid 0, Re = 250,000

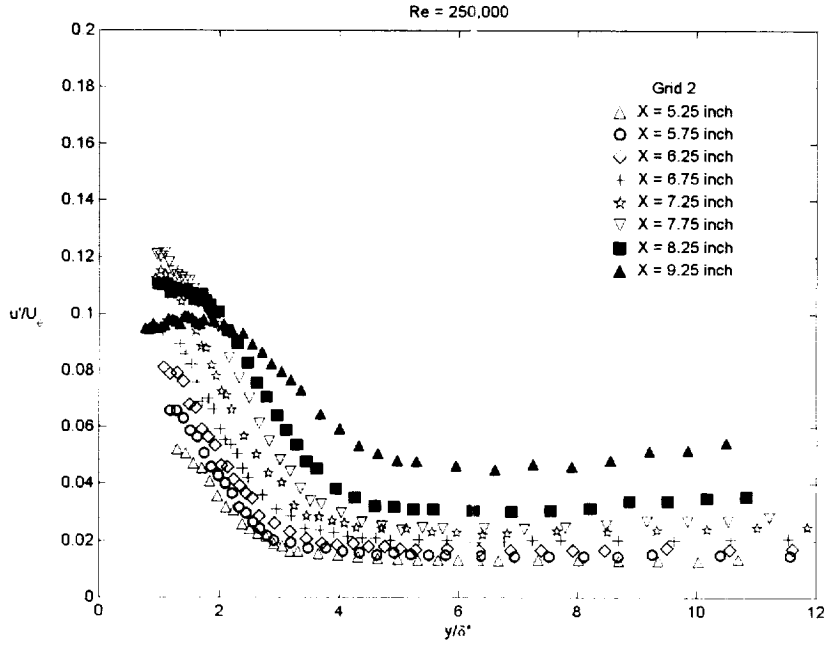

Figure 105 X-wire u′ velocity profile, grid 2, Re = 250,000

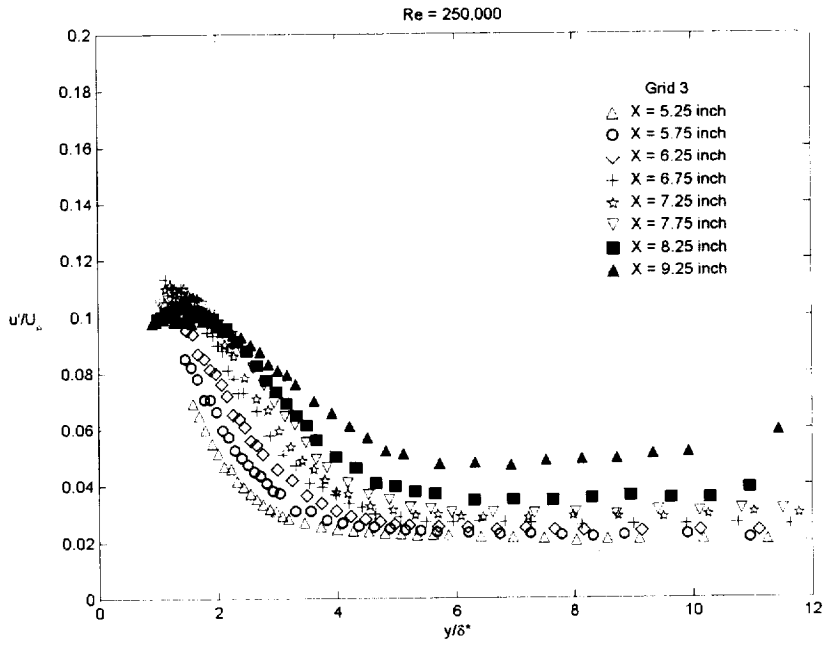

Figure 106 X-wire u′ velocity profile, grid 3, Re = 250,000

2. X-wire v′ Velocity Profiles

The x-wire vertical or v′ velocity profiles are presented in Figures 107-112 for grids 0, 2 and 3 and Reynolds numbers of 100,000 and 250,000.

The profiles for grids 0, 2 and 3 and a Reynolds number of 100,000 are shown in Figures 107-109 and these profiles exhibit behavior that is similar to the u′ rms velocity profiles. Figure 107 is the v′ plot for grid 0 and it shows that maximum values of v′ occur closer to the wall than the u′ rms velocity profiles and these values increase and move away from the wall as the flow proceeds downstream. A maximum v′ value occurs for grid 0 at x=6.75 inches (17.15 cm) and a v'/U_e value of approximately 0.125 and a y/δ^* value of approximately 1.5 and this contrasts with the maximum u'/U_e value of approximately 0.16 occurring at x= 7.25 inches (18.42 cm) and a y/δ^* value of approximately 1.0. The location of the maximum v′ value corresponds to the

approximate location of transition onset for grid 0. The levels of v'/U_e for grid 0 gradually decrease after transition onset finally leveling off to a value of approximately 0.01. The v′ plot for grid 2 is shown in Figure 108 and it shows that v′ levels have increased close to the wall due to the increase in freestream turbulence level. Again, the v′ levels of the upstream profiles occur near the wall and move away from the wall as the flow moves downstream with a maximum occurring between x=6.25 and 6.75 inches (15.88-17.14 cm, approximate location of transition onset) with a v'/U_e value of approximately 0.12 and an approximate y/δ^* value of 2. The v′ levels then decrease gradually and level off to a value of approximately 0.22. The v′ levels for grid 3 in Figure 109 increase in a fashion similar to those for grid 2 with increased v′ levels for the upstream profiles due to the higher freestream turbulence level. A maximum v′ occurs at x=6.25 inches (15.88 cm) with a v'/U_e value of approximately 0.12 and an approximate y/δ^* value of 1.2.

Figures 110-112 contain the v′ profile plots for a Reynolds number of 250,000 and these maximum v′ values tend to occur at an approximate value y/δ^* of 1.0 for grids 0, 2 and 3. Maximum v′ values of approximately 0.082, 0.097 and 0.090 occur at x=8.25, x=7.75 and 6.75 inches (20.96, 19.69 and 17.15 cm) for grids 0, 2 and 3, respectively.

The behavior of u′ and v′ in the transitional boundary layer can also be an indication of the distribution of turbulent kinetic energy in a steady shear flow (Tennekes & Lumley, 1972). More energy is transferred to the u′ velocity component than the other components because it receives all of the kinetic energy production generated by the mean flow. The transfer of turbulent kinetic energy to the other components is then

performed by the nonlinear pressure-velocity interaction, $\overline{p'\partial u_i' / \partial x_i}$. In the early stages of transition when the eddies are relatively large due to the production of turbulent kinetic energy, the energy accumulates first in the u′ velocity component with the remaining energy being transferred to the other components. Because of this process the u′and v′ velocity components increase in energy resulting in an attendant increase in their rms levels. As transition continues, the size and strength of the eddies decrease, resulting in an increase in viscous dissipation until it is globally balanced with the energy production. Some portions of the energy are redistributed to other velocity components which decreases the energy in the u′ velocity component and decreases the magnitude of the u′ rms. However, as the energy gained by v′ from the u′ component is being locally balanced with viscous dissipation, the v′ rms level remains close to a constant value in the later stages of transitional flow. A similar energy level is attained by both the u′and v′ velocity components near the edge of the boundary layer, indicating that isotropy of the turbulent fluctuations near the edge of the boundary layer is almost completed in the late stages of transitional flow.

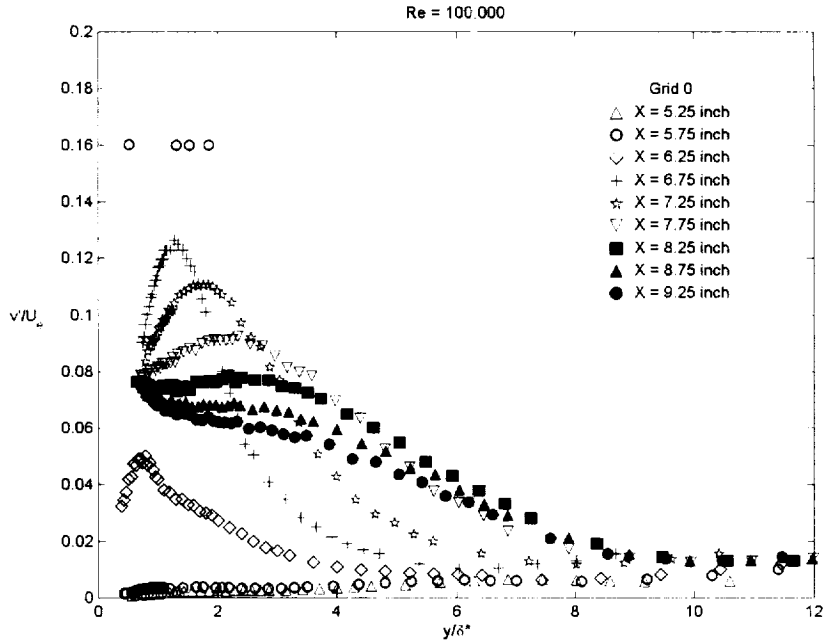

Figure 107 X-wire v′ velocity profile, grid 0, Re = 100,000

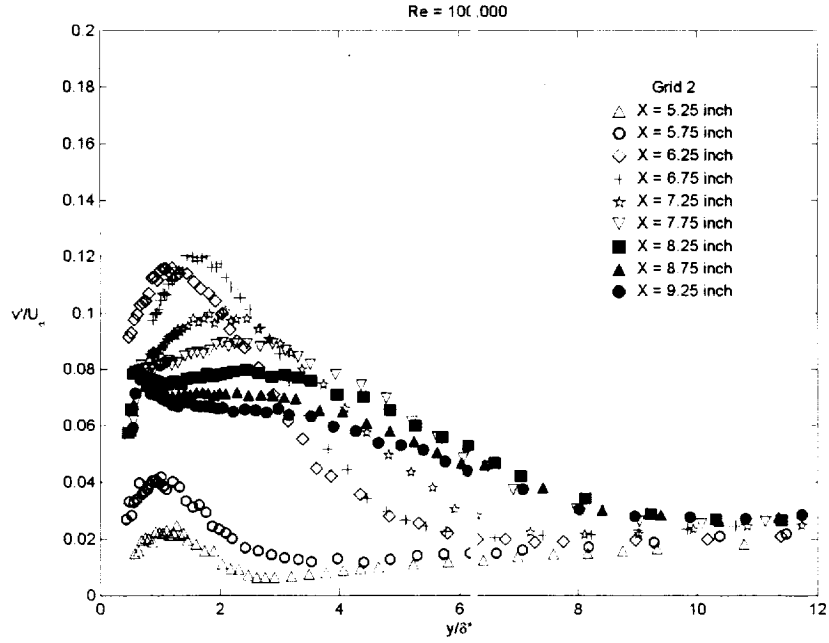

Figure 108 X-wire v′ velocity prc file, grid 2, Re = 100,000

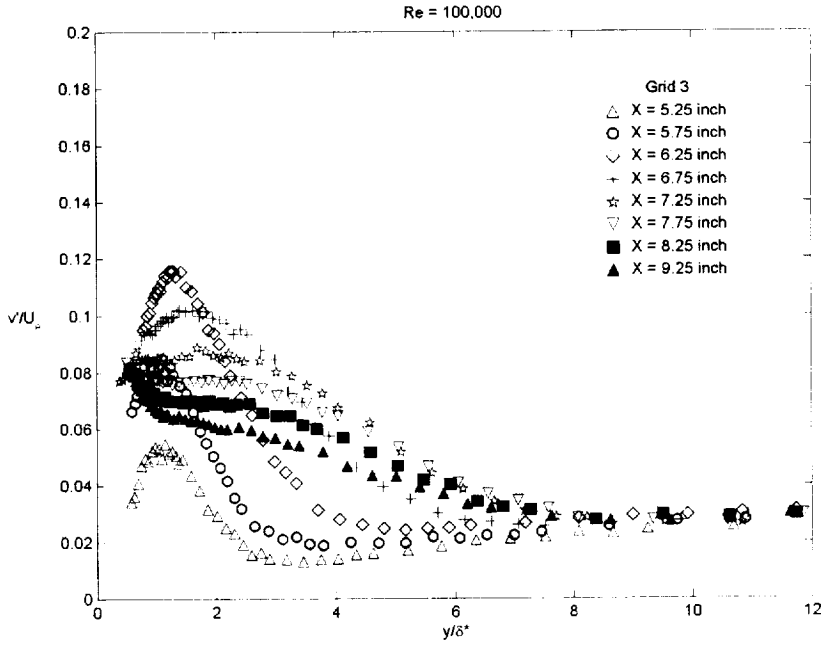

Figure 109 X-wire v′ velocity profile, grid 3, Re = 100,000

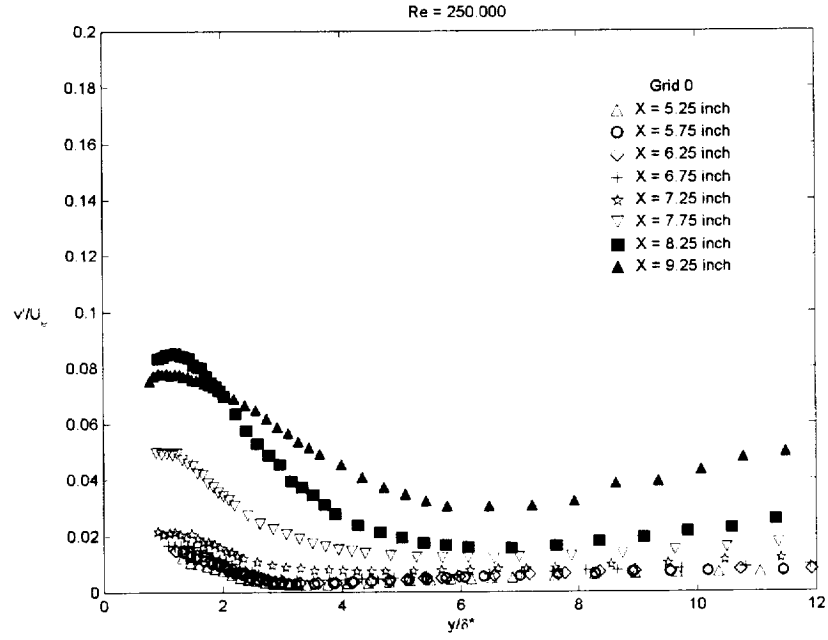

Figure 110 X-wire v′ velocity profile, grid 0, Re = 250,000

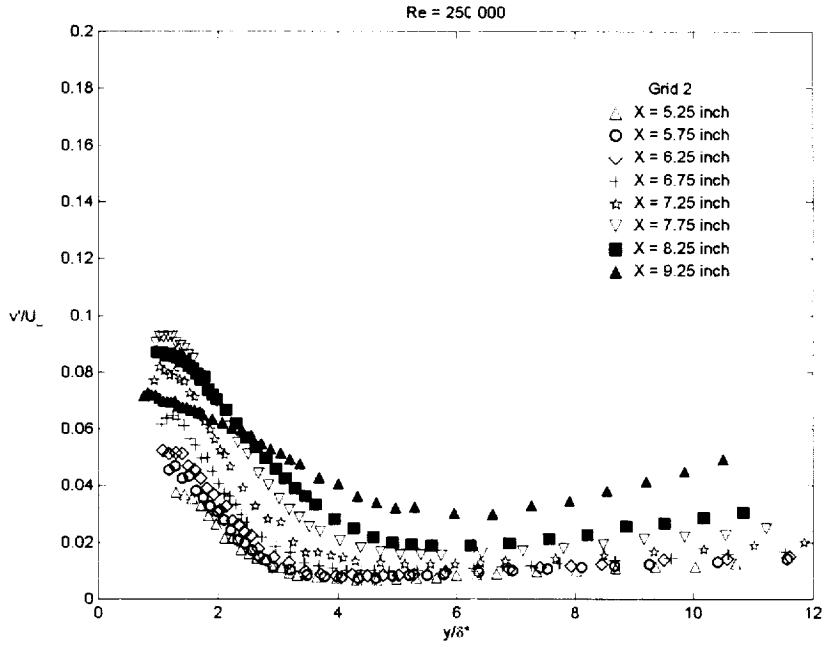

Figure 111 X-wire v′ velocity profile, grid 2, Re = 250,000

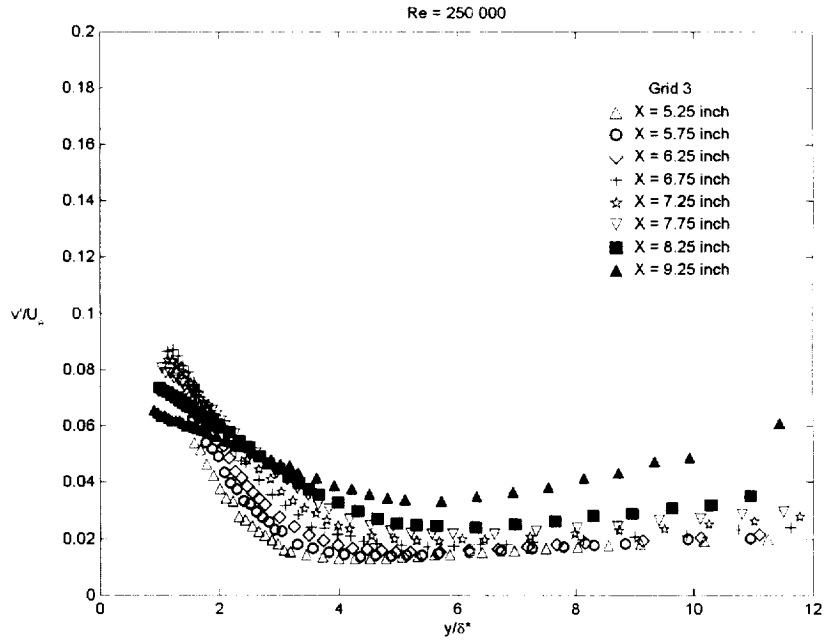

Figure 112 X-wire v′ velocity profile, grid 3, Re = 250,000

3. Reynolds Shear Stress Profiles

Reynolds shear stress profiles for Reynolds numbers of 100,000 and 250,000 for grids 0, 2 and 3 were computed from the digitally recorded instantaneous x-wire probe measurements and are shown in Figures 113-118. These profiles were normalized with respect to the square of the edge velocity.

Figure 113 is the Reynolds shear stress profile for grid 0 and a Reynolds number of 100,000. Profiles at axial locations of 5.25 and 5.75 inches (13.34 and 14.61 cm) (which are inside the separation bubble) are zero near the wall because the production of turbulent kinetic energy is ideally zero in the region. As transition begins to occur around an axial station of 6.25 inches (15.88 cm), production of turbulent kinetic energy is initiated and the Reynolds shear stress attains a peak value of approximately 0.002 at this location. As transition proceeds more turbulent kinetic energy is produced and a maximum value of approximately 0.0078 occurs at a y/δ^* value of approximately 1.0 and an axial location of 6.75 inches (17.15 cm). The levels of the Reynolds shear stress then decrease as transition is completed and turbulent flow is achieved, finally leveling off to zero near the edge of the boundary layer. The Reynolds shear stress profiles for grids 2 and 3 behave similarly to the grid 0 profile except the profiles at x=5.25 and 5.75 inches (13.34 and 14.61 cm) are not zero inside the boundary layer and a higher maximum value is achieved, as shown in Figures 114 and 115. The effect of the freestream turbulence can be clearly seen in these figures as the level of the Reynolds shear stress has increased significantly in the near wall region for x=5.25 and 5.75 inches (13.34 and 14.61 cm). The adverse pressure gradient experienced by the flow increases the rate of turbulent

shear stress production in the transition region and this phenomena was also seen experimentally by Mislevy and Wang (1995). Approximate locations of transition deduced from these shear stress distributions agree quite well with those deduced from the intermittency data.

The Reynolds shear stress plots for a Reynolds number of 250,000 and grids 0, 2 and 3 are presented in Figures 116-118. At this higher Reynolds number and for grid 0, the entire Reynolds shear stress distribution is approximately zero for axial locations of x=5.25 inches (13.34 cm) to x=7.25 inches (18.42 cm). For grid 0 at this Reynolds number, transition begins at approximately 7.25 inches (18.42 cm) according to the intermittency profiles. It can be seen in Figure 116 that turbulent shear stress production also begins approximately at this axial location. After transition is initiated, the grid 0 Reynolds shear stress profiles behave similar to the profiles at a Reynolds number of 100,000 except the magnitude is smaller. A maximum shear stress value of 0.0035 occurs at a y/δ^* value of approximately 1.0 and an axial location of x=8.25 inches (20.96 cm). Additionally, the profiles for this Reynolds number condition do not exhibit the same drop in magnitude as the profiles did for a Reynolds number of 100,000 because fully turbulent flow is not achieved. The Reynolds shear stress profile for x=9.25 inches (23.50 cm) drops below zero and this is mostly attributed to the merging of the lower and upper wall boundary layers near the end of the test section.

Figure 117 is plot of the Reynolds shear stress distribution for grid 2 and a Reynolds number of 250,000. The behavior of the shear stress profile for grid 2 is similar to that of grid 0 except that only the profile at x=5.25 inches (13.34 cm) is zero

for the entire profile and the profiles for the other axial locations have moved up due to an increased level of freestream turbulence. After transition is initiated, at approximately x=6.75 inches (17.15 cm), the grid 2 profiles move upward towards the maximum value of 0.0035 which occurs at a y/δ^* value of approximately 1.0 and an axial location of x=8.25 inches (20.96 cm). The flow is almost fully turbulent at this axial station and the shear stress production starts to decrease from x=9.25 inches (23.50 cm) since the flow is fully turbulent at this location. Additionally, the Reynolds shear stress profile for x=9.25 inches (23.50 cm) again drops below zero and this is due to the merging of the lower and upper wall boundary layers near the end of the test section. The behavior of the grid 2 shear stress profile is repeated for grid 3, as shown in Figure 118, except the maximum shear stress value of 0.0031 occurs at x=7.75 inches (19.69 cm) and a y/δ^* value of approximately 1.2. After transition is initiated, at approximately x=6.25 inches (19.69 cm), the grid 2 profiles move upward towards the maximum value and then decrease as the shear stress production starts to decrease at x=8.25 inches (20.96 cm) after fully turbulent flow is attained.

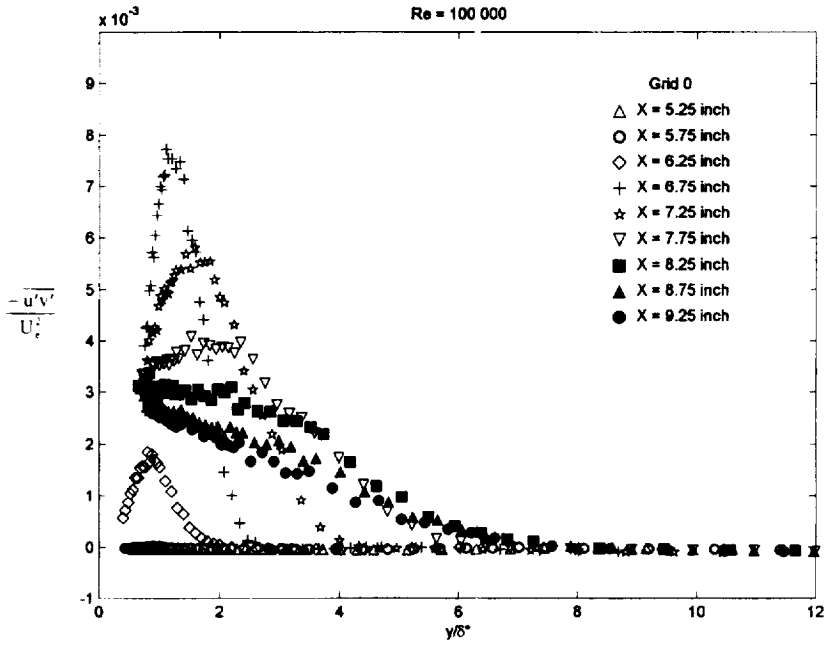

Figure 113 Reynolds shear stress profiles, grid 0, Re = 100,000

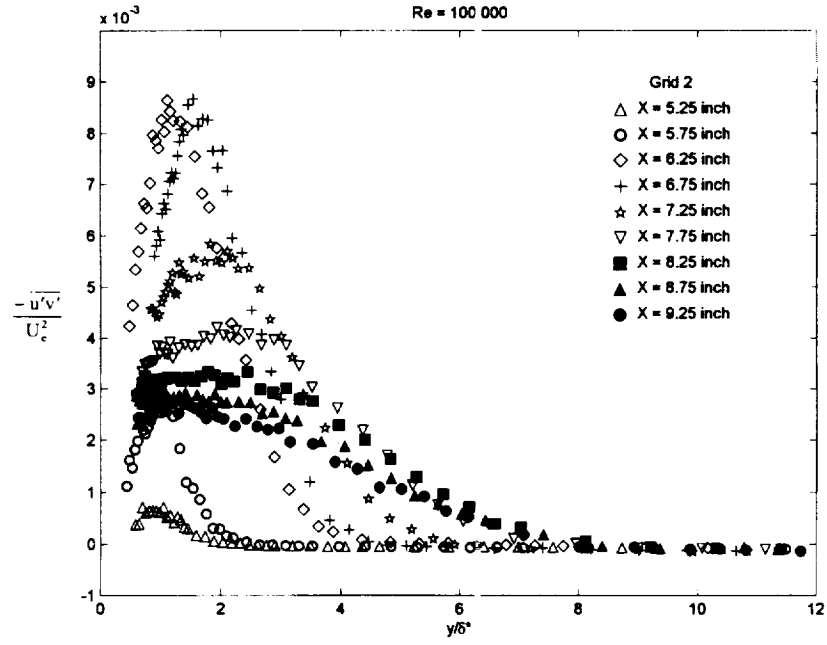

Figure 114 Reynolds shear stress profiles, grid 2, Re = 100,000

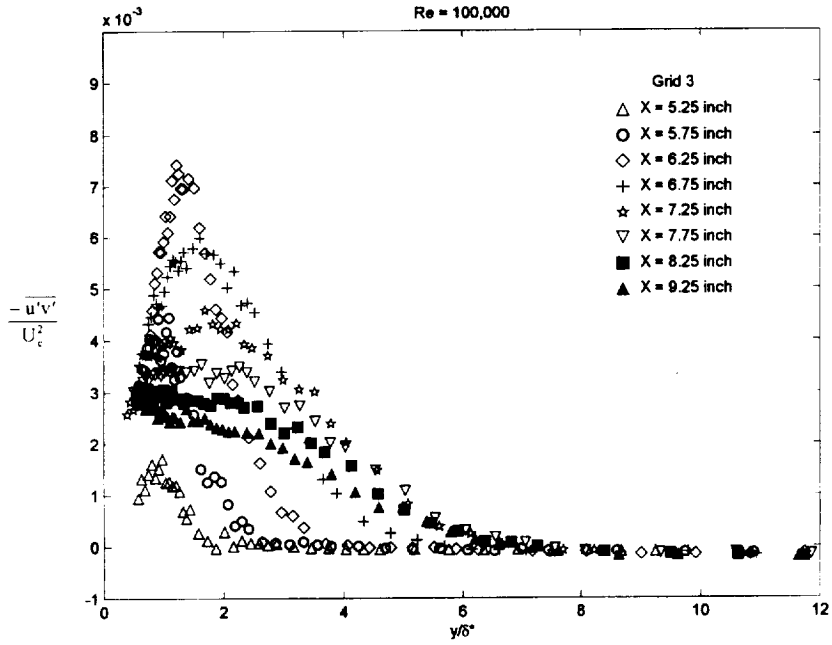

Figure 115 Reynolds shear stress profiles, grid 3, Re = 100,000

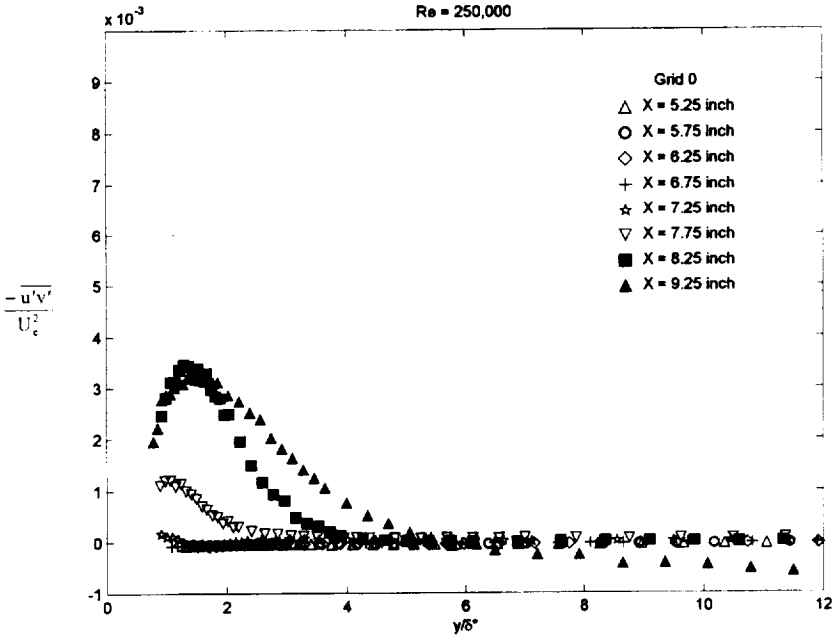

Figure 116 Reynolds shear stress profiles, grid 0, Re = 250,000

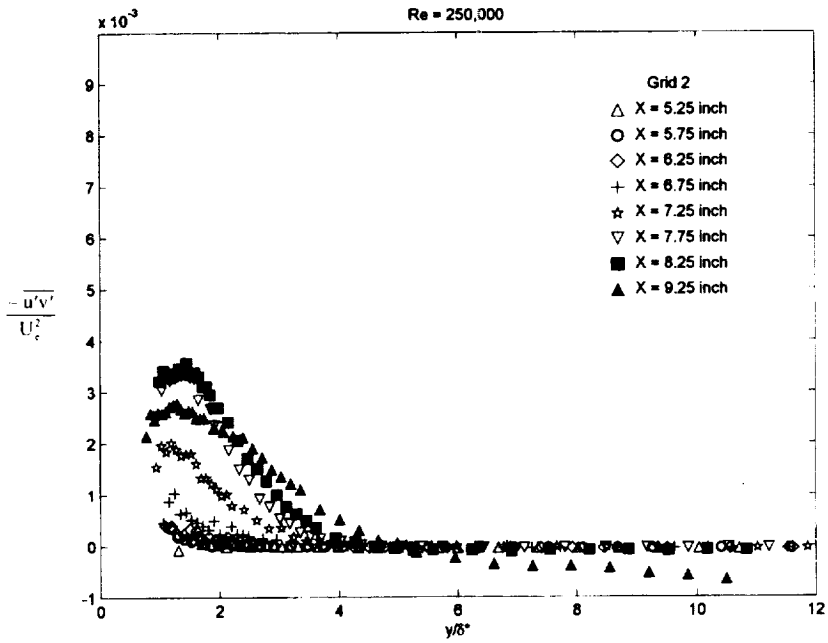

Figure 117 Reynolds shear stress profiles, grid 2, Re = 250,000

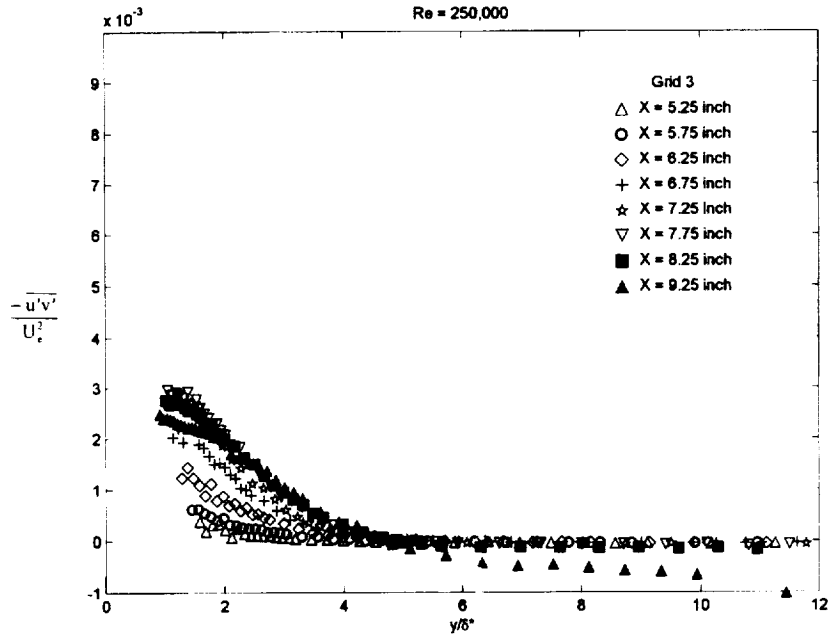

Figure 118 Reynolds shear stress profiles, grid 3, Re = 250,000

VI. UNCERTAINTY ANALYSIS

An uncertainty analysis was performed on the hot-wire data using the methods of Yavuzkurt (1984). Yavuzkurt derived the following equations for computing the uncertainty in velocities obtained from hot-wire calibration data, with the following assumptions: a constant temperature anemometer, an isothermal flow with no velocity fluctuations, and velocity is measured with a pitot tube probe connected to a micromanometer. The anemometer output E (in volts) and the micromanometer reading h (in inches of oil) are recorded. The flow velocity u can be calculated from h and will be called u_1 with an uncertainty called Δu_1. For

$$u_1 \neq \Delta u_1, \tag{1}$$

$$u_1 = \left(\frac{2hpgRT_\infty}{P_S} \right)^{1/2} \tag{2}$$

where g and R are constants with negligible uncertainties. The uncertainties in the quantities in Equation (2) can represented by the following relations:

$h \pm \Delta h$, $\rho \pm \Delta \rho$, $T_\infty \pm \Delta T_\infty$, $P_S \pm \Delta P_S$. Utilizing methods from Kline and McClintock (1953) and Holman (1978), the uncertainty Δu_1 can be represented by the following equation:

$$\Delta u_1 = \left[\left(\frac{\partial u_1}{\partial h} \Delta h \right)^2 + \left(\frac{\partial u_1}{\partial \rho} \Delta \rho \right)^2 + \left(\frac{\partial u_1}{\partial T_\infty} \Delta T_\infty \right)^2 + \left(\frac{\partial u_1}{\partial P_S} \Delta P_S \right)^2 \right]^{1/2}$$

Rearranging yields

$$\Delta u_1 = \frac{1}{2} u_1 \left[\left(\frac{\Delta h}{h} \right)^2 + \left(\frac{\Delta \rho}{\rho} \right)^2 + \left(\frac{\Delta T_\infty}{T_\infty} \right)^2 + \left(\frac{\Delta P_S}{P_S} \right)^2 \right]^{1/2} \qquad (3)$$

Instantaneous velocity data measured with the calibration process yields an effective velocity of u_{eff} and will have an uncertainty of

$$\Delta u_{eff} = \left[\left(\Delta u_1 \right)^2 + \left(\Delta u_2 \right)^2 \right]^{1/2}$$

Defining α from equation (3), leads to

$$\alpha = \frac{\Delta u_1}{u_1} = \frac{1}{2} \left[\left(\frac{\Delta h}{h} \right)^2 + \left(\frac{\Delta \rho}{\rho} \right)^2 + \left(\frac{\Delta T_\infty}{T_\infty} \right)^2 + \left(\frac{\Delta P_S}{P_S} \right)^2 \right]^{1/2}$$

Replacing $\frac{\Delta h}{h}$ with $\frac{\Delta P}{P}$, the relative uncertainty of the total pressure (since a pressure transducer was used instead of a manometer board) yields

$$\frac{\Delta u_1}{u_1} = \alpha = \frac{1}{2} \left[\left(\frac{\Delta P}{P} \right)^2 + \left(\frac{\Delta \rho}{\rho} \right)^2 + \left(\frac{\Delta T_\infty}{T_\infty} \right)^2 + \left(\frac{\Delta P_S}{P_S} \right)^2 \right]^{1/2} .$$

$$\Delta u_1 = \alpha u_{eff}$$

$$\Delta u_2 = \beta u_{eff}$$

The quantity β can be calculated from the curve fit data as follows:

$$\beta = \left[\frac{\sum_{i=1}^{n} \left(\frac{\Delta u_2}{u_{eff}} \right)_i^2}{n} \right]^{1/2} ,$$

Hence,

$$\Delta u_{eff} = u_{eff}\left(\alpha^2 + \beta^2\right)^{1/2}.$$

Using data obtained from the Dantec Streamline calibration flow unit:

n	U volts	E m/s*	T °C*	P kPa *	Ecorr volts	Ucorr m/s*
1	0.49467	1.17238	28.50794	98.30303	1.19079	0.49422
2	2.29737	1.35147	28.51239	98.30578	1.37271	2.31376
3	4.11157	1.44054	28.51114	98.30578	1.46316	4.08173
4	5.84837	1.50359	28.51154	98.30303	1.52721	5.80823
5	7.85840	1.56446	28.51346	98.30578	1.58904	7.91243
6	9.53361	1.60475	28.51715	98.30303	1.62998	9.56792
7	11.30462	1.64031	28.51755	98.30028	1.66610	11.21661
8	13.01815	1.67677	28.51483	98.30028	1.70312	13.10108
9	14.87473	1.70712	28.51111	98.29753	1.73394	14.82722
10	16.59053	1.73726	28.50449	98.30028	1.76452	16.68931
11	18.39380	1.76471	28.49442	98.29753	1.79236	18.51782
12	20.14946	1.78649	28.47153	98.29203	1.81439	20.05871
13	22.29227	1.81498	28.42935	98.30303	1.84314	22.19776
14	24.00756	1.83672	28.37830	98.30028	1.86500	23.92433
15	25.44061	1.85401	28.31592	98.29753	1.88228	25.35272
16	27.47637	1.87891	28.24036	98.30303	1.90723	27.51473
17	29.46212	1.90105	28.15704	98.29753	1.92934	29.53252
18	31.73464	1.92494	28.06400	98.29753	1.95316	31.81570
19	32.75958	1.93401	27.99271	98.30303	1.96204	32.69641
20	34.53765	1.95238	27.90659	98.30028	1.98029	34.55689

***Note:** 1 m/s = 3.281 ft/sec, °C = 5/9 (°F +40)-40, 1 kPa= 1.450×10^{-4} psi.

Using data point 7 to calculate the density and its associated error,

P = 98.300278 kPa, $\Delta P = \pm 0.05$ kPa,
T= 28.517548 °C, $\Delta T = \pm 0.3$ °C,
V= 11.216614 m/s (calibration free jet set point)
ρ= 1.13539 kg/m^3, $\Delta\rho$= 0.01052 kg/ m^3
P_S= 98.25221 kPa, $\Delta P_S = \pm 0.05$ kPa

The error in computing the density is determined from the following equations,

$$\rho = \frac{P}{RT}$$

$$\rho = f(P, T)$$

$$w_R = \left[\left(\frac{\partial R}{\partial x_1} w_1 \right)^2 + \left(\frac{\partial R}{\partial x_2} w_2 \right)^2 + \ \ldots \ + \left(\frac{\partial R}{\partial x_n} w_n \right)^2 \right]^{1/2}$$

$$\frac{\partial \rho}{\partial P} = \frac{1}{RT} \ ,$$

$$\frac{\partial \rho}{\partial T} = \frac{-P}{RT^2} \ ,$$

yielding

$$\frac{w_\rho}{\rho} = \left[\left(\frac{w_P}{P} \right)^2 + \left(\frac{-w_T}{T} \right)^2 \right]^{1/2}$$

Substituting in for P, w_P, T and w_T yields

$$\Delta\rho = \pm 0.01052 \ kg/m^3.$$

Computing the quantity α using P, ΔP, ρ, $\Delta\rho$, T_∞, ΔT_∞, P_S, ΔP_S, gives

$$\alpha = 0.01404.$$

Computing the quantity β using P, ΔP, ρ, $\Delta\rho$, T_∞, ΔT_∞, P_S, ΔP_S, yields

$$\beta = 0.0049217.$$

Computing

$$\frac{\Delta \overline{U}_{eff}}{\overline{U}_{eff}} = \frac{\Delta\left(\overline{u'^2_{eff}}\right)^{1/2}}{\left(\overline{u'^2_{eff}}\right)^{1/2}} = \left(\alpha^2 + \beta^2\right)^{1/2}$$

yields

$$\left(\alpha^2 + \beta^2\right)^{1/2} = 0.014499 \text{ or } 1.4499\ \%.$$

Therefore, the error in the mean and rms velocities from the calibration is 1.4499%.

VII. CONCLUSIONS AND RECOMMENDATIONS

The parametric investigation of the flow field on a simulated LPT blade was performed at three levels of freestream turbulence for Reynolds numbers of 100,000 and 250,000. The flow visualization data confirmed that the boundary layer was separated and formed a bubble. Based on a two parameter bubble bursting criterion proposed by Gaster (1969), the bubbles formed in this experiments were of the short, non-bursting type.

Flow visualization photographs revealed that the laminar portion of the bubble is steady, while the regions downstream from transition are unsteady. The transition process over the separated flow region for a Reynolds number of 100,000 is similar to a laminar free shear layer through the formation of a large coherent eddy structure. However, the transition path for an attached boundary layer at a Reynolds number of 250,000 is through the formation of intermittent turbulent spots. These two distinct transition mechanisms were confirmed by a series of instantaneous hot-film signals. The pressure distribution shows a typical feature, namely a nearly constant pressure zone followed by a sharp pressure rise region. Intermittency profiles showed that shear flow transition (Reynolds number of 100,000) is initiated at approximately x=6.25 inches (15.88 cm) for grid 0, at approximately x=5.75 inches (14.61 cm) for grid 2 and before x=5.75 inches (14.61 cm) for grid 3. Additionally, the intermittency profiles revealed that fully turbulent flow occurs approximately at x=7.25-7.75 inches (18.42-19.69 cm) for

grid 0, at x=6.75 inches (17.15 cm) for grid 2, and between x=6.25-6.75 inches (15.88-17.15 cm) for grid 3. For a Reynolds number of 250,000, the intermittency profiles show that transition is initiated between x=5.75 and 6.25 inches (14.61 and 15.88 cm) for grid 0, between x=6.25 and 6.75 inches (15.88 and 17.15 cm) for grid 2 and before x=5.75 inches (14.61 cm) for grid 3. Additionally, the intermittency profiles revealed that fully turbulent flow does not occur for grid 0, but it does occurs at between x=8.25 and 9.25 inches (20.96 and 23.50 cm) for grid 2 and between x=7.75 and 8.25 inches (19.69 and 20.96 cm) for grid 3.

The transition onset location and length are inversely proportional to the freestream turbulence level. Additionally, the characteristics of transition deduced from the intermittency profiles and boundary layer spectra data show excellent agreement. The modified Roberts' transition length correlation predicts quite well the transition length of the bubble for each condition. It was also observed that bubble length and height decreased as freestream turbulence level increased.

Power spectral density (PSD) profiles showed that almost all of the fluctuating energy is confined in low frequencies less than 700 Hz. This data also shows that the flow field was contaminated by main and bleed blower noise and their sub-harmonics. A two-order of PSD magnitude jump occurs at x=5.75 inches (14.61 cm) for low frequencies less than 1200 Hz. followed by a larger jump in the spectra for all frequency bands measured at x=6.25-6.75 inches (15.88-17.15 cm). Transition onset is indicated by this small jump and the spectra increases in magnitude as the flow becomes fully turbulent as it moves downstream. The PSD spectra over the separation bubble shows no broad band disturbance hump around 1500 Hz., which would be caused by a Kelvin-

Helmholtz type instability in the flow field. Classical flow instabilities (Kelvin-Hemholtz or Tollmien-Schlichting) and their propagation downstream were not identified in any of the PSD profiles in this experimental study. Additionally, the approximate locations of transition onset and fully turbulent flow deduced from the PSD profiles agree favorably with those deduced from the intermittency profiles and hot-film traces.

It is recommended that future research concentrate on identifying the Reynolds numbers at which the separation bubbles burst for various levels of freestream turbulence. It is also recommended that steady state data be taken in experiments with stationary bars or rods upstream of the test section to analyze the effect of wake shedding on the separation/transition process. This data may lead to a clearer understanding of some of the fundamental physics involved in wakes interacting with a transitional or separated flow. Additionally, fundamental research with a moving wake will also be required to characterize the unsteady effect of the wake on the boundary layer since an unsteady wake occurs in a real engine environment.

VIII. REFERENCES

Anderson, J. D., **Fundamentals of Aerodynamics**, Second Edition, McGraw-Hill, Inc., New York, NY, pp. 711-738, 1991.

Ashworth, D. A., LaGraff, J. E., Schultz, D. L. and Grindod, K. J., "Unsteady Aerodynamic and Heat Transfer Processes in a Transonic Turbine Stage", *Journal of Engineering for Gas Turbines and Power*, Vol. 107, October 1985, pp. 1022-1033.

Baughn, J. W., Butler, R. J., Byerley, A. R. and Rivir, R. B., "An Experimental Investigation of Heat Transfer, Transition and Separation on Turbine Blades at Low Reynolds Number and High Turbulence Intensity", To be published in bound proceedings of the 1995 International Mechanical Engineering Congress and Exposition, June 1995.

Bellhouse, B. J. and Schultz, D. L., "Determination of Mean and Dynamic Skin Friction, Separation and Transition in Low Speed Flow with a Thin-Film Heated Element", *Journal of Fluid Mechanics*, Vol. 24, Part 2, 1966, pp. 379-400.

Binder, A., Schroeder, Th. and Hourmouziadis, J., "Turbulence Measurements in a Multistage Low Pressure Turbine", ASME Paper A88-54207, 1988.

Blaha, R. J., "ESCORT D/D$^+$ Users Manual", NASA Lewis Research Center, 1993.

Blair, M. F. , "Influence of Free-stream Turbulence on Boundary Layer Transition in Favorable Pressure Gradients", *Journal of Engineering for Power*, Vol. 104, October 1982, pp. 743-750.

Blair, M. F., Bailey, D. A. and Schlinker, R. H., "Development of a Large-Scale Wind Tunnel for the Simulation of Turbomachinery Airfoil Boundary Layer", *Journal of Engineering for Power*, Vol. 103, pp. 678-687, 1981.

Chang, P. K., **Separation of Flow**, Pergamon Press, First edition, New York, NY, pp. 36-93, 1970.

Cherry, D. G., Gay, C. H. and Lenahan, D. T., "Energy Efficient Engine Low Pressure Turbine Test Hardware Detailed Design Report", NASA CR-167956, 1982.

Clauser, F. H., "The Turbulent Boundary layer", *Advances in Applied Mechanics*, Vol. IV, 1956, Academic Press, New York, NY, pp. 1-51.

Crawford, M. E. and Keys, W. M., "Program for Computing Boundary Layer in Turbomachinery and Compressors", NASA CR-11111, April 1987.

Cumpsty, N. A., Dong, Y., and Li, Y. S., "Compressor Blade Boundary Layers in the Presence of Wakes", ASME 95-GT-1111, June 1995.

Dantec Measurement Technology A/S, "Streamline Installation & User's Guide", 1994, Publication No. 9150A9406, First edition, Skovlunde, Denmark.

Davis, R. L. Cater, J. E. and Reshotko, E., "Analysis of Transitional Separation Bubbles on Infinite Swept Wings", AIAA Paper No. AIAA-85-1685, 1985.

Dixon, S. L., **Fluid Mechanics, Thermodynamics of Turbomachinery**, Pergamon Press, Third edition, New York, NY, 1978.

Gardner, W. B., "Energy Efficient Engine Low Pressure Turbine Boundary Layer Program Technology Report", NASA CR-165338, 1981.

Gaster, M., "The Structure and Behavior of Separation Bubbles", NPL Reports and Memoranda, No. 3595, 1969.

Gostelow, J. P., Blunden, A. R. and Walker, G. J., "Effects of Free-stream Turbulence and Adverse Pressure Gradients on Boundary Layer Transition", ASME 92-GT-380, June 1992.

Glassman, A .J. (editor), "Turbine Design and Application", NASA SP-290, Vols. 1-3, 1972.

Gostelow, J. P. and Walker, G. J., "Effects of Pressure Gradients on the Nature and Length of Boundary Layer Transition", *Journal of Turbomachinery*, Vol. 112, April 1990.

Hall, D. J. and Gibbings, J. C., "Influence of Stream Turbulence and Pressure Gradient Upon Boundary Layer Transition", *Journal of Mechanical Engineering*, 1972, Vol. 14, No. 2, pp. 134-146.

Halstead, D. E., Wisler, D. C., Okishi, T. H., "Boundary Layer Development in an Embedded Turbine Stage", ASME 95-GT-1122, June 1995.

Halstead, D. E., Wisler, D. C., Okishi, T. H., Walker, G. J., Hodson, H. P., Shin, H. W., "Boundary Layer Development in Axial Compressors and Turbines, Part 1 of 4: Composite Picture", ASME 95-GT-461, June 1995.

Halstead, D. E., Wisler, D. C., Okishi, T. H., Walker, G. J., Hodson, H. P., Shin, H. W., "Boundary Layer Development in Axial Compressors and Turbines, Part 2 of 4: Compressors", ASME 95-GT-462, June 1995.

Halstead, D. E., Wisler, D. C., Okishi, T. H., Walker, G. J., Hodson, H. P., Shin, H. W., "Boundary Layer Development in Axial Compressors and Turbines, Part 3 of 4: LP Turbines", ASME 95-GT-463, June 1995.

Halstead, D. E., Wisler, D. C., Okishi, T. H., Walker, G. J., Hodson, H. P., Shin, H. W., "Boundary Layer Development in Axial Compressors and Turbines, Part 4 of 4: Computations & Analyses", ASME 95-GT-464, June 1995.

Hedley, T. B. and Keffer, J. F., "Turbulent/Non-Turbulent Decisions in an Intermittent Flow", *Journal of Fluid Mechanics*, 1974, Vol. 64, pp. 625-644.

Hodson, H. P., Huntsman, I. and Steele, A. B., "An Investigation of Boundary Layer Development in a Multistage LPT", ASME Paper 93-GT-310, May 1993.

Holman, J. P., **Experimental Methods for Engineers**, McGraw-Hill Inc., Third edition, New York, NY, pp. 252-253., 1978.

Horton, H. P., "A Semi-Empirical Theory for the Growth and Bursting of Laminar Separation Bubbles", Aeronautical Research Council, CP-1073, 1968.

Klebanoff, P. S., "Characteristics of Turbulence in a Boundary Layer with Zero Pressure Gradient", NACA Rep. No. 1247, 1955.

Kline, S. J., and McClintock, F. A., "Describing Uncertainties in Single-sample Experiments", *Mechanical Engineering*, p. 3, January 1953.

Lomas, C. G., **Fundamentals of Hot-Wire Anemometry**, Cambridge University Press, New York, 1986.

Malkiel, E. and Mayle, R. E., "Transition in a Separation Bubble", ASME 95-GT-32, 1995.

Mayle, R. E., "Unsteady, Multimode Transition in Gas Turbine Engines", Keynote Address, Workshop on End-Stage Boundary Layer Transition sponsored by Syracuse University, August 1993.

Mayle, R. E., "The Role of Laminar-Turbulent Transition in Gas Turbine Engines", *Journal of Turbomachinery*, Vol. 113, October 1991, pp. 509-537.

Mayle, R. E., "A Theory for Wake-Induced Transition", ASME Paper No. 89-GT-57, June 1989.

McFarland, E. R., "Solution of Plane Cascade Flow Using Improved Surface Singularity Methods", *Journal of Engineering for Power*, July 1982, Vol. 104, pp. 668-674.

McFarland, E. R., "A Rapid Blade-to-Blade Solution for Use in Turbomachinery Design", *Journal of Engineering for Gas Turbines and Power*, April 1984.

Mislevy, S. P. and Wang, T., "The Effects of Adverse Pressure Gradients on Momentum and Thermal Structures in Transitional Boundary Layers, Part 2 Fluctuation Quantities", ASME Paper No. 95-GT-5, June 1995.

Morin, B. L. and Patrick , W. P., "Detailed Studies of a Large-Scale Laminar Separation Bubble on a Flat Plate, Volume 1, Report No. R91-956786-1, June 1991.

Musker, A.J., "Explicit Expression for the Smooth Wall Velocity Distribution in a Turbulent Boundary Layer," *AIAA Journal*, Vol. 17, No. 6, pp. 655-657, 1979.

Johnson, I. A. and Bullock, R. O. (editors), "Aerodynamic Design of Axial-Flow Compressors", NASA SP-36, 1965.

NPARC Alliance Technical Team, NASA Lewis Research Center and Arnold Engineering Development Center, "A User's Guide to NPARC", Version 2.0, 1994.

O'Meara, M. M. and Mueller, T. J., "Experimental Determination of Laminar Separation Bubble Characteristics of an Airfoil at Low Reynolds Numbers, AIAA-86-1065, 1986.

Perry, A. E., **Hot-wire Anemometry**, Oxford University Press, New York, NY, 1982.

Roberts, W. B., "The Effect of Reynolds Number and Laminar Separation on Axial Cascade Performance", *Journal of Engineering for Power*, pp. 261-274, April 1975.

Roberts, W. B., "Calculation of Laminar Separation Bubbles and Their Effect on Airfoil Performance", *AIAA Journal*, Vol. 18, No. 1, pp. 25-30, April 1980.

Rivir, R. B., "Transition on Turbine Blades and Cascades at Low Reynolds Numbers", AIAA 96-2079, June 1996.

Schlichting, H., **Boundary Layer Theory**, McGraw-Hill Inc., New York, NY, Seventh edition., 1959.

Schulte, V., and Hodson, H. P., "Wake Separation Bubble Interaction in Low Pressure Turbines", AIAA-94-2931, June 1994.

REPORT DOCUMENTATION PAGE

Form Approved
OMB No. 0704-0188

1. AGENCY USE ONLY (*Leave blank*)

2. REPORT DATE
October 1998

3. REPORT TYPE AND DATES COVERED
Technical Memorandum

4. TITLE AND SUBTITLE
Experimental Study of Boundary Layer Behavior in a Simulated Low Pressure Turbine

5. FUNDING NUMBERS
WU–523–26–33–00

6. AUTHOR(S)
Rickey J. Shyne

7. PERFORMING ORGANIZATION NAME(S) AND ADDRESS(ES)
National Aeronautics and Space Administration
Lewis Research Center
Cleveland, Ohio 44135–3191

8. PERFORMING ORGANIZATION REPORT NUMBER
E–11305

9. SPONSORING/MONITORING AGENCY NAME(S) AND ADDRESS(ES)
National Aeronautics and Space Administration
Washington, DC 20546–0001

10. SPONSORING/MONITORING AGENCY REPORT NUMBER
NASA TM—1998-208503

11. SUPPLEMENTARY NOTES
This report was submitted as a dissertation in partial fulfillment for the degree Doctor of Philosophy to the University of Toledo, May 1998. Responsible person, Rickey J. Shyne, organization code 5820, (216) 433–3595.

12a. DISTRIBUTION/AVAILABILITY STATEMENT
Unclassified - Unlimited
Subject Categories: 02, 07, and 34 Distribution: Nonstandard
This publication is available from the NASA Center for AeroSpace Information, (301) 621–0390.

12b. DISTRIBUTION CODE

13. ABSTRACT (*Maximum 200 words*)

A detailed investigation of the flow physics occurring on the suction side of a simulated Low Pressure Turbine (LPT) blade was performed. A contoured upper wall was designed to simulate the pressure distribution of an actual LPT blade onto a flat plate. The experiments were carried out at Reynolds numbers of 100,000 and 250,000 with three levels of freestream turbulence. Freestream turbulence levels ranging from 0.8% to 3% was used in this experiment. Smoke-wire flow visualization data was used to confirm that the boundary layer was separated and formed a bubble. Hot-wires (single and x-wire) and surface mounted hot-film gages and static pressure taps were used to map the flowfield. The transition process over the separated flow region is observed to be similar to a laminar free shear layer flow with the formation of a large coherent eddy structure. For each condition, the locations defining the separation bubble were determined by careful examination of pressure and mean velocity profile data. Transition onset location and length determined from intermittency profiles decrease as freestream turbulence levels increase. Additionally, the length and height of the laminar separation bubbles were observed to be inversely proportional to the levels of freestream turbulence.

14. SUBJECT TERMS
Low-pressure turbine; Boundary layer; Experiment

15. NUMBER OF PAGES
165

16. PRICE CODE
A08

17. SECURITY CLASSIFICATION OF REPORT	18. SECURITY CLASSIFICATION OF THIS PAGE	19. SECURITY CLASSIFICATION OF ABSTRACT	20. LIMITATION OF ABSTRACT
Unclassified	Unclassified	Unclassified	

Sharma, O. P., "Momentum and Thermal Boundary Layer Development on Turbine Airfoil Suction Surfaces", AIAA-87-1918, June 1987.

Simon, F. F. and Ashpis, D. E., "Progress in Modeling of Laminar to Turbulent Transition on Turbine Vanes and Blades", Submitted for Publication in the *International Journal of Heat Transfer and Fluid Flow*, May 1996.

Simon, T. W. and Qiu, S., "Measurements in a Transitional Boundary Layer Under Low-Pressure Turbine Airfoil Conditions", Proposed NASA Contract Report, October 1997.

Sohn, K. H. and Reshotko, E., "Experimental Study of Boundary Layer Transition With Elevated Freestream Turbulence on a Heated Flat Plate", NASA CR-187068, 1991.

Suder, K. L., O'Brien, J. E. and Reshotko, E., "Experimental Study of Bypass Transition in a Boundary Layer", NASA TM-100913, 1988.

Tani, I., "Low Speed Flows Involving Bubble Separations", Progress in Aeronautical Sciences, Vol. 5, pp. 70-104, 1964.

Tennekes, H. and Lumley, J. L., **A First Course in Turbulence**, MIT Press, Second edition, Massachusetts, 1972.

Walker, G. J., "The Role of Laminar-Turbulent Transition in Gas Turbine Engines: A Discussion", *Journal of Turbomachinery*, Vol. 115, April 1993, pp. 207-217.

White, F. M., **Viscous Fluid Flow**, McGraw-Hill, First edition, New York, NY, 1974.

Wisler, D. C., "Loss Reduction in Axial-Flow Compressors Through Low-Speed Model Testing", *Journal of Engineering for Gas Turbines and Power*, Vol. 7, April 1985, pp. 354-363.

Yavuzkurt, S., "A Guide to Uncertainty Analysis of Hot-Wire Data", *Journal of Fluids Engineering*, Vol. 106, June 1984, pp. 181-186.